

# **Cyclic Uniaxial Constitutive Model For Steel Reinforcement**

Se-Hyung Kim

Thesis submitted to the faculty of the Virginia Polytechnic Institute and State University in  
partial fulfillment of the requirements for the degree of

Master of Science  
In  
Civil and Environmental Engineering

Ioannis Koutromanos  
Roberto T. Leon  
Carin L. Roberts-Wollmann

December 11<sup>th</sup>, 2014  
Blacksburg, VA

Keywords: Reinforcing Steel, Constitutive Model, Cyclic Loading, Buckling, Rupture

# **Cyclic Uniaxial Constitutive Model For Steel Reinforcement**

Se-Hyung Kim

## **ABSTRACT**

Reinforced Concrete (RC) structures are common in earthquake-prone areas. During an earthquake, the steel reinforcement is subjected to cyclic strain histories which lead to inelastic response. In the case of rare, strong earthquakes, inelastic buckling and even rupture due to low-cycle fatigue can also occur. The understanding and characterization of the performance of RC structures under earthquake hazards requires the accurate simulation of the inelastic hysteretic behavior of steel reinforcement by means of appropriate constitutive models.

Several uniaxial material models have been developed for reinforcing steel. Existing material models sacrifice efficiency for accuracy or vice versa. Conceptually simple and numerically efficient models do not accurately capture the hysteretic response and ignore rupture or buckling. On the other hand, more refined material models are characterized by iterative stress update procedures which can significantly increase the computational cost of an analysis. Additionally, experience suggests that refined models attempting for the effect of inelastic buckling tend to lead to numerical convergence problems in the stress update procedure.

The goal of the present study is the formulation and implementation of an accurate and computationally efficient constitutive model for steel reinforcement under cyclic loading. A previously developed model, capable of capturing the inelastic hysteretic response of reinforcing steel in the absence of buckling and rupture, is used as a starting point in this study. The model is enhanced by replacing its original, iterative stress update procedure with an equally accurate, non-iterative one. Additionally, the model is enhanced to capture the effects of inelastic buckling and of rupture. The accuracy of the model and the efficiency of the non-iterative stress update

algorithm are demonstrated by means of validation analyses.

## **Acknowledgements**

The work presented in this thesis would not be possible without the help and support from several people. My greatest support came from my advisor, Dr. Ioannis Koutromanos, who provided great advice and always pushed me to work harder. I would like to thank Sadik Can Girgin for providing me with several key references during the preliminary stage of my thesis preparation. I would also like to thank my other committee members: Dr. Roberto Leon and Dr. Carin Roberts-Wollmann.

I would also like to thank several cohorts at the Virginia Tech Department of Civil and Environmental Engineering: Chia-Hung Fang, Jeremy Bowers, Michael Gangi, Mohammadreza Moharrami Gargari, and Junle Cai. Their input has been greatly appreciated.

Last, but not least, I would like to thank my family and Meagan Betke. They have encouraged me and provided much needed love and support during this experience.

## Table of Contents

<b>Notation</b> .....	viii
<b>List of Figures</b> .....	xiv
<b>List of Tables</b> .....	xviii
<b>1. Introduction</b> .....	1
<b>1.1 Background</b> .....	1
<b>1.2 Stress-Strain Behavior of Steel</b> .....	1
<b>1.3 Effects of Inelastic Buckling</b> .....	2
<b>1.4 Motivation for Research</b> .....	5
<b>1.5 Research Approach</b> .....	6
<b>2.Literature Review</b> .....	7
<b>2.1 Stress-Strain Law of Reinforcing Steel Bars</b> .....	7
<b>2.2 Accounting for Inelastic Buckling</b> .....	10
<b>2.3 Accounting for Low Cycle Fatigue</b> .....	13
<b>2.4 Significance of Research</b> .....	14
<b>3.Proposed Stress-Strain Material Model</b> .....	15
<b>3.1 Proposed Model Overview</b> .....	15
<b>3.2 Original Dodd and Restrepo Model</b> .....	18
<b>3.3 NURBS Approximation to the Nonlinear Reversal Curve</b> .....	24
3.3.1 <i>Introduction to the NURBS approximation</i> .....	24
3.3.2 <i>NURBS-Based Interpolation Equations</i> .....	26
3.3.3 <i>Effect of Carbon Content on the Nonlinear Reversal Curve</i> .....	28

<b>3.4 Simulating the Effects of Inelastic Buckling</b> .....	30
3.4.1 <i>Simulating the Effects of Inelastic Buckling</i> .....	30
3.4.2 <i>Calculating the Buckling Strength Degradation Factor</i> .....	40
3.4.3 <i>Application to Other Material Models</i> .....	42
<b>3.5 Accounting for Low-Cycle Fatigue</b> .....	43
<b>4.Verification of the Material Model</b> .....	47
<b>4.1 Verification of Hysteretic Stress Response Without Buckling</b> .....	47
<b>4.2 Verification of Buckling Strength Degradation Analysis</b> .....	49
<b>4.3 Verification of Low-Cycle Fatigue Law</b> .....	51
<b>4.4 Computational Time of Analyses</b> .....	52
<b>5.Summary and Discussion</b> .....	55
<b>6.Need for Further Research</b> .....	58
<b>References</b> .....	60
<b>Appendix A: Derivation of Basis Functions in NURBS-Based Interpolations</b> .....	64
<b>A.1 Introduction</b> .....	64
<b>A.2 B-Spline Basis Functions</b> .....	64
<b>Appendix B: Calibration and Calculation of Linear Portion of Major Reversals</b> .....	67
<b>B.1 Introduction</b> .....	67
<b>B.2 Calibration of <math>\mathbf{b}</math></b> .....	68
<b>B.3 Calculation of <math>\mathbf{b}</math></b> .....	74
<b>B.4 Verification</b> .....	75
<b>Appendix C: Proof of Sign Retainment of Radical in Equation for <math>\mathbf{u}</math></b> .....	79
<b>C.1 Introduction</b> .....	79

<b>C.2 Un-weighted NURBS Curves.....</b>	<b>79</b>
<b>C.3 In Calculations For The Onset of Buckling.....</b>	<b>80</b>
<b>Appendix D: Single Curvature Check in Reversal curves.....</b>	<b>82</b>
<b>D.1 Introduction.....</b>	<b>82</b>
<b>D.2 Sign Retainment in the Natural Coordinate Space.....</b>	<b>82</b>
<b>D.3 Major Reversals.....</b>	<b>83</b>
<b>D.4 Minor and Simple Reversals.....</b>	<b>84</b>
<b>D.5 Sign Retainment in the Engineering Coordinate Space.....</b>	<b>86</b>
<b>Appendix E: Comparison Between the Analytical Values and Approximated Values of the</b>	
<b>Sectional Tangent Stiffness Matrix for a Reinforcing bar.....</b>	<b>89</b>
<b>E.1 Introduction.....</b>	<b>89</b>
<b>E.2 Determining the Onset of Buckling.....</b>	<b>89</b>
<b>E.3 Deriving the Sectional Tangent Matrix.....</b>	<b>92</b>
<b>Appendix F: Calibration of Strength Degradation Factor with Monotonic Experimental</b>	
<b>Data.....</b>	<b>96</b>
<b>F.1 Introduction.....</b>	<b>96</b>
<b>F.2 Method.....</b>	<b>96</b>

## Notation

$NURBS$	Non-Uniform Rational B-Splines;
$RC$	Reinforced Concrete;
$a$	Half of the width of neutral axis on the reinforcement bar;
$A$	Area of a portion of the reinforcing bar cross section;
$b$	A parameter used to find the location of $\varepsilon''_k$ ;
$b$	Distance to the neutral axis (Figure E1);
$C$	Coordinate parameter used in the parametric NURBS expressions;
$D$	Diameter of the reinforcing bar;
$D_{crit}$	Critical value of damage variable for occurrence of rupture due to low-cycle fatigue;
$D_m$	A measure for how much damage occurred due to low-cycle fatigue;
$\hat{D}_T$	A general expression for the stiffness matrix;
$E_o$	The unloading modulus in engineering coordinates;
$E_s$	Young's modulus of elasticity;
$E_{sh}$	The initial tangent of the strain hardening curve;
$E_T$	Slope of the stress strain curve in engineering coordinates;
$\bar{E}_T$	Slope of the stress strain curve in engineering coordinates;
$E'_u$	Unloading modulus;
$f''$	Stress in the normalized natural coordinate space;



$f_1$	The normalized true stress coordinate of the second control point in the NURBS approximation of logarithm (base 10) of the strength degradation factor;
$f''_1$	The normalized true stress coordinate of the first control point in the NURBS approximation of the normalized true stress;
$f_2$	The logarithm (base 10) of the strength degradation factor at the negative of the ultimate strain;
$f'_a$	True stress at the beginning of the nonlinear reversal curve;
$f_b$	The strength degradation factor;
$f''_j$	The normalized true stress coordinate of the second control point in the NURBS approximation of normalized true stress;
$f''_k$	The normalized true stress coordinate of the first control point used in the NURBS approximation for major reversal curves;
$f'_p$	The stress magnitude between inclined envelope and point at initiation of Bauschinger effect;
$f'_{rejoin}$	True stress at the rejoin point;
$f'_r$	True stress at a strain reversal;
$f_s$	Engineering stress;
$f'_s$	True stress;
$f'_{sh}$	True stress at the onset of strain hardening;
$f'_{sh,1}$	Arbitrary true stress coordinate on strain hardening curve;

$f'_t$	The stress magnitude between top and bottom inclined envelopes in the natural coordinate system;
$f_{su}$	Engineering stress at ultimate;
$f'_{su}$	True stress at ultimate;
$f'_{su}^*$	Slope of true stress-strain curve at the rejoin coordinates;
$f_y$	Yield stress;
$h$	Maximum change in stress (Figure E1);
$I$	Moment of Inertia of a portion of the reinforcing bar cross section about the neutral axis;
$k$	Directional factor equal to 1 for tensile curves and 2 for compressive curves;
$L$	The spacing between the confinement ties;
$m$	Directional factor equal to 2 for tensile curves and 1 for compressive curves;
$M$	Internal moment in the reinforcing bar;
$M1$	The initial asymptote in the NURBS approximation of the logarithm (base 10) of the strength degradation factor;
$M2$	The final asymptote in the NURBS approximation of the logarithm (base 10) of the strength degradation factor;
$m_d$	Slope of the final line in the $b$ vs $\Omega$ curve (Appendix B);
$N$	Internal axial force in the reinforcing bar;

$N_{i,p}$	A Bernstein Polynomial of index $i$ and polynomial degree, $p$ , used in the NURBS approximations;
$P$	Power of the strain hardening curve;
$P_{0,1,2}$	Control points used in parametric NURBS expressions;
$R$	Radius of reinforcement bar;
$s$	Sign parameter equal to 1 for tensile curves and -1 for compressive curves;
$t$	A material constant that determines how much damage the material experiences for a change in tensile stress;
$u$	Independent variable used in the Parametric NURBS expressions;
$u_i$	An element of the knot vector used in the NURBS approximations;
$u_T$	Independent variable used in the Parametric NURBS expressions for the section modulus stiffness matrix;
$V$	Volume of change of stress distribution along the reinforcement bar;
$w_{0,1,2}$	Weights on the control points used in parametric NURBS expressions;
$x$	Distance along the reinforcing bar;
$\bar{y}$	Distance between the neutral axis and the extreme compression face of the reinforcing bar.;
$\gamma_T$	An expression for the stiffness matrix elements after it is generalized for all materials and reinforcing bar diameters;
$\Delta\varepsilon'_p$	Discrete incremental plastic strain increment;
$\varepsilon''$	Strain in the normalized natural coordinate space;

$\varepsilon''_1$	The normalized true strain coordinate of the first control point in the NURBS approximation of the normalized true stress;
$\varepsilon'_a$	True strain at the beginning of the nonlinear reversal curve;
$\varepsilon_b$	The strain at the onset of buckling;
$\varepsilon''_j$	The normalized true strain coordinate of the second control point in the NURBS approximation of normalized true stress;
$\varepsilon''_k$	The normalized true strain coordinate of the first control point used in the NURBS approximation for major reversal curves;
$\varepsilon'_M$	Maximum plastic strain;
$\varepsilon_n$	The strain normalized to the difference between the strain at the onset of buckling and the negative of the ultimate strain;
$\varepsilon_{n1}$	The normalized true strain coordinate of the second control point in the NURBS approximation of logarithm (base 10) of the strength degradation factor;
$\varepsilon'_o(k)$	Shifted origin true strain;
$\varepsilon'_p$	The strain magnitude between inclined envelope and point at initiation of Bauschinger effect in natural coordinate system;
$\varepsilon'_r$	True strain at a strain reversal;
$\varepsilon'_{rejoin}$	True strain at the rejoin point;
$\varepsilon_s$	Engineering strain;

$\varepsilon_{sc}$	Engineering strain where the proposed model was calibrated with the original Dodd and Restrepo model (1995)
$\varepsilon'_s$	True strain;
$\varepsilon'_{sh}$	True strain at the onset of strain hardening;
$\varepsilon'_{sh,l}$	Arbitrary true strain coordinate on strain hardening curve;
$\varepsilon'_{su}$	True strain at ultimate;
$\varepsilon'_{su,shift}$	Shifted true ultimate strain;
$\varepsilon'_y$	True yield strain;
$\eta$	The ratio of the tangent to the stress-strain curve to the $E_o$ ;
$\theta$	The angle in radians of the circular arc on the perimeter of the unloading portion of the reinforcing bar cross section;
$\phi$	Curvature in the reinforcing bar;
$\phi_o$	Curvature in the reinforcing bar midway between confinement ties;
$\varphi$	Angle at which the neutral axis is located (Figure E1);
$\omega$	The lateral deflection of the reinforcing bar;
$\omega_o$	The maximum lateral deflection at midway between the confinement Ties;
$\Omega$	A parameter developed by Dodd and Restrepo (1995) to uniquely identify each reversal curve for any given material;
$\Omega_i$	Omega coordinates of key points along the $b$ vs. $\Omega$ curve (Appendix B);

## List of Figures

<b>Figure 1.1.</b>	Basic shape of a non-linear hysteretic loop including a linear elastic region, a yield plateau, a strain hardening region, compressive and tensile reversal curves.....	2
<b>Figure 1.2.</b>	Concrete Spalling on a Column with Exposing Reinforcing bar.....	3
<b>Figure 1.3.</b>	Illustration of the effects of inelastic buckling on a hysteretic curve starting from the onset of buckling, continuing to the compressive reversal curve, and ending the tensile reversal curve both of which experience strength degradation.....	4
<b>Figure 1.4.</b>	Experimental Results from a Buckled Bar Specimen (Monti and Nuti, 1992).....	4
<b>Figure 2.1.</b>	Illustration of the Overshooting Problem in Cycles of Low Amplitude.....	7
<b>Figure 2.2.</b>	Converting a Reversal Curve for a Normalized Coordinate Space.....	10
<b>Figure 2.3.</b>	Compression Buckled Curve with the Negative-Sloped Target Tangent.....	11
<b>Figure 2.4.</b>	Assumed Stress Distributions in the Cross-Section of a Buckled Reinforcing Bar for Various Models in the Literature.....	12
<b>Figure 3.1.</b>	Components of a Reversal Curve in the Dodd and Restrepo Material Model Starting with a Linear Unloading Curve and Continuing into the Nonlinear Curve.....	17
<b>Figure 3.2.</b>	Comparison Between the Tensile and Compressive Stress-Strain Monotonic Behavior in Natural Coordinates and Engineering Coordinates.....	19
<b>Figure 3.3.</b>	Illustration of Reversals from the Yield Plateau, Minor Reversals and Major Reversals As Well As Their Respective Rejoin Points.....	21

<b>Figure 3.4.</b>	Illustration of the Shift in the Rejoin Coordinate After the Strain Unloads to a Non-Zero Value.....	23
<b>Figure 3.5.</b>	Examples of the Implementation of the NURBS Approximation.....	25
<b>Figure 3.6.</b>	Illustration of Minor and Major Reversals in the Normalized Coordinate Space.....	28
<b>Figure 3.7.</b>	Cyclic Test Results Plotted in Terms of Absolute Stress and Strain.....	29
<b>Figure 3.8.</b>	Buckled shape of the isolated reinforcing bar between two confinement ties.....	31
<b>Figure 3.9.</b>	Example of the reduced modulus theory implemented in the proposed model starting with the reinforcing bar with a uniform stress distribution, then applying a change in stress distribution, and resulting in the non-linear stress distribution shown in the bottom.....	32
<b>Figure 3.10.</b>	Free Body Diagram of Half of the Buckled Shape of the Reinforcing bar. The signs are positive for Tensile Forces and Counter-Clockwise Rotations While the Orientations Drawn Reflect the Predicted Response.....	35
<b>Figure 3.11.</b>	Relationships Between $t$ and $D_{crit}$ that Lead to an Accurate Cycle of Rupture for Test Specimens tested by Kunnath et al. (2009b) with the cross hairs denoting the coordinate used on analysis.....	46
<b>Figure 4.1.</b>	Comparison between the Analyses from the Proposed and Original Dodd and Restrepo Model (2005).....	47
<b>Figure 4.2.</b>	Verification of Proposed Stress-Strain Law Calculations with Experimental Results.....	48
<b>Figure 4.3.</b>	Simulated Stress Response Without Buckling According to the Modified Proposed Model and the Model by Dhakal and Maekawa (2002a).....	50

<b>Figure 4.4.</b>	Analytical and Experimental Cyclic Responses of Test Specimens Examined By Monti and Nuti (1992).....	51
<b>Figure 4.5.</b>	Verification of Low Cycle Fatigue Analysis Between Proposed Model and Experimental Results Gathered by Kunnath (2009b).....	52
<b>Figure 4.6.</b>	Computational Time Analysis of the Original and Modified Material Models....	53
<b>Figure B1.</b>	Initial $b$ Optimization Analysis.....	69
<b>Figure B2.</b>	First linear portions of $b$ vs. $\Omega$ .....	69
<b>Figure B3.</b>	General Form of the Variation of $b$ with $\Omega$ .....	70
<b>Figure B4.</b>	Effects of Varying Material Properties on the $b$ vs. $\Omega$ Relationship.....	71
<b>Figure B5.</b>	Determination of $b$ vs. $\Omega$ relationship constants.....	73
<b>Figure B6.</b>	Comparison Between $b$ vs. $\Omega$ Approximated and Analytical Relationships.....	75
<b>Figure C1.</b>	Variation of $u$ with $\eta$ in the Equations for Buckling Considerations.....	81
<b>Figure D1.</b>	Stress-Strain Tangent vs. Strain Along a Compressive Reversal.....	87
<b>Figure D2.</b>	Stress-Strain Tangent vs. Strain Along a Tensile Reversal.....	87
<b>Figure E1.</b>	Geometry of a Cylindrical Wedge (Weisstein, n.a.).....	90
<b>Figure E2.</b>	Comparison of Analysis from (E.4) and NURBS Approximation of the Ratio of the Location of the Neutral Axis to the Diameter of the Reinforcing bar.....	92
<b>Figure E3.</b>	Comparison between Analytical Results and NURBS Approximations in Predicting the Stiffness Matrix Parameters.....	94
<b>Figure F1.</b>	Variation of the Strength Degradation Factor with Strain Normalized to the Buckled Strain and Slenderness Ratio.....	97
<b>Figure F2.</b>	Variation of Logarithm of the Strength Degradation Factor with Normalized Strain.....	98



<b>Figure F3.</b>	Strength Degradation Factor at Negative Ultimate vs. Slenderness Ratio.....	98
<b>Figure F4.</b>	Relationship Between The Initial Slope, $M_1$ , and The Slenderness Ratio and Material Properties.....	99
<b>Figure F5.</b>	Comparisons Between The Proposed Approximation and The Experimental Results of the Logarithm of the Strength Degradation Factor (Bae et al., 2005).....	100
<b>Figure F6.</b>	Comparisons Between the Bare-Bar Monotonic Test Results and Approximations of the Buckled Response (Dhakal and Maekawa, 2002ab).....	101

## List of Tables

<b>Table 4.1.</b> Material Properties for Experiments and Analyses.....	48
<b>Table 4.2.</b> Material Properties of Specimens for Cyclic Tests.....	50
<b>Table 4.3.</b> Material Properties Used in Experiments and Analysis.....	52
<b>Table B1.</b> Material Properties of Initial <i>b</i> Optimization Analysis.....	68

# **1. Introduction**

## **1.1 Background**

Reinforced concrete (RC) structures constitute a significant portion of the building inventory in the United States, including seismically active regions like the western states. During earthquake loadings, cyclic inelastic strains may develop in structural components. The reliable determination of the performance of RC structures requires an accurate description of the cyclic inelastic behavior of steel reinforcement. There are different approaches to predicting the hysteretic behavior, including, but not limited to, representing any RC element as a truss or as a beam. These models can involve tens of thousands of elements and often use iterative algorithms such as the Newton-Raphson method to achieve force equilibrium in any given system.

A typical model of any kind will use a uniaxial material model to predict the hysteretic behavior of the steel reinforcing bars. This material model must not only be accurate for the validity of the analysis, but also computationally efficient and mathematically robust to reduce computational costs. To achieve an accurate and efficient model, several experiments have been carried out to gain the understanding of steel reinforcement that we have now.

## **1.2 Stress-Strain Behavior of Steel**

The typical cyclic behavior of steel reinforcing bars is illustrated in Fig. 1.1. The behavior is linearly elastic until the magnitude of stress reaches the yield stress. Beyond this point, the magnitude of the stress remains constant in the yield plateau. Strain hardening is a phenomena where the stress develops further than yield at higher strains. The stress increases

beyond this point only until the ultimate stress. This is the basic behavior of steel during a monotonic loading, which is what is experienced during the initial loading of the material.

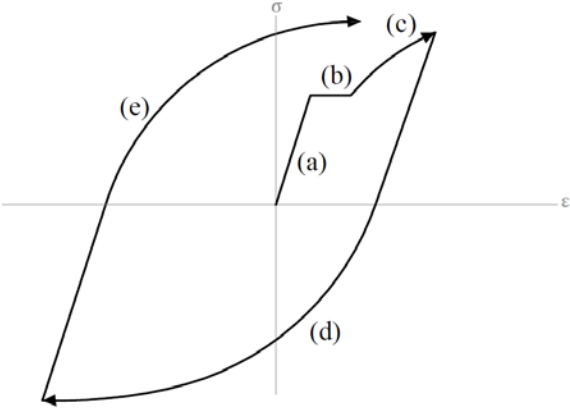


**Figure 1.1.** Basic shape of a non-linear hysteretic loop including a (a) linear elastic region, (b) a yield plateau, (c) a strain hardening region, (d) compressive and (e) tensile reversal curves.

In any seismic event, the ground motion will result in strains in the reinforcement that will reverse several times. After one of these reversals, the reinforcing steel yields at a lower magnitude of stress due to what is known as the Bauschinger effect. After the steel yields after a reversal, the stress-strain behavior develops curvature and forms a nonlinear curve shape. This curve shape, known as a reversal curve, continues until the next load reversal, after which the same behavior is observed except the change in stresses and strains will change sign. A sequence of reversal curves forms the non-linear hysteretic loop-shapes that represent the stress-strain law under cyclic loading.

### 1.3 Effects of Inelastic Buckling

At high tensile strains, large cracks form on the tension face of a concrete section. After enough of these cracks form, the cover concrete on the tension face will break off and leave the reinforcing bars exposed. With no cover concrete to resist lateral deflections, the reinforcing bar

is prone to buckle at high compressive forces as shown in Figure 1.3. Because this is common in RC columns and beams under cyclic loading, the effects of inelastic buckling have been heavily researched. The general shape of the cyclic stress-strain behavior of a buckled bar is shown in Figure 1.3. An example of experimental results of cyclic stress-strain behavior of a buckled bar is shown in Figure 1.4.

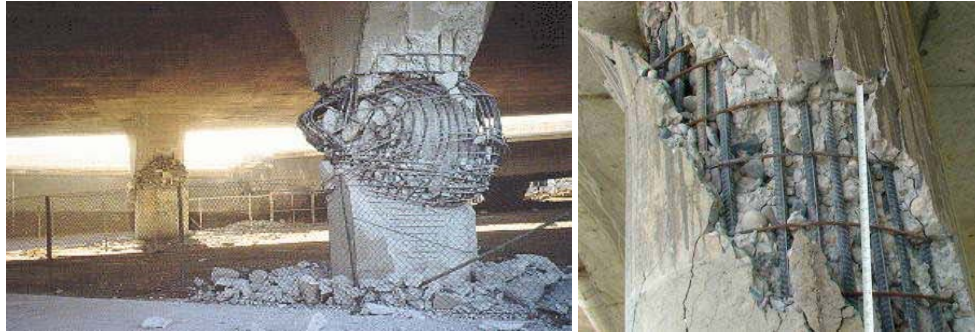


**Figure 1.2.** Concrete Spalling on a Column with Exposing Reinforcing bar.

Left Picture: Cooper, G.A. and Mander, J.B. (1994). “Seismic Energy Based Fatigue Damage Analysis of Bridge Columns: Part I – Evaluation of Seismic Capacity.” *Rep. NCEER-94-0006*, National Center for Earthquake Engineering Research, State University of New York at Buffalo, Buffalo, NY. Used under fair use, 2014.

Right Picture: N.A. (2012). “China Earthquake Reconnaissance Report: Performance of Transportation Structures During the May 12, 2008, M7.9 Wenchuan Earthquake.” From U.S. Department of Transportation: Federal Highway Administration – Office of Research, Development, and Technology, Office of Infrastructure.

<http://www.fhwa.dot.gov/publications/research/infrastructure/structures/11029/003.cfm>

Used under fair use, 2014.

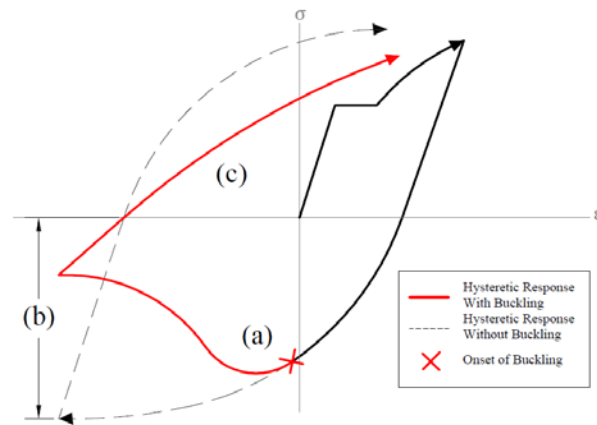


**Figure 1.3.** Illustration of the effects of inelastic buckling on a hysteretic curve starting from the (a) onset of buckling, (b) continuing to the compressive reversal curve, (c) and the tensile reversal curve both of which experience strength degradation.

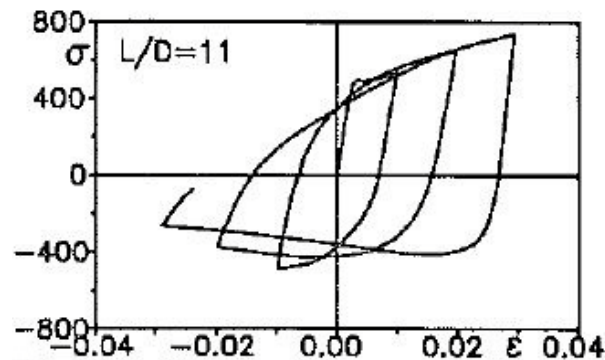


**Figure 1.4.** Experimental Results from a Buckled Bar Specimen.

Monti, G., and Nuti, C. (1992). "Nonlinear Cyclic Behavior of Reinforcing Bars Including Buckling." *Journal of Structural Engineering* 118(12), 3268-3284. Used under fair use, 2014.

After the onset of buckling, the reinforcing steel incurs softening, i.e. the compressive stress reduces for increasing compressive strain. The reduction occurs until the steel reaches the residual stress of the material, after which the stress in the material stays constant at the residual value. After a strain reversal, the strength in the tensile regions of the hysteretic loop are also affected. The rate reduction is still the same in these regions, meaning that the reduction decreases with a more tensile strain.

## 1.4 Motivation for Research

Many uniaxial material models have been developed to simulate the hysteretic behavior of reinforcing steel. The models proposed by Filippou et al. (1983) and Chang and Mander (1994) have had difficulty simulating the non-linear hysteretic loop shape and the strength degradation due to buckling. The material models which include simple and quick computations to simulate the hysteretic curve are less accurate in simulating the loop shape. The material models proposed by Dodd and Restrepo (1995) and Kunnath (2009a) are more accurate and require more complex, iterative calculations which significantly increase the computational cost of an analysis.

Several models have also been developed to account for the effect of buckling. The buckling effect is introduced by modifying the hysteretic equations, and this has negatively affected the numerical robustness of the models (Monti and Nuti, 1992)(Gomes and Appleton, 1997)(Dhakal and Maekawa 2002ab)(Urmson and Mander, 2012), rendering them prone to failure to obtain meaningful results. This has been observed for, as an example, the currently available material model in OpenSees. Furthermore, the few models that account for low-cycle fatigue and rupture require a significant amount of memory which also increases the computational costs of an analysis (Kunnath et al., 2009ab). As stated before, a typical analysis will already involve an iterative process and many elements. This means that any increase in computation time and probability for convergence failures will multiply with each iteration and element. Since accuracy is also crucial to the success of the RC model as a whole, there needs to be a material model for steel that is accurate, computationally efficient, and robust without compromising one of these properties for another.

## **1.5 Research Approach**

This thesis proposes a uniaxial material model that is computationally efficient, accurate, and robust. Most of the material models only use iterative processes when calculating the nonlinear hysteretic loop shapes, while the remainder of any given model involves direct calculations. Therefore, the proposed model is a modification on an existing model rather than a completely new model, retaining the direct calculations while eliminating the iterative processes. The Dodd and Restrepo model (1995) was chosen to be modified due to its high level of accuracy. While the calculations for the nonlinear reversal portion of a hysteretic curve require iterations, a majority of the model doesn't. Therefore, most of the Dodd and Restrepo model was retained (Dodd and Restrepo, 1995).

The model proposed in this thesis implements a Non-Uniform Rational B-Spline (NURBS) interpolation to allow the accurate description of the hysteretic curves, while removing the need for an iterative stress update algorithm. The effects of inelastic buckling are introduced through a strength degradation factor which is applied to an already calculated axial stress along the hysteretic loop. This factor will only be applied if the reinforcement strains become more compressive than that at the onset of buckling. This separates the considerations for buckling from the stress-strain law, eliminating any possibility for numerical convergence failure. Finally, the rupture of the reinforcing bar due to low-cycle fatigue is predicted using a continuous damage model. This will be implemented without interfering with the prediction of the hysteretic loop and the considerations for buckling will retain the robustness of the model.



## 2. Literature Review

### 2.1 Stress-Strain Law of Reinforcing Steel Bars

Many of the current material models for the cyclic response of steel reinforcement use variations of the equation proposed by Menegotto and Pinto (Filippou et al. 1983). This equation is computationally efficient and includes hysteretic loop shape. However, these models tend to under/over-predict the stress when in cycles of low amplitudes, where the stresses at the two reversal points do not differ significantly. Experimental tests have shown that if the amplitude of the cycle is low enough, the reversal will rejoin the reversal curve of a previous, high-amplitude cycle. This means that the curvature of the non-linear hysteretic loop is not always accurately simulated in these models. Figure 2.1 shows a low amplitude cycle over/under-predicting the stress.

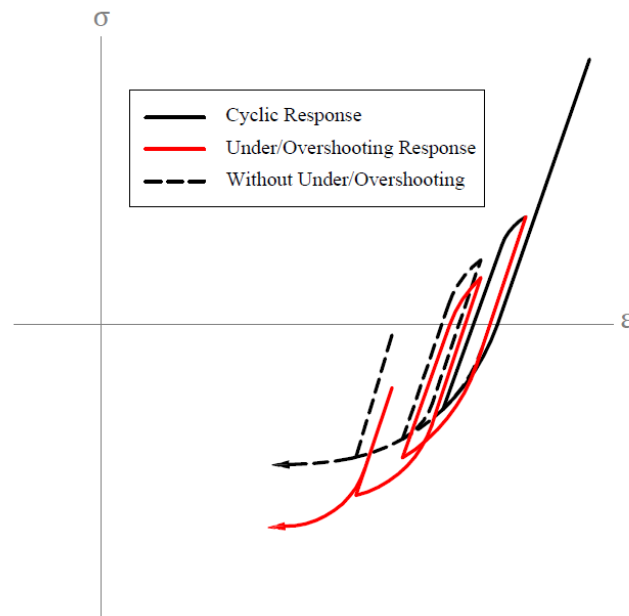


**Figure 2.1.** Illustration of the Overshooting Problem in Cycles of Low Amplitude.

This is a problem found in the Menegotto-Pinto equation as well as the modified Menegotto-Pinto equation by Filippou et al. (1983). Chang and Mander (1994) partly remedied the issue by creating conditions for a curve in a low-amplitude cycle to return to a previous, high-amplitude reversal curve to reflect the behavior shown in the aforementioned experiments. However, Kunnath et al. (2009a) noticed that their efforts were not sufficient enough to correct the issues.

Kunnath et al. (2009a) propose that Chang and Mander did not include a sufficient number of conditions to dictate the behavior of a reversal curve after a low-amplitude cycle. Kunnath et al. (2009a) propose a model that creates more conditions for these reversals depending on where the strain reversal happened. This further reduces the over-shooting and under-shooting which occurs in cycles of low amplitude. However, more conditions means more memory required in an analysis which compromises computational time. Furthermore, the Menegotto-Pinto equation as modified by Chang and Mander requires iterations to correct the curvature of the reversal curves. Kunnath et al. (2009a) modified the material model proposed by Chang and Mander; so it must also use the same iterative processes.

Dodd and Restrepo (1995) calibrated a new material model to experimental data that they gathered previously with other researchers (Restrepo et al., 1994). This model relies on two coordinate transformations in order to accurately predict the axial strain at any strain step. After the first coordinate transformation, the transformed tensile and compressive curves are virtually identical, simplifying calculations. The second coordinate transformation normalizes the curve to the specific material properties of the reinforcing steel. Furthermore, different algorithms are used for reversal curves in high amplitude cycles and those in low amplitude cycles, which Dodd and Restrepo call major and minor reversals respectively. These algorithms effectively remedy

the previously mentioned over/under-shooting problem. Dodd and Restrepo (1995) define minor reversals as those where the stresses at the reversal points have a difference less than or equal to twice the yield stress. The curvature of the stress-strain curve and the ranges of stress and strain vary on these conditions. The calculated stress is close to their experimental data. However, the calculation for the stress requires iterative processes when simulating the nonlinear curve shape, making the model inefficient. Furthermore, these iterative processes are not guaranteed to converge, which makes these calculations unacceptable (Dodd and Restrepo, 1995).

Furthermore, a coordinate transformation utilized in the model is very complex, making calculating the slope of the stress-strain curve through the chain rule of differentiation difficult as shown in Figure 2.2. There is no way to calculate the slope analytically using this coordinate transformation, and Dodd and Restrepo calculate an upper bound to the slope instead. This is insufficient because their model relies on the slope to calculate the stress response in their minor reversal curves. Also, the slope of the reversal curve is important for the proposed method when simulating the effects of buckling in the material, a phenomenon that Dodd and Restrepo don't account for in their proposed material model (Dodd and Restrepo, 1995). This will be elaborated on in a later section, but it should be noted now that an analytical calculation for slope is crucial to the considerations for inelastic buckling.

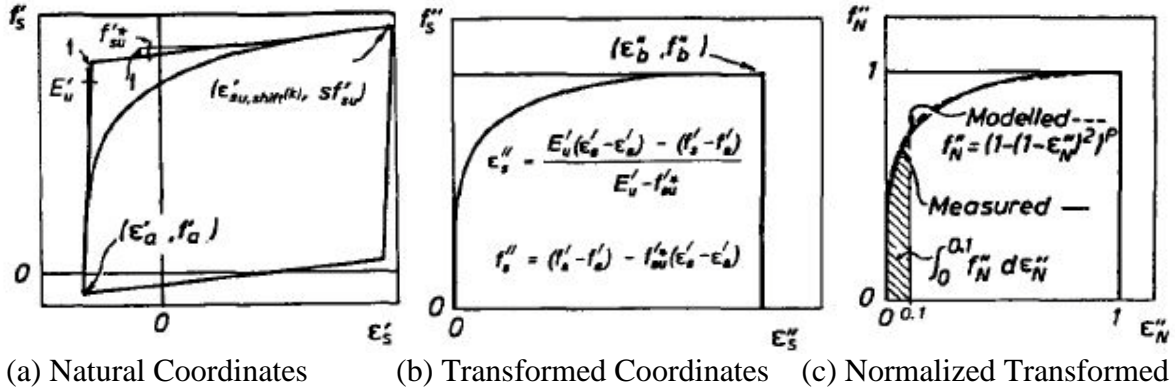


**Figure 2.2.** Converting a Reversal Curve for a Normalized Coordinate Space.  
 Dodd, L.L., and Restrepo-Posada, J.I. (1995). "Model For Predicting Cyclic Behavior of Reinforcing Steel." *Journal of Structural Engineering* 121(3), 433-445.  
 Used under fair use, 2014.

## 2.2 Accounting for Inelastic Buckling

The material models that use a variation of the Menegotto-Pinto equations for their stress-strain law adjust the Menegotto-Pinto equations when simulating the compressive reversal curve to account for the strength degradation due to inelastic buckling (Monti and Nuti, 1992)(Dhakal and Maekawa, 2002a,b). These models achieve this by adjusting the target point of the curve as well as the slope of the tangent at the end of the curve to ensure a negative sloping compressive reversal curve, simulating the strength degradation due to inelastic buckling. Monti and Nuti (1992) proposed one of those models as shown in Figure 2.3. While they improve in accuracy on Filippou, Popov, and Bertero's (1983) approach to inelastic buckling, Monti and Nuti created a very complex model and only calibrated it to a specific set of specimens with the similar material properties and only three slenderness ratios. As a result of this, Monti and Nuti underestimated the effect that material properties, such as the yield stress, have on the adjusted compressive reversal curve. Their material model is very limited for these reasons. (Monti and Nuti, 1992).

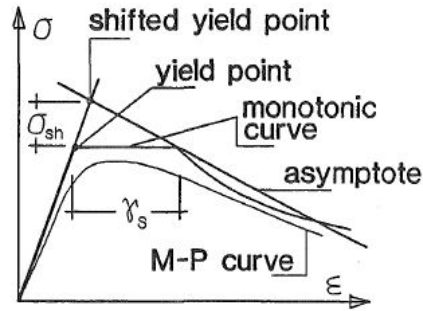


**Figure 2.3.** Compression Buckled Curve with the Negative-Sloped Target Tangent.  
 Monti, G., and Nuti, C. (1992). “Nonlinear Cyclic Behavior of Reinforcing Bars Including Buckling.” *Journal of Structural Engineering* 118(12), 3268-3284. Used under fair use, 2014.

Gomes and Appleton account for inelastic buckling by treating the bar as a beam that has reached its plastic moment. The bar is assumed to have plastic hinges formed at the confinement ties and halfway between the ties. This assumption isn't valid for all slenderness ratios, or ratio of length to diameter of the bar, as the bar could buckle before it reaches full plastic moment. This model also utilizes an iterative process to find the buckled stress response, which compromises efficiency (Gomes and Appleton, 1997). Urmson and Mander also account for buckling by treating the bar as a beam except they did not assume that the bar has reached plastic moment. They observe the non-linear stress distribution along the cross-section of the beam and obtain the axial load through integration. By doing this, they have achieved physically meaningful analytical results, in contrast to other research which relied too much on empiricism. They have derived a relatively simple equation for calculating the buckled stress in the reinforcing bar by calibrating it to the analytical results. (Urmson and Mander, 2012). Figure 2.4 compares the stress distribution used in both of these methods.

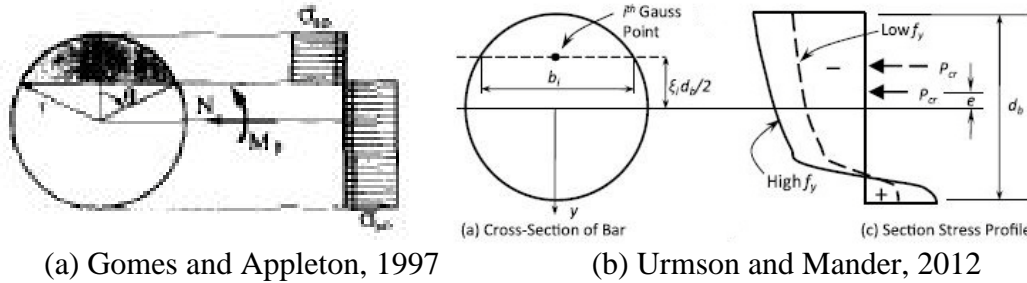


**Figure 2.4.** Assumed Stress Distributions in the Cross-Section of a Buckled Reinforcing bar For Various Models in the Literature.

Gomes, A. and Appleton, J. (1997). “Nonlinear Cyclic Stress-Strain Relationship of Reinforcement Bars Including Buckling.” *Engineering Structures* 19(10), 822-826.

Used under fair use, 2014.

Urmson, C.R., and Mander, J.B. (2012). “Local Buckling Analysis of Longitudinal Reinforcing Bars.” *Journal of Structural Engineering* 138(1), 62-71.

Used under fair use, 2014.

Dhakal and Maekawa (2002a,b) also adjust the Menegotto-Pinto equation to account for the slenderness ratio, which is similar to the approach by Monti and Nuti (1992). Unlike Monti and Nuti (1992), they calibrated their model to specimens of varying yield stresses, making the model more applicable to reinforcing steel of different material properties. Dhakal and Maekawa (2002a,b) varied key components of the compressive reversal curve by the slenderness ratio multiplied by the square root of the yield stress. Any calculations for simulating the hysteretic behavior would ideally be unitless, and this approach to inelastic buckling is not.

Finally, all of the aforementioned material models account for buckling by adjusting the stress-strain law (Dhakal and Maekawa, 2002a,b)(Gomes and Appleton, 1997)(Urmson and Mander, 2012)(Monti and Nuti, 1992). As stated previously in the introduction, adjusting the stress-strain law parameters introduces the probability for numerical convergence failure. A material model must be robust enough that in a complicated analysis involving many elements

and considerations for force equilibrium, the material model for steel always converges and provides an accurate value for the stress response.

### **2.3 Accounting for Low Cycle Fatigue**

Kunnath et al. (2009a,b) account for the damage due to low-cycle fatigue by counting the number of strain cycles that the reinforcement experiences. The number of cycles in any single analysis will be calculated based on the amount and magnitude of the local maximum and minimum strains in any given strain history. These considerations provide a prediction for strength degradation and rupture due to low-cycle fatigue (Kunnath et al., 2009a,b). Their method yielded results that agreed with their experimental data; however, current cycle-counting algorithms require at least a portion of the strain history to be stored into memory. The more required memory in an analysis means a bigger increase in required computational time. This makes this complex method more time consuming (ASTM, 2011).

Huang and Mahin (2010) suggested incorporating a continuous damage model, which requires less memory and has been shown to provide similar results to the Coffin-Manson relation that Kunnath et al. (2009a,b) use. This model also proposes that the damage caused to low-cycle fatigue is a result of the tensile stress rather than the number of cycles, which is a better approach conceptually as mentioned before. This model calculates the accumulated damage at every step in the strain history. Although the model has been developed for multi-axial steel models, the model has been modified to be applied to the proposed uniaxial model in this study (Huang and Mahin, 2010).

## **2.4 Significance of Research**

There has yet to be a material model that is accurate, computationally efficient, and robust. Previous research has focused on only one or two of these characteristics without giving much thought to the others. Accuracy can only be achieved when the material model considers all aspects of inelastic behavior including buckling and rupture. Efficiency can only be achieved when the stress update algorithm does not require iterations are direct and don't involve iterations. Robustness can only be achieved when inelastic buckling and low-cycle fatigue is accounted for without changing the hysteretic equations. The material model proposed in this thesis achieves all three, which leads to an accurate prediction of the inelastic response in the RC structure without high computational costs and the possibility for numerical convergence failure.



### **3. Proposed Stress-Strain Material Model**

#### **3.1 Proposed Model Overview**

As stated in the literature review, there has yet to be a material model that can guarantee accuracy, computational efficiency and robustness. All three are needed especially if large models of structures undergoing significant inelastic deformations are pursued. The model combines all three by implementing the following steps:

1. Calculate the stress with the proposed stress-strain law.
  - a. When in the monotonic portions and linear portions of the cyclic behavior, use the original Dodd and Restrepo (1995) equations.
  - b. When in the nonlinear cyclic portions of the hysteretic behavior, use the proposed Non-Uniform Rational B-Spline (NURBS) based interpolations.
2. Determine if the behavior of the reinforcing steel has met the proposed assumed buckling criterion.
  - a. If not, the stress remains as previously calculated.
  - b. If it has, calculate the strength degradation factor and apply it to the stress.
3. Check if the reinforcing bar has ruptured due to low-cycle fatigue using the updated stress response.
  - a. If not, then the stresses will continue to be updated in the next strain step.
  - b. If it has, the material under consideration is considered ruptured and can no longer develop any stress.

This chapter details the equations, calibrations, and derivations behind each of these steps.

The first step is possible through modifying a highly accurate material model. To find a suitable material model to calibrate the proposed model's stress-strain law to involved finding out how these models were derived. Many material models were calibrated to data gathered from experiments which applied an axial strain and recorded the stress that resulted from it. The specimens used in these experiments often varied in their chemical properties even though the reinforcement used in earthquake-prone areas in the United States do not. The most popular material for steel reinforcement is the ASTM A706 reinforcing bar because the ASTM put specifications for chemical properties in steel reinforcing bar to ensure highly ductile properties. The specimens tested by Dodd and Restrepo are similar in carbon content to this reinforcing bar, making a more relevant material model for RC structures in earthquake-prone areas (Dodd and Restrepo, 1995).

As stated before, the Dodd and Restrepo model involves iterative processes which compromise computational efficiency. However, these iterative processes are only used when calculating what they refer to as the softening curve, which is the portion of the reversal curve after the material has yielded and unloaded from stress as shown in Figure 3.1. They incorrectly use the term "softening" to describe this portion of the reversal curve because it refers to any behavior in the material after the bar has yielded. For the purposes of this research, this portion is referred to as the nonlinear reversal curve. Therefore, most of the original Dodd and Restrepo material model was retained while the calculations for the nonlinear reversal curve were replaced with a Non-Uniform Rational B-Spline (NURBS) based interpolation. The computationally efficient method will be calibrated to the original Dodd and Restrepo (1995) calculations as to retain the model's accuracy (Dodd and Restrepo, 1995).

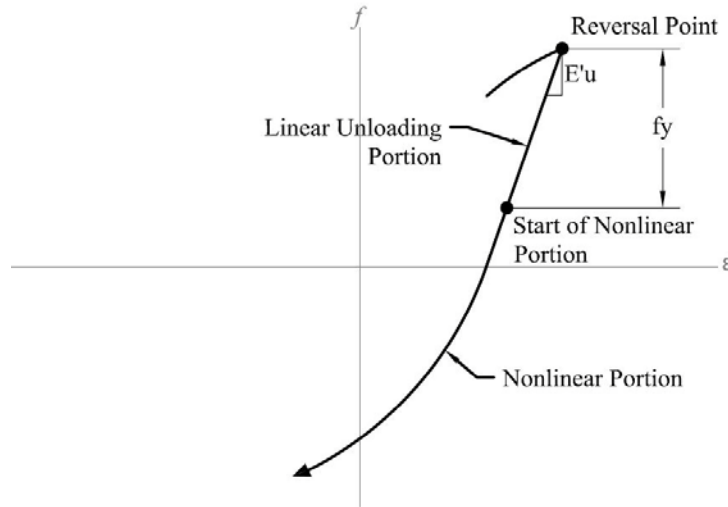


**Figure 3.1.** Components of a Reversal Curve in the Dodd and Restrepo Material Model Starting with a Linear Unloading Curve and Continuing into the Nonlinear Curve.

The second step is possible through the proposed definition of the onset of buckling, which is the point at which a change in axial strain causes no change in axial stress. This is similar to the buckling conditions in the approach by Urmson and Mander (2012) in that the reinforcing bar is treated as a beam with a non-linear distribution of stresses along the cross-section. The proposed model simplifies the calculation by assuming the distribution of the change in stress due to an instantaneous change in axial strain along the cross section is linear. Using this, the net change in stress can be calculated at any given strain.

After the onset of buckling is determined, the strength degradation factor is determined. A logarithmic relationship between the strain and the factor is derived in a later section and implemented. This factor will then reduce the stresses (tensile and compressive) calculated by the modified Dodd and Restrepo model for strains more compressive than the strain at the onset of buckling.

The last step involves the prediction of rupture due to low-cycle fatigue, which is based on a simple formulation by Huang and Mahin (2010). The prediction involves a variable that

represents the cumulative damage in the steel due to tensile stresses. This variable is updated at every step the reinforcing bar is in tension and the predicted rupture will be at the point when this variable exceeds a critical damage constant which depends on material properties. This material constant will be calibrated to rupture tests performed by Kunnath et al. (2009b).

Once the values of these parameters have been calibrated to experimental tests, they were compared with cyclic tests. The proposed method to calculate the nonlinear reversal curve is compared with the original experimental tests done by Dodd and Restrepo (1995) to show that the curve has been well calibrated to the original code. The predicted strength degradation due to buckling is compared with the experimental cyclic results collected by Monti and Nuti (1992). The predicted strain at rupture is compared with the results of the experimental tests performed by Kunnath et al. (2009b).

### **3.2 Original Dodd and Restrepo Model**

The Dodd and Restrepo model is based on the true axial stress of the material, i.e. the stress defined as the ratio of the axial force over the cross-sectional area of the deformed bar. Due to the Poisson's effect, the cross-sectional area decreases when the axial strain is tensile and increases when the axial strain is compressive. Therefore, the true stress is calculated using the true cross-sectional area of the bar rather than the nominal which has been used in previous research. The Dodd and Restrepo model converts from an engineering coordinate system, which is calculated using the nominal area, to a natural coordinate system, which is calculated using the true area. This conversion is performed with equations (3.1) to (3.4). The conversion between coordinates is shown below. The strains and stresses in the natural coordinate space (or true

stress and strain) are denoted in the coordinate,  $(\varepsilon'_s, f'_s)$ . The coordinate of the strain and stress in the engineering coordinate space are denoted as  $(\varepsilon_s, f_s)$ .

$$\varepsilon'_s = \ln(1 + \varepsilon_s) \quad (3.1)$$

$$\varepsilon_s = e^{\varepsilon'_s} - 1 \quad (3.2)$$

$$f'_s = f_s(1 + \varepsilon_s) = f_s e^{\varepsilon'_s} \quad (3.3)$$

$$f_s = \frac{f'_s}{e^{\varepsilon'_s}} = \frac{f'_s}{1 + \varepsilon_s} \quad (3.4)$$

To calculate the relationship between the tangents of the stress-strain curve between the two coordinate systems, equation (3.5) is used.

$$\frac{df_s}{d\varepsilon_s} = \left( \frac{df'_s}{d\varepsilon'_s} - f'_s \right) e^{\varepsilon'_s} \quad (3.5)$$

The use of the natural coordinate system is advantageous because the tensile and compressive hysteretic curves become identical in these coordinates, simplifying calculations as shown in Figure 3.2.

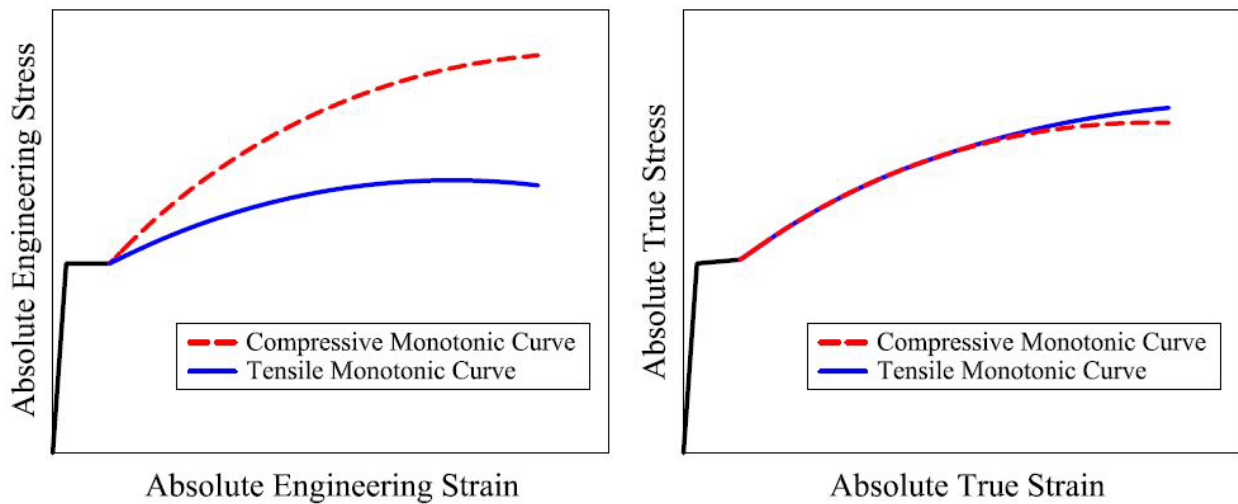


**Figure 3.2.** Comparison Between the Tensile and Compressive Stress-Strain Monotonic Behavior in (left) Natural Coordinates and (right) Engineering Coordinates (Dodd and Restrepo, 1995).

The monotonic stress strain behavior is defined by a piecewise function given by equations (3.6), (3.7) and (3.8) where the function changes at the true yield strain,  $\varepsilon'_y$ , and the true strain at the onset of strain hardening,  $\varepsilon'_{sh}$ . These equations are used to calculate the true stress,  $f'_s$ , in terms of true strain,  $\varepsilon'_s$ .

$$f'_s = E_s \varepsilon'_s \quad \text{if } |\varepsilon'_s| < |\varepsilon'_y| \quad (3.6)$$

$$f'_s = sf_y (1 + \varepsilon_s) = sf_y e^{\varepsilon'_s} \quad \text{if } |\varepsilon'_y| \leq |\varepsilon'_s| \leq |\varepsilon'_{sh}| \quad (3.7)$$

$$f'_s = s \left[ f'_{sh} + f'_{su} * (\varepsilon'_{su} - \varepsilon'_{sh}) - f'_{su} \right] \left( \frac{\varepsilon'_{su} - s [\varepsilon'_s - \varepsilon'_o(k)]}{\varepsilon'_{su} - \varepsilon'_{sh}} \right)^P \dots \quad (3.8)$$

$$\dots - f'_{su} * [s \varepsilon'_{su} - [\varepsilon'_s - \varepsilon'_o(k)]] + sf'_{su} \quad \text{if } |\varepsilon'_{sh}| \leq |\varepsilon'_s| \leq |\varepsilon'_{su}|$$

where  $f_y$  is the engineering stress at yield,  $f'_{sh}$  is the true stress at the onset of strain hardening,  $(\varepsilon'_{sh,1}, f'_{sh,1})$  is an arbitrary coordinate on the tensile true stress-strain curve,  $(\varepsilon'_{su}, f'_{su})$  is the true ultimate stress and strain,  $s$  and  $k$  denotes whether the curve is tensile ( $s = 1, k = 1$ ) or compressive ( $s = -1, k = 2$ ),  $\varepsilon'_o(k)$  is the shifted origin strain,  $f'_{su} *$  is the slope at the true ultimate stress and strain, and  $P$  is the power of the strain hardening curve as calculated using equation (3.9) (Dodd and Restrepo, 1995).

$$P = \frac{\log_{10} \left[ \frac{f'_{sh,1} + f'_{su} * (\varepsilon'_{su} - \varepsilon'_{sh,1}) - f'_{su}}{f'_{sh} + f'_{su} * (\varepsilon'_{su} - \varepsilon'_{sh}) - f'_{su}} \right]}{\log_{10} \left[ \frac{\varepsilon'_{su} - \varepsilon'_{sh,1}}{\varepsilon'_{su} - \varepsilon'_{sh}} \right]} \quad (3.9)$$

The reversal curve is computationally classified as either a major reversal or a minor reversal. As stated previously, a minor reversal is any reversal where the difference in true

stresses between the previous two reversal points is less than or equal to twice the yield stress. A major reversal would be any reversal where the difference is greater than twice the yield stress. A reversal from the strain hardening region would be considered a major reversal while a reversal from the yield plateau region would be considered a minor reversal as illustrated in Figure 3.3 (Dodd and Restrepo, 1995).

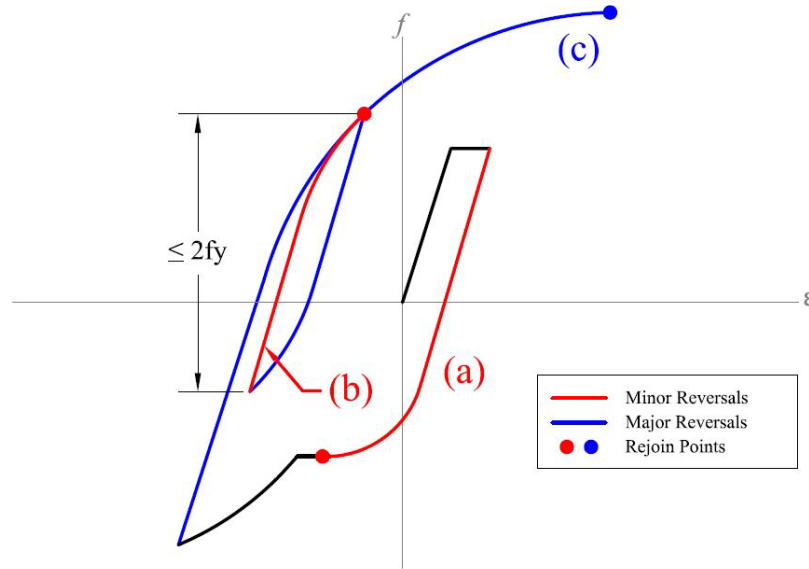


**Figure 3.3.** Illustration of (a) Reversals from the Yield Plateau, (b) Minor Reversals and (c) Major Reversals As Well As Their Respective Rejoin Points.

As shown in Figure 3.1, every reversal starts with an unloading branch, which simulates the behavior after a strain reversal until the true stress has decreased by a value equal to the yield stress. The reversal curve is linear until the coordinate,  $(\varepsilon'_a, f'_a)$ , which is calculated using equations (3.10) and (3.11) after a reversal at the coordinate,  $(\varepsilon'_r, f'_r)$ . The unloading branch is at a slope which is slightly different from the modulus of elasticity called the unloading modulus,  $E'_u$ . Dodd and Restrepo derived an empirical equation, (3.12), for calculating this value based on the maximum plastic strain,  $\varepsilon'_M$  (Dodd and Restrepo, 1995).

$$\varepsilon'_a = \varepsilon'_r + \frac{sf_y}{E'_u} \quad (3.10)$$

$$f'_a = f'_r + sf_y \quad (3.11)$$

$$E'_u = E_s \left( 0.82 + \frac{1}{5.55 + 1.000\varepsilon'_M} \right) \quad (3.12)$$

where  $E_s$  is the Young's Modulus of Elasticity.

After the unloading branch, the nonlinear reversal curve starts, and the coordinate at which the nonlinear reversal curve ends is calculated. This target, or “rejoin” coordinate depends on whether it is a major or minor reversal. The rejoin coordinates for a major reversal are calculated using equations (3.13) and (3.14) while the rejoin coordinates for a reversal from the yield plateau are calculated using equations (3.15) and (3.16) (Dodd and Restrepo, 1995).

$$f'_{rejoin} \approx sf'_{su} \quad (3.13)$$

$$\varepsilon'_{rejoin} \approx \varepsilon'_{su,shift} = s\varepsilon'_{su} + \varepsilon'_o(k) \quad (3.14)$$

$$f'_{rejoin} \approx sf_y \quad (3.15)$$

$$\varepsilon'_{rejoin} = \varepsilon'_r(m) + s \left[ \varepsilon'_o(2) - \varepsilon'_o(1) + \frac{2f_y}{E'_u} \right] \quad (3.16)$$

Equations (3.14) and (3.16) involve shifting the rejoin strain coordinate. As shown in Figure 3.4, the strain unloads to a non-zero value once the behavior becomes inelastic. To account for this shift in the strain, the rejoin strain coordinate also shifts. As shown in the equations, major reversal curves always end at the shifted ultimate coordinates, and a reversal curve from the yield plateau always ends at the yield plateau on the monotonic stress strain curve of the opposite sign. In a minor reversal, the curve rejoins the major reversal or minor reversal at the reversal coordinate one cycle prior (Dodd and Restrepo, 1995).



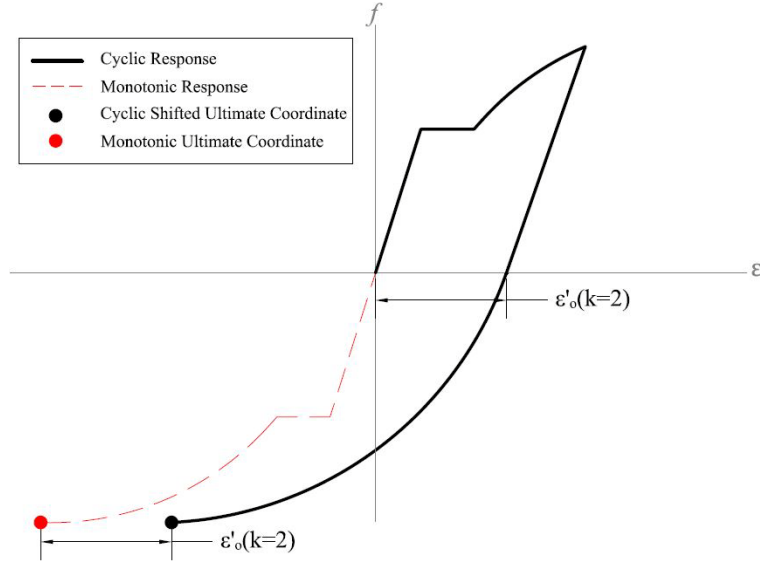


**Figure 3.4.** Illustration of the Shift in the Rejoin Coordinate After the Strain Unloads to a Non-Zero Value.

For minor reversals, the rejoin slope is merely the slope previously calculated at the reversal coordinate. For reversals from the yield plateau, the rejoin slope is zero (the slope of the yield plateau) in engineering coordinates, but it is equal to the yield stress in the natural coordinates. For major reversals, the slope in engineering coordinates is zero, the slope in natural coordinates is calculated using equation (3.17).

$$f'_{su} * = f_{su} e^{\varepsilon'_{su}} \quad (3.17)$$

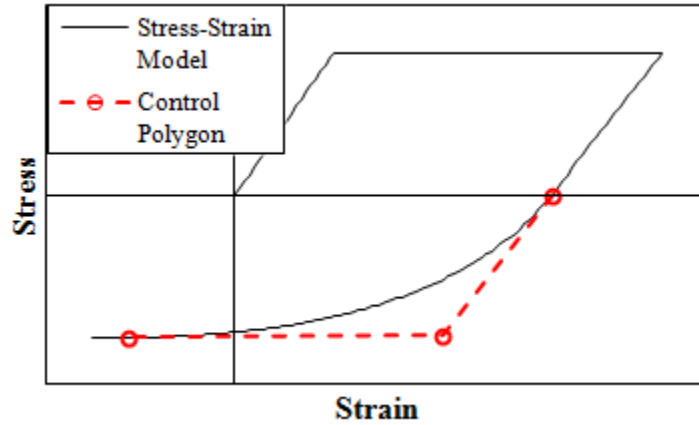
where  $f_{su}$  is the ultimate stress in engineering coordinates. This is important since the NURBS approximation uses the rejoin slopes as the slope of the final asymptote (Dodd and Restrepo, 1995).

### **3.3 NURBS Approximation to the Nonlinear Reversal Curve**

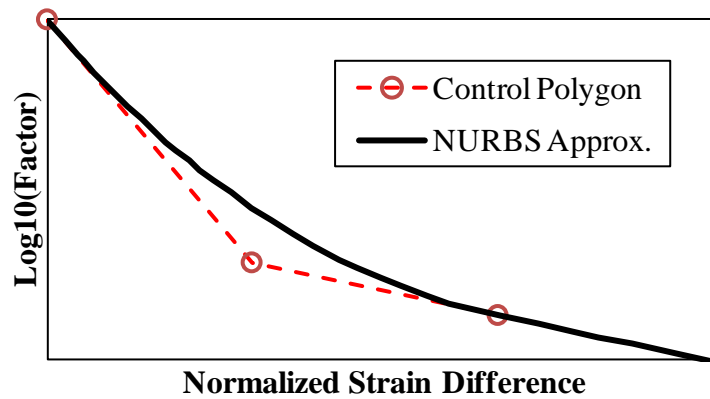
#### *3.3.1 Introduction to the NURBS approximation*

When simulating the nonlinear reversal curve, a NURBS curve is approximated in a normalized coordinate space to replace the iterative processes that are used in the Dodd and Restrepo model (Dodd and Restrepo, 1995). The algorithm used to calculate the NURBS curve is central to making the model more efficient than that proposed by Dodd and Restrepo (1995). For simplicity, the NURBS curve used in the proposed model is a second degree curve calculated with parametric equations. Figure 3.5 shows two examples where NURBS curves are used in this model.

The parametric equations are made up of three polynomials which interpolate the curve within a control polygon made up of three control points. The derivation of these polynomials is discussed further in Appendix A. The coordinates in the curve interpolates between the coordinates at the vertices of the structure known as the control polygon. The control polygon used in the proposed model is made up of three control points and two lines which represent the beginning and final tangent of the curve (Piegl and Tiller, 1997).



(a) Control Polygon and NURBS Approximation of a Reversal from the Yield Plateau.



(b) Logarithm of Buckling Strength Degradation Factor and Strain Normalized To The Buckling Strain.

**Figure 3.5.** Examples of the Implementation of the NURBS Approximation.

The second degree curve begins and ends at the first and last control point respectively. Furthermore, the curve is tangent to the control polygon at the beginning and end of the curve. The general form of the NURBS-based interpolation equations are shown in equations (3.18) and (3.19).

$$C(u) = \frac{(1-u)^2 w_0 P_0 + 2u(1-u) w_1 P_1 + u^2 w_2 P_2}{(1-u)^2 w_0 + 2u(1-u) w_1 + u^2 w_2} \quad (3.18)$$

$$C(u) = (1-u)^2 P_0 + 2u(1-u) P_1 + u^2 P_2 \quad (3.19)$$

where  $P_0$ ,  $P_1$  and  $P_2$  are the three vertices, or control points, of the control polygon and  $w_0$ ,  $w_1$  and  $w_2$  are the weights applied to the control points (Piegl and Tiller, 1997).

Equation (3.19) is a special version of equation (3.18) where all of the weights are equal to one. Weights will not always be needed in the proposed model, so it's necessary to simplify the equation in the beforehand. Also note that these are parametric equations with a common independent variable,  $u$ . For example, to solve for stress, it is necessary to put the term,  $u$ , in terms of strain (Piegl and Tiller, 1997). The equations used for NURBS approximations in the proposed model are variations of these equations.

### 3.3.2 NURBS-Based Interpolation Equations

The proposed model calculates the NURBS curve in a normalized, dimensionless coordinate space. Specifically, the strain and stress are normalized to the range of true strain and true stress along the nonlinear reversal curve with equations (3.20) and (3.21).

$$f'' = \frac{f'_s - f'_a}{f'_{rejoin} - f'_a} \quad (3.20)$$

$$\varepsilon'' = \frac{\varepsilon'_s - \varepsilon'_a}{\varepsilon'_{rejoin} - \varepsilon'_a} \quad (3.21)$$

where  $(\varepsilon'_a, f'_a)$  is the coordinate start of the nonlinear reversal curve,  $(\varepsilon'_{rejoin}, f'_{rejoin})$  is the coordinate at the end, and  $(\varepsilon'_s, f'_s)$  is the coordinate at the current step.

The normalized coordinates at the end of the NURBS curve are always at (1, 1). Once the coordinates have been transformed, and the control points determined, the normalized stress can be obtained from the normalized strain using the following equations.

$$f''(u) = (1-u)^2 f''_1 + 2u(1-u) f''_j + u^2 \quad (3.22)$$

$$\text{where } u(\varepsilon'') = \frac{-\left(2(\varepsilon''_j - \varepsilon''_1)\right) + \sqrt{\left(2(\varepsilon''_j - \varepsilon''_1)\right)^2 - 4(1 - 2\varepsilon''_j + \varepsilon''_1)(\varepsilon''_1 - \varepsilon'')}}{2(1 - 2\varepsilon''_j + \varepsilon''_1)} \quad (3.23)$$

The two tangents lines in the control polygon of the NURBS curve are the linear continuation of the unloading portion of the reversal curve and the tangent to the rejoin coordinate that passes through the end of the nonlinear reversal curve. The slopes of these two tangents are equal to the unloading modulus and the slope at the rejoin coordinate converted in the normalized coordinate space through chain rule of differentiation as shown in (3.24).

$$\frac{df''}{d\varepsilon''} = \frac{df'_s}{d\varepsilon'_s} \frac{df''}{df'_s} \frac{d\varepsilon'_s}{d\varepsilon''} = \frac{df'_s}{d\varepsilon'_s} \left( \frac{\varepsilon'_{rejoin} - \varepsilon'_a}{f'_{rejoin} - f'_a} \right) \quad (3.24)$$

The control point coordinates are  $(\varepsilon''_1, f''_1)$ ,  $(\varepsilon''_j, f''_j)$ , and (1,1). The second control point is defined as the coordinate where the two asymptotes cross, which is calculated using equations (3.25) and (3.26).

$$\varepsilon''_j = \frac{\left(1 - \frac{f'_{rejoin} * (\varepsilon'_{rejoin} - \varepsilon'_a)}{f'_{rejoin} - f'_a}\right)}{\left(\frac{E'_u - f'_{rejoin} *}{f'_{rejoin} - f'_a}\right) (\varepsilon'_{rejoin} - \varepsilon'_a)} \quad (3.25)$$

$$f''_j = \varepsilon''_j \frac{E'_u (\varepsilon'_{rejoin} - \varepsilon'_a)}{f'_{rejoin} - f'_a} \quad (3.26)$$

where  $f'_{rejoin} *$  is the slope at the end of the reversal curve.

The first control point,  $(\varepsilon''_1, f''_1)$ , is  $(0,0)$  in minor reversals. In major reversals, the first control point is delayed to  $(\varepsilon''_k, f''_k)$  and the stress response until that point is linear with a slope equal to the first tangent as shown in Figure 3.6. The first control point in a major reversal is calculated using equations (3.27) and (3.28).

$$\varepsilon''_k = b\varepsilon''_j(2-b) \quad (3.27)$$

$$f''_k = bf''_j(2-b) \quad (3.28)$$

The calculation of  $b$  is based on the properties of the material and the natural stress and strain ranges of the reversal curve. The calculation as well as the calibration of  $b$  are explained in full detail in Appendix B.

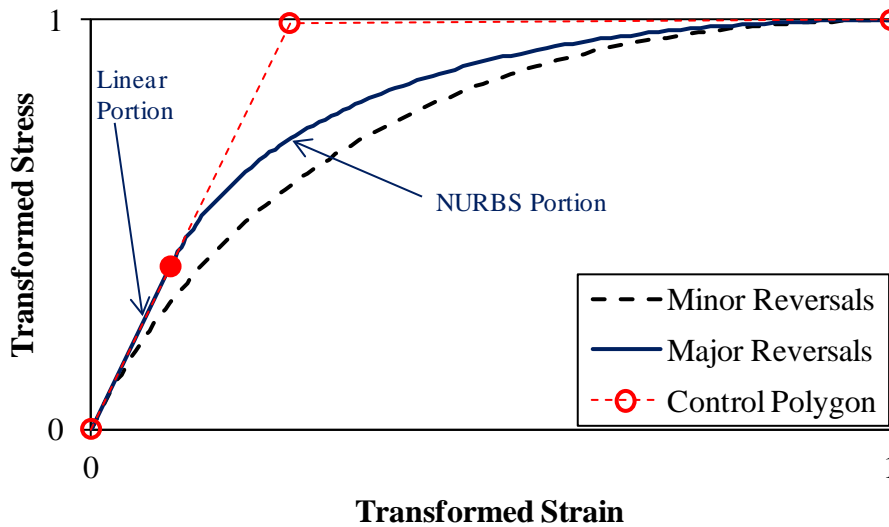
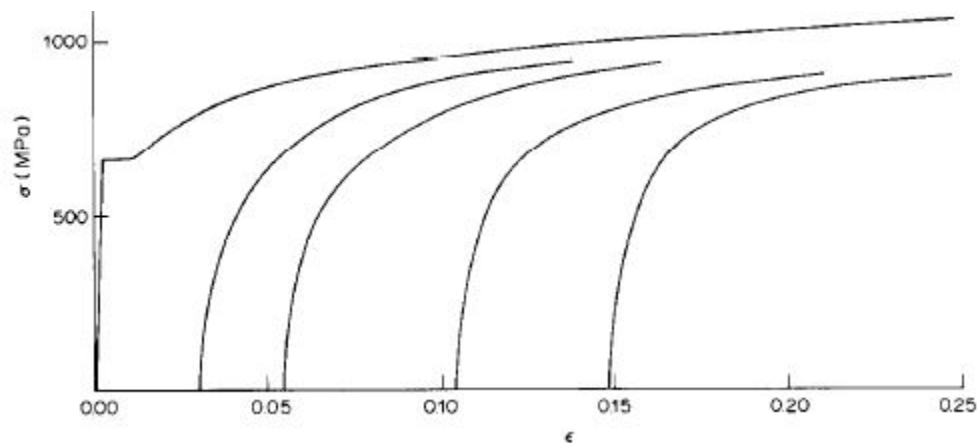


**Figure 3.6.** Illustration of Minor and Major Reversals in the Normalized Coordinate Space.

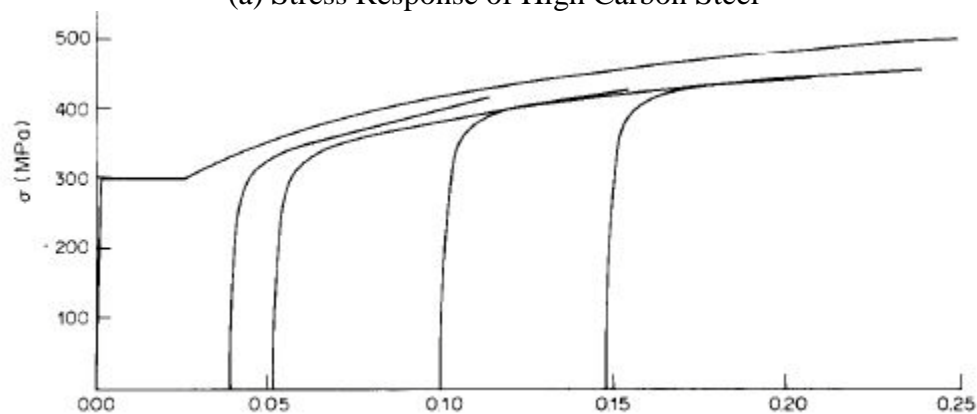
### 3.3.3 Effect of Carbon Content on the Nonlinear Reversal Curve

It is important to note that the Dodd and Restrepo model was calibrated to specimens with similar carbon content (0.19%-0.25%) (Restrepo et al., 1994). Therefore, the proposed model is calibrated to these specimens. As stated by Wilson and Bate (1986), the carbon content

in the steel significantly affects the Bauschinger effect in the steel as shown in Figures 3.7a and b.



(a) Stress Response of High Carbon Steel



(b) Stress Response of Low Carbon Steel

**Figure 3.7.** Cyclic Test Results Plotted in Terms of Absolute Stress and Strain  
Wilson, D.V. and Bate, P.S. (1986). "Reversibility in the Work Hardening of Spheroidised Steels." *Acta Metallurgica*, 34(6), 1107-1120. Used under fair use, 2014.

This would be a significant problem if ASTM A615 reinforcing steel were widely used in earthquake-prone areas since ASTM doesn't have a standard carbon content for A615 reinforcing bar (ASTM A615/A615M, 2013). However, A706 reinforcing bar is more widely used because ASTM caps its carbon content at 0.33% (ASTM A706/A706M, 2013). The low carbon content gives the reinforcing bar more ductility, which is desirable in high seismic zones.

Since the specimens used in Dodd and Restrepo's experiments were below this limit, their model is applicable for the purposes of cyclic response modeling. Still, this poses a problem for verification since the experimental data that some analyses are compared with involved specimens with no required or known carbon content. A temporary measure has been used to adequately verify the proposed model as specified in a later section.

### **3.4 Simulating the Effects of Inelastic Buckling**

#### *3.4.1 Simulating the Effects of Inelastic Buckling*

Unlike existing material models, the strength degradation due to inelastic buckling is accounted for in this proposed model by applying a factor to the stress after it has been calculated in the hysteretic stress-strain law. This factor is only applied after the onset of buckling is determined. Most existing material models do not calculate the strain or stress at the onset of buckling. For the material models that do calculate the coordinate at the onset of buckling, the current methods wouldn't apply to the proposed model because the approach is different in concept and implementation (Dhakal and Maekawa, 2002a and b)(Gomes and Appleton, 1997) (Urmson and Mander, 2012).

The proposed method to determine the onset of buckling involves treating the reinforcing bar as a beam element with a non-uniform stress profile along the cross-section. This approach is similar to the approach used by Urmson and Mander (2012), but it doesn't require the integration of the stress-distribution. Urmson and Mander (2012) required integration because they attempted to calculate the non-linear stress distribution at every step in strain (Urmson and Mander, 2012).

This method makes several assumptions:



- The reinforcing bar is initially straight.
- The reinforcing bar is fixed at the confinement ties.
- The unbraced length of the reinforcing bar is the spacing between the confinement ties.
- The reinforcing bar is completely exposed after the concrete has spalled off along its entire unbraced length.
- The lateral deflection of the steel reinforcing bar at the onset of buckling varies co-sinusodally between consecutive ties.

It should also be noted that for this portion of the analysis, the diameter of the reinforcing bar is assumed to be constant. Therefore, any values of strain and stress are calculated in the engineering coordinates. An illustration of these assumptions are shown in Figure 3.8.

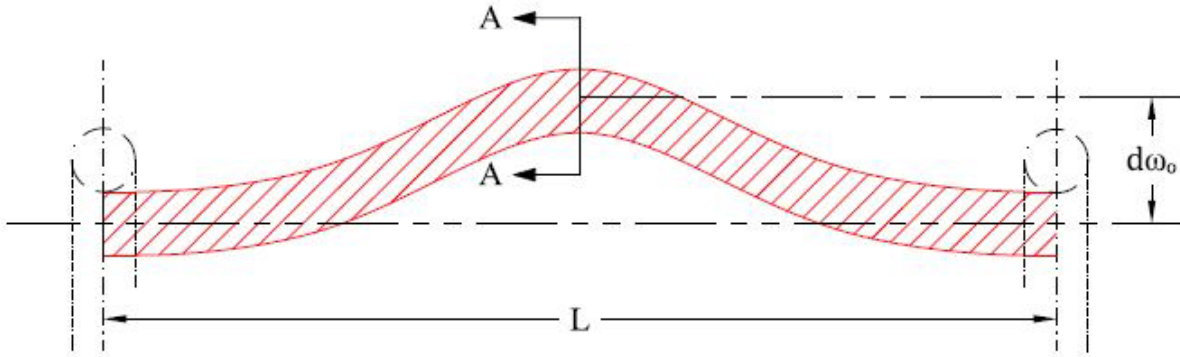


**Figure 3.8.** Buckled shape of the isolated reinforcing bar between two confinement ties.

The reduced modulus theory proposed by Engesser, as mentioned by Chen and Liu (1936), states that any non-linear distribution of stresses can be represented as the sum of linear distributions of the change in stresses along the cross section as illustrated in Figure 3.9. Observe that every linear distribution has a different neutral axis location, creating the non-linear shape after the summation. Since the beam element analysis involved only examines the change in

axial force and moment, the proposed model only focuses on the linear distribution of the change in stresses along the cross-section of the beam. Not only will analyzing a linear distribution be mathematically simple, but it is also valid according to Engesser's theory (Chen and Liu, 1936).

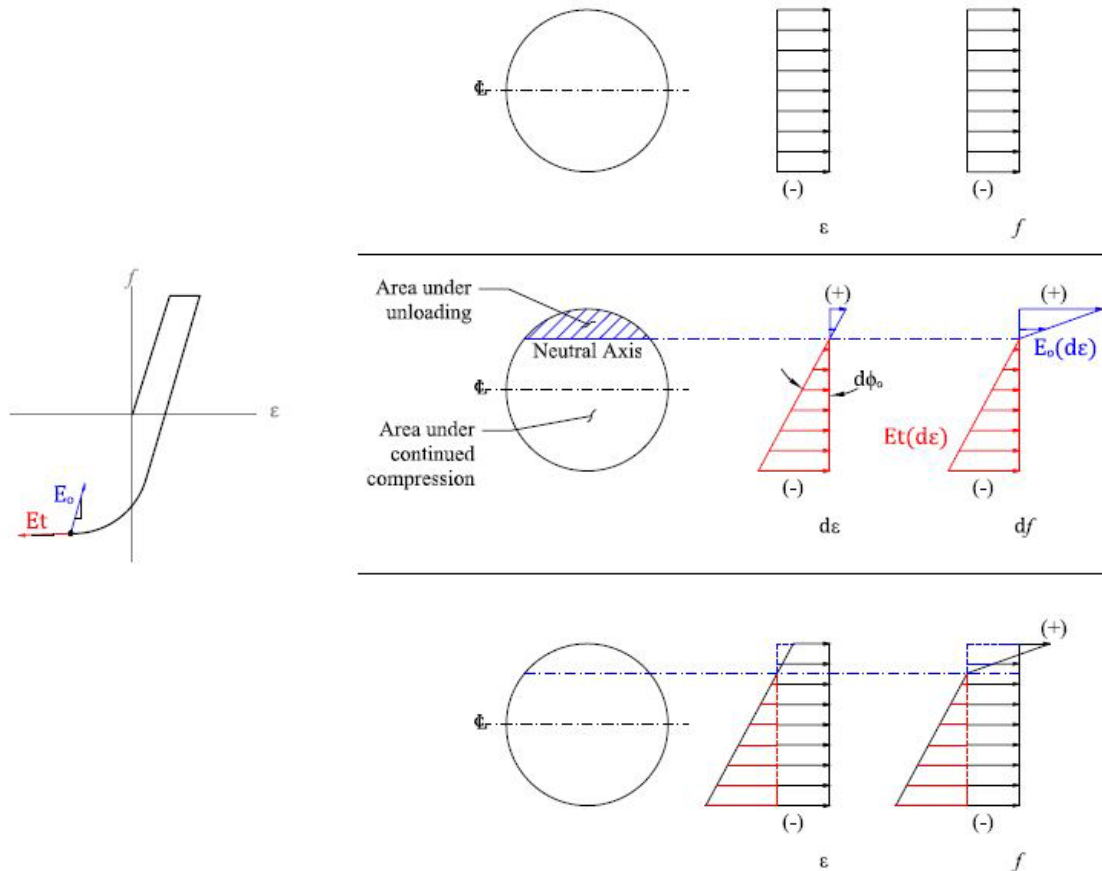


**Figure 3.9.** Example of the Reduced Modulus Theory Implemented in the Proposed Model Starting with (top) the Reinforcing Bar with a Uniform Stress Distribution, then Adding a Change in Stress Distribution (middle), and Resulting in the Nonlinear Stress Distribution Shown in the Bottom.

At every step in strain, the linear distribution of the change in stresses is calculated and analyzed. This distribution changes at every step because the location of the neutral axis changes. This varying location also affects the stiffness the reinforcing bar because one side of the neutral axis experiences different stress-strain behavior as the other side. The proposed method needs the stiffness because it relates the strain and curvature to the axial force and moment. The onset of

buckling is defined as the point at which the net change in axial stress due to a change in axial strain is zero. It initially assumes that the change in axial stress is zero and verifies that assumption. If the assumption is correct and then the model attributes the strain at that step to the onset of buckling.

The method calculates the distribution of the change in stress along the cross section of the reinforcing bar midway between confinement ties. The portion of the reinforcing bar under a tensile change in stress will be essentially unloading while the portion of the reinforcing bar under a compressive change in stress will be continuing in the stress-strain curve. Because of this the behavior of these sections are governed by different moduli: the tensile change in stresses is governed by the unloading modulus calculated using (3.12), and the compressive change is governed by the current tangent to the stress-strain curve. Therefore, the linear distribution of the change in stresses can be calculated by multiplying the change in strain by the appropriate modulus as previously shown in Fig. 3.9.

With the known moduli and equilibrium, it is possible to find the distance between the neutral axis and the extreme compression face of the reinforcing bar. Once this is found through equilibrium, the stiffness parameters of the reinforcing bar can be determined. Finding the location of the neutral axis analytically requires an iterative process as that would require finding the volume of a cylindrical wedge (the shape of the three dimensional stress distribution), which is a computationally taxing process. Computational efficiency is a major objective in this study; so a NURBS approximation has been derived to calculate the ratio of the location of the neutral axis to the diameter of the bar. This ratio varies with another ratio, of the tangent to the stress-strain curve to the unloading modulus transformed into engineering coordinates. This approximation is calibrated to the analytical values of the location of the neutral axis. This is a

sufficient algorithm to predict the ratio when compared with the analytical method, eliminating the need for the iterative process as shown in equations (3.29), (3.30) and (3.31). The approximation is found to provide very accurate results, as shown in Appendix E.

$$\bar{y} = D \frac{-0.32u^2 + 0.22u + 0.5}{-0.7u^2 + u + 0.5} \quad (3.29)$$

$$\text{where } u = \frac{-\eta - \sqrt{\eta^2 - 2(-0.7\eta - 0.8)\eta}}{2(-0.7\eta - 0.8) \sqrt{\quad}} \quad (3.30)$$

$$\text{and } \eta = \frac{\bar{E}_t}{E_o} \quad (3.31)$$

where  $D$  is the diameter of the bar and  $E_o$  refers to the unloading modulus transformed into engineering coordinates.

Once the location of the neutral axis is calculated, the stiffness parameters can be calculated and the matrix analysis of the reinforcing bar as a beam element can be set up. The change in axial force and moment is related to the change in strain and curvature with a sectional tangent stiffness matrix as shown in expression (3.32).

$$\begin{Bmatrix} dN \\ dM \end{Bmatrix} = [\hat{D}_T] \begin{Bmatrix} d\varepsilon_o \\ d\phi_o \end{Bmatrix} = \begin{bmatrix} \frac{\partial N}{\partial \varepsilon_o} & \frac{\partial N}{\partial \phi_o} \\ \frac{\partial M}{\partial \varepsilon_o} & \frac{\partial M}{\partial \phi_o} \end{bmatrix} \begin{Bmatrix} d\varepsilon_o \\ d\phi_o \end{Bmatrix} = \begin{bmatrix} \iint_A E_t dS & \iint_A -yE_t dS \\ \iint_A -yE_t dS & \iint_A y^2 E_t dS \end{bmatrix} \begin{Bmatrix} d\varepsilon_o \\ d\phi_o \end{Bmatrix} \quad (3.32)$$

where  $dN$  is the change in axial stress,  $dM$  is the change in moment,  $d\varepsilon_o$  is a change in axial strain,  $d\phi_o$  is the change in the change in curvature at midspan,  $\hat{D}_T$  is the sectional tangent stiffness matrix,  $y$  is the vertical location along a cross section,  $A$  is the cross-sectional area and  $E_t$  is the sectional modulus. However, there are three unknowns in (3.32) where ideally we

would have just one: the change in axial force. Several substitutions must be made before this analysis can happen.

The first change to (3.32) is to put the change in moment in terms of change in axial force. Due to lateral deflections, the bar is bound to experience p-delta effects as shown in Figure 3.10.

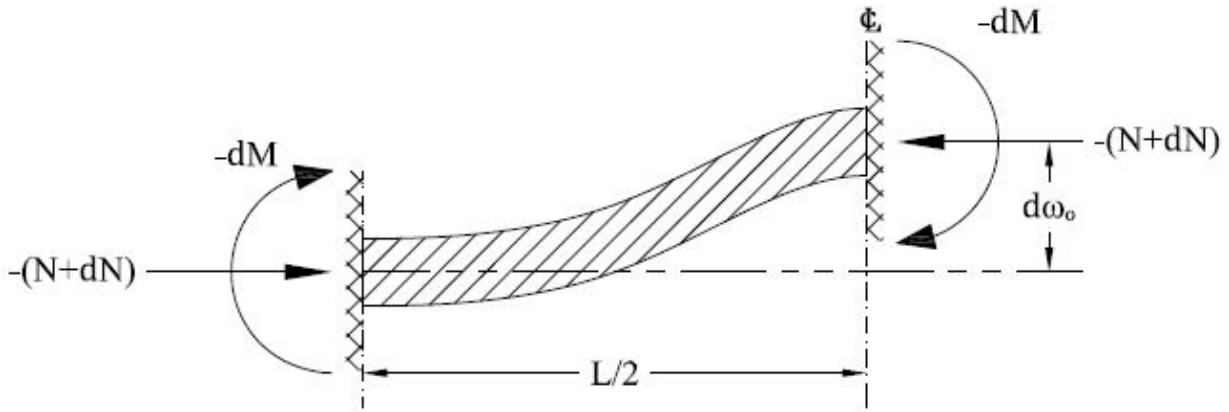


**Figure 3.10.** Free Body Diagram of Half of the Buckled Shape of the Reinforcing bar. The signs are positive for Tensile Forces and Counter-Clockwise Rotations While the Orientations Drawn Reflect the Predicted Response.

Since the buckled shape of the reinforcing bar is assumed to complete a full co-sinusoidal period between the confinement ties, the curvature at midspan and the curvature at the centerline of the ties are equal and opposite. This means that the internal moments at those same locations are also assumed to be equal and opposite. Examining the reinforcing bar for moment equilibrium yields the following expression.

$$\sum M = 0 = -(N + dN)d\omega_o + 2dM$$

This expression is used to put the change in moment in terms of the axial force.

$$dM = \frac{(N + dN)d\omega_o}{2} \tag{3.33}$$

Observe the second row of (3.32).

$$dM = \hat{D}_{T,21}d\varepsilon_o + \hat{D}_{T,22}d\phi_o$$

where  $\hat{D}_{T,21}$  refers to the element in the second row and first column in the stiffness matrix.

Substituting in expression (3.33) for  $dM$  gives the following expression.

$$\frac{(N + dN)d\omega_o}{2} = \hat{D}_{T,21}d\varepsilon_o + \hat{D}_{T,22}d\phi_o$$

There are three unknowns in this expression. Ideally, it would only have two unknowns,  $d\varepsilon_o$  and  $d\phi_o$ , so that the equation could be substituted into the first row of (3.32). This way an equation for the change in axial force due to a change in axial strain can be derived.

The next relationship to find, therefore, is between the change in curvature,  $d\phi_o$ , and the change in lateral deflection,  $d\omega_o$ , at midspan. Because the buckled shape is assumed to be symmetrical and fixed at the confinement ties, the slope at the confinement ties and midway between is assumed to be zero. The following expression comes from these assumptions.

$$d\omega = \frac{-1}{2}d\omega_o \cos\left(\frac{2\pi}{L}x\right) \quad (3.34)$$

where  $d\omega$  is the lateral deflection at a distance,  $x$ , along the beam and  $L$  is the spacing between the confinement ties. The second derivative of equation (3.34) is put in terms of the change in curvature as shown in equation (3.36).

$$\frac{d(d\omega)}{dx} = \frac{\pi}{L}d\omega_o \sin\left(\frac{2\pi}{L}x\right) \quad (3.35)$$

$$\frac{d^2(d\omega)}{dx^2} = 2\left(\frac{\pi}{L}\right)^2 d\omega_o \cos\left(\frac{2\pi}{L}x\right) = d\phi \left(1 + \left(\frac{d(d\omega)}{dx}\right)^2\right)^{3/2} \quad (3.36)$$

Because the lateral deflection,  $d\omega_o$ , and curvature  $d\phi_o$  are only observed at midspan, half of the length is plugged into  $x$ , and  $\frac{d(d\omega)}{dx}$  is equal to zero at midspan as previously stated in the assumptions. The curvature term,  $d\phi$ , is replaced with the midspan curvature term,  $d\phi_o$ . Equation (3.37) is the result of all of these substitutions.

$$d\phi_o = -2\left(\frac{\pi}{L}\right)^2 d\omega_o \quad (3.37)$$

(3.37) is substituted into the aforementioned second row of (3.32) to give the following expression.

$$\frac{(N + dN)}{2} \left( \frac{-d\phi_o L^2}{2\pi^2} \right) = \hat{D}_{T,21} d\varepsilon_o + \hat{D}_{T,22} d\phi_o$$

This is rearranged to find the relationship between the midspan curvature and the axial strain as shown in equation (3.38). Also, this is where the term,  $dN$ , is assumed to be zero as previously mentioned.

$$d\phi_o = \left( \frac{\hat{D}_{T,21}}{\frac{-NL^2}{4\pi^2} - \hat{D}_{T,22}} \right) d\varepsilon_o \quad (3.38)$$

(3.38) is substituted into the first row of (3.32) to give the following expression.

$$dN = \hat{D}_{T,11} d\varepsilon_o + \hat{D}_{T,12} d\phi_o = \hat{D}_{T,11} d\varepsilon_o + \hat{D}_{T,12} \left( \frac{\hat{D}_{T,21}}{\frac{-NL^2}{4\pi^2} - \hat{D}_{T,22}} \right) d\varepsilon_o$$

The term,  $d\varepsilon_o$ , is then factored out and brought to the other side to create an expression for the change in axial force due to a change in axial strain.

$$\left(\frac{dN}{d\varepsilon_o}\right)_{\text{condensed}} = \hat{D}_{T,11} - \frac{(\hat{D}_{T,12})^2}{\frac{NL^2}{4\pi^2} + \hat{D}_{T,22}} \quad (3.39)$$

The subscript label “condensed” is there to distinguish this term from the  $\frac{\partial N}{\partial \varepsilon_o}$  term in the section tangent stiffness matrix in that the condensed form accounts for a change in curvature as well. Also since  $\hat{D}_{T,12}$  equals  $\hat{D}_{T,21}$ , there is no need to treat them as separate terms.

Equation (3.39) is used to determine whether a further increase in compressive axial strain leads to no change or decrease of the axial force, at which buckling is assumed to occur. If (3.39) yields a zero value (or a slightly negative value), then buckling has occurred. There are cases where (3.39) doesn't seem to ever yield zero. In these cases, (3.39) will seem to approach zero, reach a local minima, and then start increasing again. This indicates that the strain step is too large to find the precise strain at which buckling occurs. At a certain strain step, the compressive axial force becomes so large that the denominator of the term in (3.39) becomes negative. This means that at some point between the current step and the one previous, the denominator was small enough that (3.39) yielded a zero value. For cases like these, a negative denominator is another criterion for the onset of buckling.

While the elements of the stiffness matrix could be found through a direct calculation analytically, a NURBS approximation is also used to determine these values at every step to simplify calculations and further increase computational efficiency. To generalize the approximations to any material and geometric properties, NURBS actually is calculating a series of variables  $\gamma_{T,11}$ ,  $\gamma_{T,12/21}$  and  $\gamma_{T,22}$ , which are related to the tangent stiffness matrix as shown in equations (3.40), (3.41) and (3.42).



$$\hat{D}_{T,11} = \iint_A E_t dS = \gamma_{T,11} E_o \pi \left( \frac{D}{2} \right)^2 \quad (3.40)$$

$$\hat{D}_{T,12/21} = \iint_A -y E_t dS = \gamma_{T,12/21} E_o \pi \left( \frac{D}{2} \right)^3 \quad (3.41)$$

$$\hat{D}_{T,22} = \iint_A y^2 E_t dS = \gamma_{T,22} E_o \pi \left( \frac{D}{2} \right)^4 \quad (3.42)$$

Therefore, equation (3.39) turns into the following expression:

$$\left( \frac{dN}{d\varepsilon_o} \right)_{condensed} = \gamma_{T,11} E_o \pi \left( \frac{D}{2} \right)^2 - \frac{\left( \gamma_{T,12/21} E_o \pi \left( \frac{D}{2} \right)^3 \right)^2}{\frac{NL^2}{4\pi^2} + \gamma_{T,22} E_o \pi \left( \frac{D}{2} \right)^4}$$

With the diameter of the reinforcing bar and the unloading modulus factored out, the only variable affecting  $\gamma_{T,11}$ ,  $\gamma_{T,12/21}$  and  $\gamma_{T,22}$  is  $\eta$ , the tangent ratio,  $\eta$ . After conducting curve fitting with analytical results as described in Appendix E, the following expressions have been obtained:

$$\gamma_{T,11}(\eta) = \frac{0.04 - \sqrt{0.0016 + 3.84\eta}}{-1.92} \quad (3.43)$$

$$\gamma_{T,12}(u_{T,12/21}) = \gamma_{T,12}(u_{T,12/21}) = \frac{-0.546(u - u^2)}{0.44u^2 - 0.44u + 1} \quad (3.44)$$

$$\text{where } u_{T,12/21}(\eta) = \frac{0.44\eta + 0.3432 - \sqrt{(-0.44\eta - 0.3432)^2 - 4\eta(0.44\eta - 0.6568)}}{2(0.44\eta - 0.6568)} \quad (3.45)$$

$$\gamma_{T,22}(u_{T,22}) = -0.03u^2 + 0.28u \quad (3.46)$$

$$\text{where } u_{T,22}(\eta) = \frac{0.3 - \sqrt{0.09 + 2.8\eta}}{-1.4} \quad (3.47)$$

With these equations, the entirety of this check can be determined with the ratio of moduli and the diameter of the reinforcing bar.

### 3.4.2 Calculating the Buckling Strength Degradation Factor

If the reinforcing bar has buckled, the strength degradation factor must be calculated. The factor is determined through a relationship found between the logarithm (base 10) of the factor and the compressive strain normalized to the difference between the strain at buckling,  $\epsilon_b$ , and the negative of the ultimate strain as shown in equation (3.48). This relationship is calibrated to experimental monotonic tests performed by Bayrak and Sheikh (2001), Mander et al. (Dhakal and Maekawa, 2002ab), and Bae et al. (2005). The relationship is dependent on the slenderness ratio as well as the material properties as Dhakal and Maekawa have discovered in their work (2002ab). This calibration process is described in further detail in Appendix F.

$$\epsilon_n = \frac{\epsilon_b - \epsilon_s}{\epsilon_b - \epsilon_{su}} \quad (3.48)$$

As previously shown in Figure 3.5b, this relationship is approximated with NURBS and has two varying parameters: the slope of the initial asymptote (M1) and the logarithm of the factor at a normalized strain of 1 ( $f2$ ). These parameters can be calculated using equations (3.49) and (3.50).

$$M1 = -0.1208 \frac{L}{D} \sqrt{P} + 0.868 \leq 0 \quad (3.49)$$

$$f2 = -0.1 \frac{L}{D} + 0.2778 \quad (3.50)$$

The slope of the final asymptote,  $M2$ , has been found to be constant at -0.17034. With the two asymptotes, the first control point and last control point known as  $(0,0)$  and  $(1, f_2)$  respectively, the second control point is calculated using equations (3.51) and (3.52).

$$\varepsilon_{n1} = \frac{f_2 - M2}{M1 - M2} \quad (3.51)$$

$$f_1 = M1\varepsilon_{n1} \quad (3.52)$$

After the control points and slopes are calculated, a NURBS approximation is derived to calculate the logarithm of the strength degradation factor using equations (3.53), (3.54) and (3.55). It should be noted that the NURBS approximation only calculates the factor between the strain at onset of buckling and the negative ultimate strain. After the negative ultimate strain, the logarithm varies linearly with normalized strain. However, there is a chance that equation (3.51) will yield a value not between 0 and 1. In this case, the logarithm will be calculated with equation (3.56). Finally, to account for the residual strength in the reinforcing bar, the factor shall not lead to a stress below 20% the yield stress of the material. This plateau is calculated with equation (3.57) and is based on observations by Dhakal and Maekawa (2002 ab). The summary of the calculation of  $\log_{10} f_b$  is shown below.

If  $0 \leq \varepsilon_{n1} \leq 1$

$$\log_{10} f_b = 2u(1-u)f_1 + u^2 f_2 \quad 0 \leq \varepsilon_n \leq 1 \quad (3.53)$$

$$\text{where } u(\eta) = \frac{-\varepsilon_{n1} - \sqrt{\varepsilon_{n1}^2 + \varepsilon_n(1-2\varepsilon_{n1})}}{(1-2\varepsilon_{n1})} \quad (3.54)$$

$$\log_{10} f_b = M2(\varepsilon_n - 1) + f_2 \quad \varepsilon_n > 1 \quad (3.55)$$

Otherwise

$$\log_{10} f_b = M1\varepsilon_n \quad (3.56)$$

$$\text{if } f_s < 0.2f_y \quad f_b = \frac{0.2f_y}{f_s} \quad (3.57)$$

After this,  $f_b$  is found by calculating 10 to the power of the logarithm, and then it is applied to the stress calculated in the stress-strain law. The factored stress is saved as a separate history value in order to not interfere with the stress strain law. When the reinforcing bar is in tension after the onset of buckling, the factor of the stress is also calculated using equations (3.53) to (3.57) until the reinforcement bar returns to the strain at the onset of buckling. This allows for a simple calculation by stating that there is a unique value of  $f_b$  for every value of  $\varepsilon_n$  in compression or in tension.

### 3.4.3 Application to Other Material Models

Because this buckling strength degradation factor is calculated outside of the stress strain law, it can be applied to any model which calculates the tangent of the stress-strain curve at each step. The only complication that might arise is the inclusion of the power of the strain hardening curve as calculated in the Dodd and Restrepo code. Many material models use the initial tangent of the strain hardening curve ( $E_{sh}$ ) to calculate the strain hardening curve. The following derivation shows an expression for the power in terms of the initial tangent.

$$E_{sh} = \frac{df_s}{d\varepsilon_s}(\varepsilon_{sh}) = \frac{df_s}{df'_s} \frac{d\varepsilon'_s}{d\varepsilon_s} \left[ \frac{df'_s}{d\varepsilon'_s}(\varepsilon'_{sh}) \right] \quad (3.58)$$

The derivation starts with the derivative of the equation of the strain hardening curve (3.8) to get (3.59).

$$\frac{df'_s}{d\varepsilon'_s} = Ps \left[ f'_{sh} + f'_{su} * (\varepsilon'_{su} - \varepsilon'_{sh}) - f'_{su} \right] \left( \frac{\varepsilon'_{su} - s[\varepsilon'_s - \varepsilon'_o(k)]}{\varepsilon'_{su} - \varepsilon'_{sh}} \right)^{P-1} + f'_{su} * \quad (3.59)$$

Because  $E_{sh}$  is the tangent of the tensile strain hardening curve at virgin loading,  $s = +1$  and  $\varepsilon'_o(k) = 0$ . Substituting  $\varepsilon'_s$  with  $\varepsilon'_{sh}$  will get the following expression.

$$\frac{df'_s}{d\varepsilon'_s}(\varepsilon'_{sh}) = P \left[ f'_{sh} + f'_{su} * (\varepsilon'_{su} - \varepsilon'_{sh}) - f'_{su} \right] + f'_{su} *$$

Now, to get the other terms in equation (3.58), (3.1) was derived in terms of  $\varepsilon_s$  and (3.4)

was derived in terms of  $f'_s$ .

$$\frac{df'_s}{df'_s} = \frac{d\varepsilon'_s}{d\varepsilon_s} = \frac{1}{1 + \varepsilon_s} \quad (3.60)$$

By substituting  $\varepsilon'_s$  with  $\varepsilon'_{sh}$  and combining equations (3.58), (3.59) and (3.60) together, the final expression for  $P$  is formed.

$$P = \frac{E_{sh} (1 + \varepsilon_{sh})^2 - f'_{su} *}{f'_{sh} + f'_{su} * (\varepsilon'_{su} - \varepsilon'_{sh}) - f'_{su}} \quad (3.61)$$

When applying the proposed considerations for inelastic buckling to other material models, it is important to calculate the material properties in the natural coordinate space. The equations to solve for these can be found in the original Dodd and Restrepo model (1995). Finally, when calculating  $E_o$ , use the initial tangent of the compression reversal curve or the young's modulus for simplicity.

### 3.5 Accounting for Low-Cycle Fatigue

When steel is subjected to high axial loads, then the steel develops cracks at a microscopic level due to ductile damage. This is worsened in the case of cyclic loading with energy dissipation from plastic deformation. As the steel is continually loaded in the tensile region, the microscopic cracks grow and coalesced. When the microvoids become big and

numerous, macroscopic cracks appear indicating failure. Once a macroscopic crack occurs, the capacity of the steel is greatly decreased and rupture will follow shortly in sections with relatively small cross-sectional areas such as reinforcing bars. Huang and Mahin (2010) have incorporated a method to simulate this failure, and this method is chosen for the proposed model. This method is preferable above the Coffin-Manson/Miner algorithms used is Kunnath's model because it doesn't require as much computer memory (Kunnath et al. 2009ab). Furthermore, the proposed considerations for low-cycle fatigue are separate from the stress-strain law just as the considerations for buckling are. This prevents numerical convergence failure and can be applied to other material models with ease.

The method involves updating the damage parameter,  $D_m$ , only when the true stress is tensile. When the updated parameter is greater than a material property,  $D_{crit}$ , then the material is considered ruptured. Equations (3.62) to (3.66) describe the process of updating the damage parameter by observing the true stress halfway between the newly calculated true stress,  $f'_{n+1}$ , and the true stress of the previous step,  $f'_n$ . The plastic strain increment,  $\Delta\varepsilon'_p$ , also plays a major role in this damage parameter as well.

$$\Delta\varepsilon'_p = \Delta\varepsilon'_s - \frac{f'_{n+1} - f'_n}{E'_u} \quad (3.62)$$

$$f'_{n+\frac{1}{2}} = \frac{1}{2}(f'_{n+1} + f'_n) \quad (3.63)$$

$$Y_{n+\frac{1}{2}} = \frac{1}{2} \frac{\left(f'_{n+\frac{1}{2}}\right)^2}{E'_o} \quad (3.64)$$

$$\Delta D_m = \left( \frac{Y}{S} \right)^t \Delta \varepsilon'_p \quad \text{if } f'_{n+\frac{1}{2}} > 0 \quad (3.65)$$

where  $t$  and  $D_{crit}$  are material constants and  $S$  is a suggested material constant calculated using equation (3.66).

$$S = \frac{1}{2} \frac{(f_y)^2}{E'_o} \quad (3.66)$$

Thus (3.65) turns into the following expression.

$$\Delta D_m = \left( \frac{f'_{n+\frac{1}{2}}}{f_y} \right)^{2t} \Delta \varepsilon'_p$$

After  $\Delta D_m$  is calculated, it is added to the previous value of  $D$ , and if that value exceeds  $D_{crit}$ , then the material does not develop any more stress for the rest of the analysis.

The material constants,  $t$  and  $D_{crit}$ , were calibrated to the rupture experimental tests performed by Kunnath et al. (2009b). Specifically, it was calibrated to the loading tests of the specimens with the material designated Heat 3 in the experiments. A relationship between  $t$  and  $D_{crit}$  was found for each specimen and the intersection of these curves would yield the constants for the Heat 3 material. Figure 3.11 shows the curves and where most of them intersect ( $t \approx 0.43$  and  $D_{crit} \approx 0.19$ ). Although the lines intersected at several points, the point of intersection with a lower  $D_{crit}$  value was chosen as it would be more conservative to have a constant which leads to less cycles until failure for a given strain history.

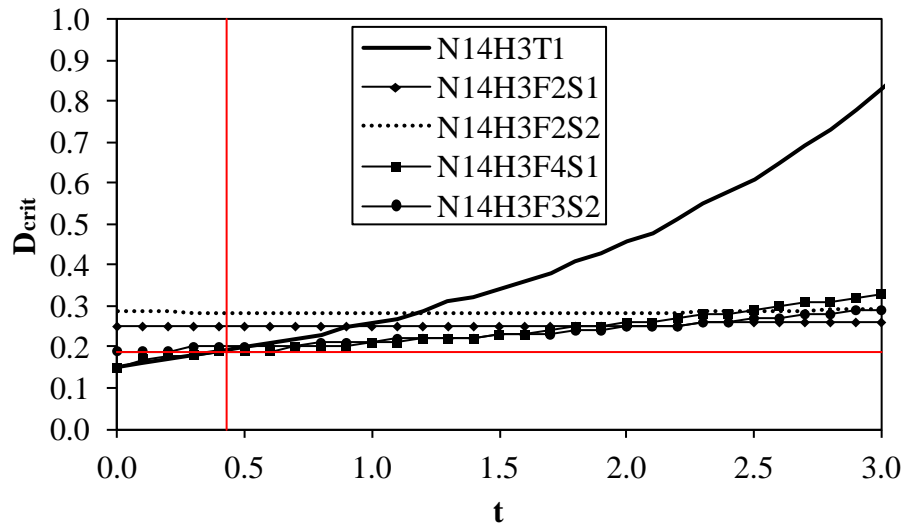


**Figure 3.11.** Relationships Between  $t$  and  $D_{crit}$  that Lead to an Accurate Cycle of Rupture for Test Specimens tested by Kunnath et al. (2009b) with the cross hairs denoting the coordinate used on analysis.



## 4. Verification of the Material Model

### 4.1 Verification of Hysteretic Stress Response Without Buckling

First, the proposed model must be able to capture the stress-strain behavior of the original Dodd and Restrepo model. Two comparisons between the original and modified models are shown in Figures 4.1a and b. Second, the stress-strain law is verified with test experimental data performed by Dodd and Restrepo and Ma et al. The Dodd and Restrepo experiments are chosen because they show both high and low-amplitude cycles and the experimental data were the basis of the original model. The experiment performed by Ma is chosen because it was desirable to see how well the analysis did with a specimen outside of Dodd and Restrepo's experiments. Table 4.1 lists the material properties used in each analysis which is found in Figures 4.2 a-c. The analyses are identified by the name of the experimenters and the test specimens (Restrepo et al., 1994)(Ma et al. 1976).

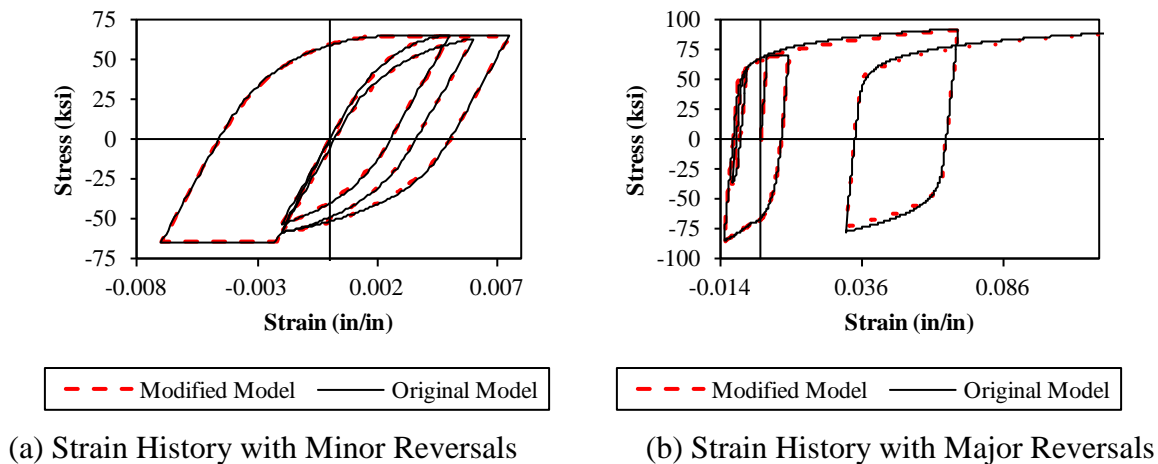
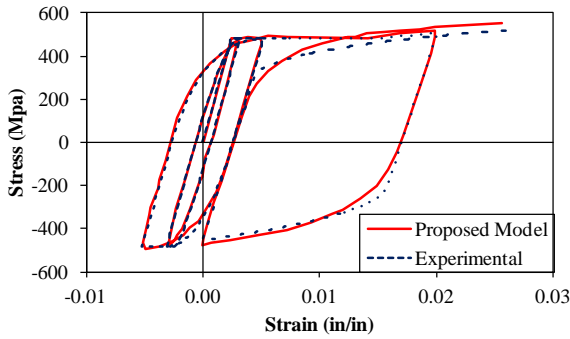


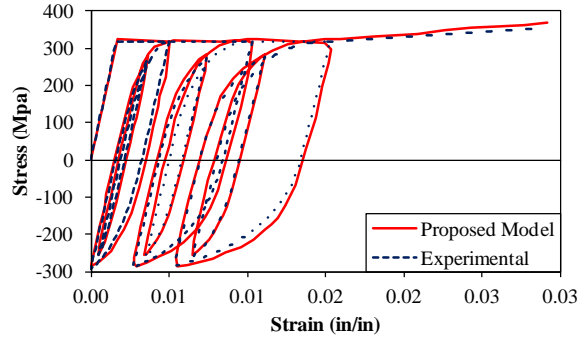
**Figure 4.1.** Comparison Between the Analyses Proposed and Original Dodd and Restrepo Models (2005).

**Table 4.1.** Material Properties for Experiments and Analyses.

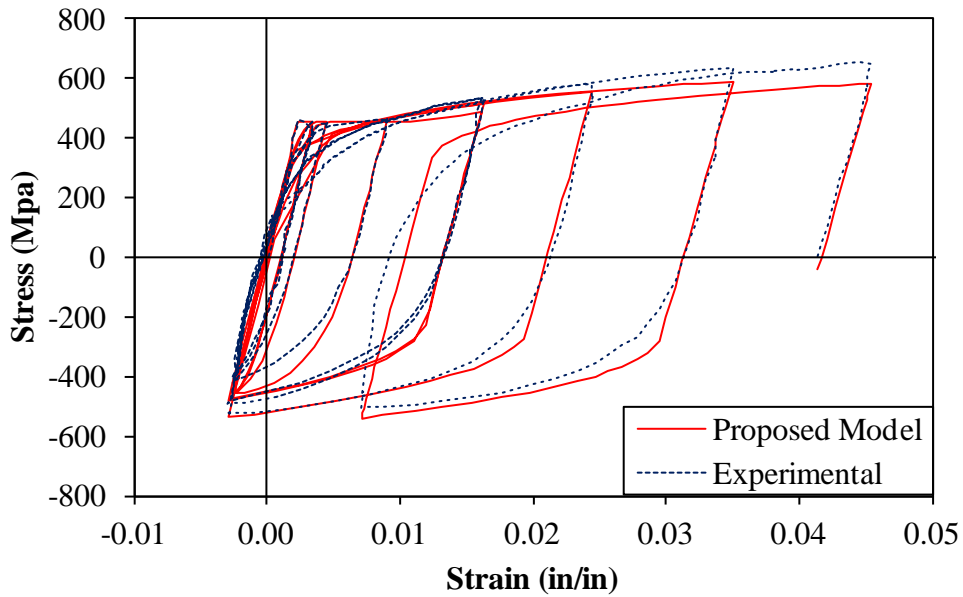
Specimen	$f_v$ (ksi)	$E_s$ (ksi)	$\epsilon_{sh}$	$\epsilon_{sh,1}$	$f_{sh,1}$ (ksi)	$\epsilon_{su}$	$f_{su}$ (ksi)	Ref
HV15	69.91	28863	0.0178	0.05100	85.80	0.146	92.97	Restrepo et al., 1994
MJSG2	46.27	28572	0.0160	0.03930	55.11	0.225	69.04	Restrepo et al., 1994
2	66.00	29000	0.0118	0.02596	80.02	0.123	95.00	Ma et al., 1976



(a) Specimen HV15



(b) Specimen MJSG2



(c) Specimen 2

**Figures 4.2.** Verification of Proposed Stress-Strain Law Calculations with Experimental Results (Restrepo et al., 1994) (Ma et al. 1976).

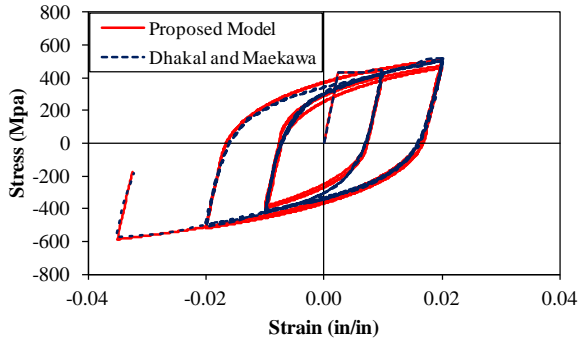
## 4.2 Verification of Buckling Strength Degradation Analysis

The most readily available experimental data for cyclically loaded reinforcing bar with buckling included was collected by Monti and Nuti (1992). The model is compared with this experimental data for verification. As stated before, the original Dodd and Restrepo model, as well as the proposed model, is only calibrated to highly-ductile steel reinforcement used in earthquake-prone regions. The specimens used in Monti and Nuti's experiments (1992) do not share these material properties, it is necessary to find a temporary solution for verification.

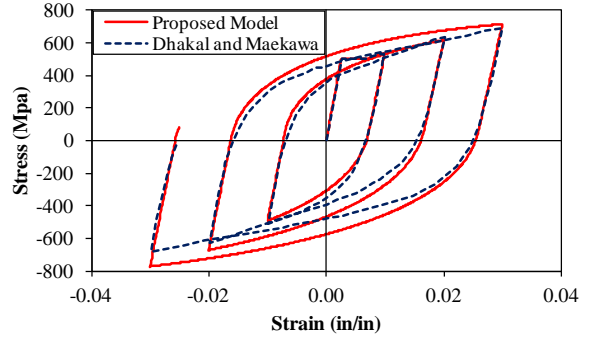
This temporary solution involves applying a factor to the parameter  $\Omega$  which is used to calculate the parameter  $b$  in the NURBS approximation. This parameter is further discussed in detail in Appendix B. Dhakal and Maekawa (2002a) published the results of their model without considerations for buckling. Because the proposed considerations for inelastic buckling are supposed to be able to apply to any material model, these analyses were used. To account for the difference in carbon content, a factor applied to  $\Omega$  in the calculations for the major reversal parameters. This factor is calibrated to Dhakal and Maekawa's analytical results related to the stress response of a reinforcing bar without considerations for buckling. The material properties as well as the factor applied to  $\Omega$  are shown in Table 4.2. As shown in Figures 4.2a and b, the calibration worked well for two of the specimens (Dhakal and Maekawa, 2002a).

**Table 4.2.** Material Properties of Specimens for Cyclic Tests.

Specimen	$f_v$ (ksi)	$E_s$ (ksi)	$\epsilon_{sh}$	$\epsilon_{sh,1}$	$f_{sh,1}$ (ksi)	$\epsilon_{su}$	$f_{su}$ (ksi)	factor
C3	62.37	26107	0.007	0.04	76.14	0.10	85.0	0.4266
S5, S8 and S11	72.52	29008	0.007	0.02	91.37	0.09	107.5	0.6500



(a) Specimen C3



(b) Specimen S5

**Figure 4.3.** Simulated Stress Response Without Buckling According to the Modified Proposed Model and the Model by Dhakal and Maekawa (2002a).

After this was determined, the rest of the analyses were compared as shown in Figures 4.3 a-d. It should be noticed that Specimens S5, S8 and S11 are from the same material and have a slenderness ratio of 5, 8 and 11 respectively. Specimen C3 has different material properties and has a slenderness ratio of 11.

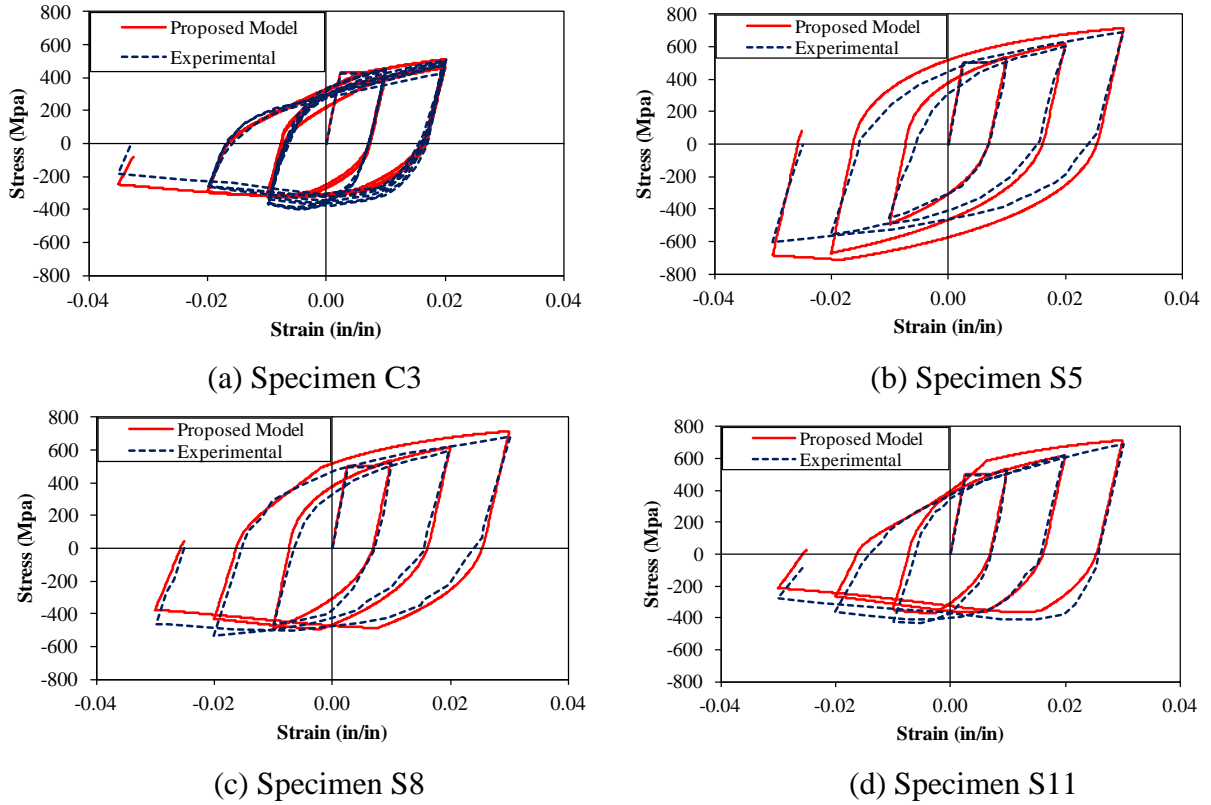


**Figure 4.4.** Analytical and Experimental Cyclic Responses of Test Specimens Examined By Monti and Nuti (1992).

### 4.3 Verification of Low-Cycle Fatigue Law

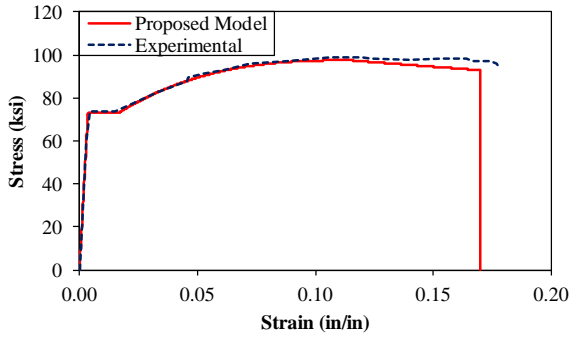
The most comprehensive experimental data on rupture was performed by Kunnath, Kanvinde, Xiao and Zhang. As stated before, the proposed model is only verified for one of the materials experimented on, the properties of which are listed in Table 4.3. Using the material constant values determined earlier, the proposed model is compared with the results of two monotonic tests and two cyclic tests (Figure 4.4) (Kunnath et al., 2009b).

In the monotonic analysis, the strain at rupture is quite accurate for both specimens N14H3T1 and N14H3T2 from experiments performed by Kunnath. For the cyclic analysis, the number of cycles before rupture is recorded. Specimen N14H3F2S1 fails after thirteen cycles in

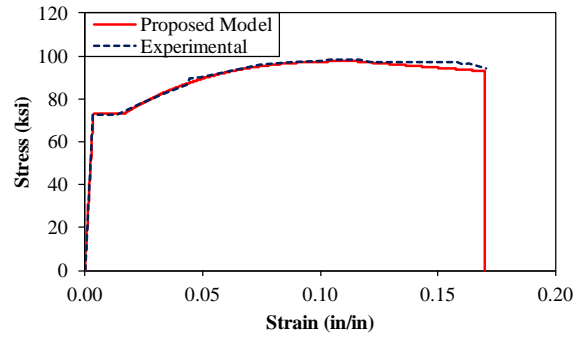
the analysis, while it has failed after seventeen cycles in the experiment. Specimen N14H3F3S1 fails after eight cycles in the analysis while it failed after seven cycles in the experiment (Kunnath et al., 2009b).

**Table 4.3.** Material Properties Used in Experiments and Analysis.

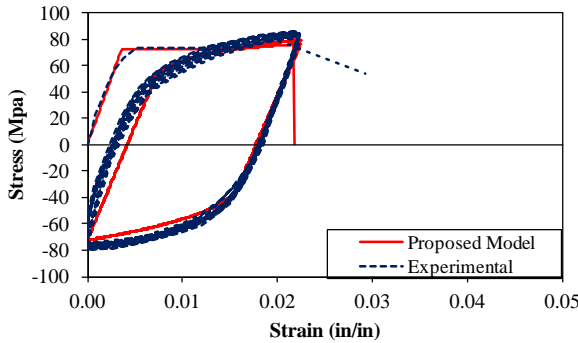
Material	$f_v$ (ksi)	$E_s$ (ksi)	$\epsilon_{sh}$	$\epsilon_{sh,1}$	$f_{sh,1}$ (ksi)	$\epsilon_{su}$	$f_{su}$ (ksi)
Heat 3	73	20278	0.0165	0.04202	86.56	0.11471	97.5



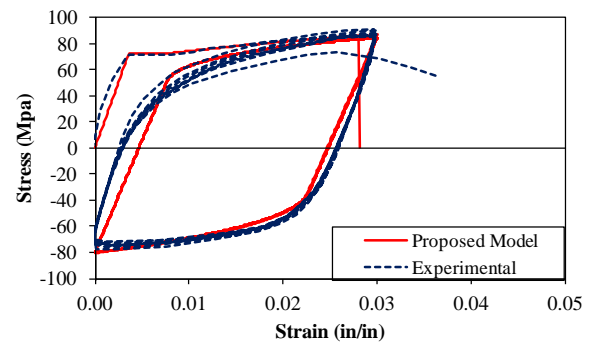
(a) Specimen N14H3T1



(b) Specimen N14H3T2



(c) Specimen N14H3F2S1



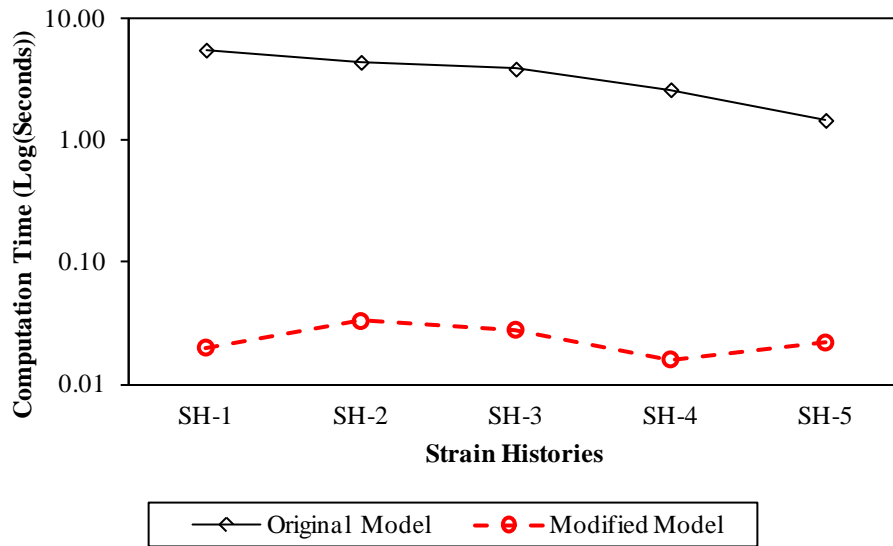
(d) Specimen N14H3F3S1

**Figure 4.5.** Verification of Low Cycle Fatigue Analysis Between Proposed Model and Experimental Results Gathered by Kunnath (2009b).

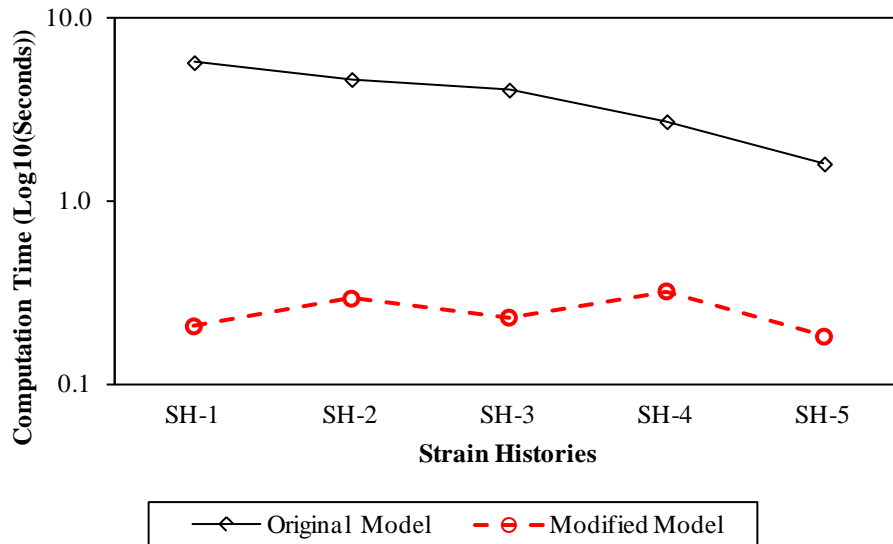
#### 4.4 Computational Time of Analyses

The computation time of these analyses were recorded and compared with that of the original Dodd and Restrepo Material model. Figure 4.6a illustrates the difference in the time it takes to compute the nonlinear reversal curve between the material models. Figure 4.6b

illustrates the difference in the time it takes to complete a complete analysis for each material model. The amount of time it took to simulate the nonlinear reversal curve with the proposed model is so small, that the time data had to put into a logarithmic scale to see the significant difference in computation time.



(a) Logarithm (base 10) of the Computational Time of Nonlinear reversal curve Calculations.



(b) Logarithm (base 10) of the Computational Time of Complete Analyses.

**Figure 4.6.** Computational Time Analysis of the Original and Modified Material Models.

When looking at the time it takes to calculate the stress response in the nonlinear reversal curve alone, and analysis performed by the proposed model requires no more than 1.5% of the time required by the original Dodd and Restrepo model to do the same. When looking at the total time of analysis, the analysis performed by the proposed model requires no more than 12% of the time required by the original model. This is despite the fact that the proposed model also accounts for buckling and low-cycle fatigue, which the original model doesn't (Dodd and Restrepo, 1995).



## **5. Summary and Discussion**

The verifications show a material model which is accurate. The proposed model's predictions show good agreement with the experimental data. Previous research has developed models which showed similar results. The significance of this research is that the material model performed similar, if not better, results with more efficient and robust equations. The amount of computational time saved from these processes will accelerate analyses of reinforced concrete systems. Furthermore, the robustness of the model will help future projects progress without the convergence failures which hinder many analyses.

The validations show that the analysis fits the experimental data of reinforcing bars reasonably well. The analysis is slightly more accurate in minor reversals than for major reversals, but the major reversal responses do not differ significantly between the analyses done by the original Dodd and Restrepo material model and the proposed model as shown in Figure 4.1. Also, it is rare that the stress in reinforcing bars ever reaches strains beyond the onset of strain hardening in any given analyses. Therefore, most of the time will be spent on the more accurate minor reversals.

The verification of the buckling considerations show favorable agreement as well with the experimental data of buckled reinforcing bars for slenderness ratios of greater than 5. It should be noted that the lower the slenderness ratio the more delayed the onset of buckling. This is consistent with experimental results by Monti and Nuti (1992) and Bayrak and Sheikh (2001). Finally, the tensile response after buckling is fairly accurate, but relatively crude in appearance compared to that of other methods. The proposed method produces a tensile curve with sudden changes in curvature and a nearly linear response in between. There may be a need to create a

more gradual curve in the tensile region, but the current results are fairly close to the experimental results.

The verifications of the proposed model with the experimental tests on rupture are also promising. In one of the cyclic analyses the number of cycles to failure is less than those recorded in the experiment, but the other cyclic analysis and the monotonic analyses showed a good agreement with the experimental results regarding the cycle and strain at rupture. However, there is still a difference in one of the cyclic analyses and one of the monotonic analyses was more accurate than the other. This might indicate that the proposed method of rupture is fairly sensitive to differences in material properties. It should also be noted that the analyses were done with nearly the same set of “averaged” material properties. The values for  $t$  and  $D_{crit}$  used in the verifications are specific to A706 No.14 reinforcing bars with the material properties listed in Table 4.3.

A significant conclusion is that the proposed model required significantly less computation time to perform more analyses than the original Dodd and Restrepo model. The proposed model requires slightly more memory than the original and more time to account for inelastic buckling and low-cycle fatigue, but it makes up for the time when calculating the stress response in the nonlinear reversal curve. Figures 4.6b show that even with considerations for buckling and low-cycle fatigue, the proposed model still showed a significant improvement in efficiency over its predecessor, which provided considerations for neither.

An even more significant conclusion is a material model that is more mathematically robust while also accurate. The direct calculations in the stress strain law, as well as the separation of the buckling and low-cycle fatigue considerations remove the chance of numerical convergence failure as is common in the previous methods. Even the original Dodd and Restrepo

model had chances of numerical convergence failure. Many of the analyses done to create Figures 4.6a and b were not completed because the original model could not reach convergence for certain strain histories and material properties. However, the proposed model has always reached convergence through their simple and direct equations, which is a significant improvement on existing material models. The efficiency and robustness would help complex inelastic analyses of reinforced concrete structures in earthquake-prone areas.

## 6. Need for Further Research

The proposed model still cannot accurately simulate the response of reinforcing bars with a carbon content significantly different from that of the experimental specimens tested on by Restrepo et al. (1994). As stated before, this isn't a problem with A706 reinforcing bars and other models have been calibrated to materials of specific chemical contents as well. Still, the stress response in reinforcing bars older structural systems that primarily used A615 reinforcing bars might be slightly more difficult to simulate as the carbon content is much more variable in that standard. For this purpose, this issue should still be addressed.

Carbon content influences the material properties which are all accounted for in the calculation of the parameter,  $b$ , detailed in Appendix B. However,  $b$  was calibrated to the original Dodd and Restrepo model. If this parameter was calibrated to experimental results of varying chemical properties using the same calibration process, it could resolve this issue well. Furthermore, the factor applied to  $\Omega$  was sufficient for the buckling analyses. If a relationship was derived between the factor and the carbon content, then the proposed model could also be applied to reinforcing bar other than A706.

Another minor issue is that the proposed model doesn't ensure that the sign of curvature is retained in compressive reversal curves. This is due to the fact that wherever the true stress-strain relationship is linear, the curvature in engineering coordinates is slightly negative. So the sign of curvature is retained in the tensile reversal curves but not in the compressive. However, as shown in Appendix D, this was a problem in the original Dodd and Restrepo model, and the curvature can be deemed negligible in these regions. Still, this is an issue that is worth looking over in future studies. It is out of the scope of this study to solve inherent problems in the original Dodd and Restrepo material model not related to the iterative calculations.

Finally, the considerations for low-cycle fatigue require refinement. While the analysis showed good results with the  $t$  and  $D_{crit}$  values, these values are limited to the test specimens used in the calibrations. It will be useful to provide a physically meaningful approach to calculating the values for  $t$  and  $D_{crit}$ . This way, the low-cycle fatigue considerations won't rely too heavily on empiricism and will be applicable to more materials. But for this to happen, more experimental data on the rupture in reinforcing steel of various material properties must be performed and analyzed.

## References

- Aktan, A.E., Karlsson, B.I., and Sozen, M.A. (1973). "Stress-Strain Relationships of Reinforcement Bars Subjected to Large Strain Reversals." *Report No. NSFRC GI 29934*, Dept. of Civ. Engrg., University of Illinois, Urbana, ILL.
- ASTM A615 / A615M - 14, 1976 (2013), "Standard Specification for Deformed and Plain Carbon-Steel Bars for Concrete Reinforcement," ASTM International, West Conshohocken, PA, 2014, DOI: 10.1520/A0615\_A0615M, [www.astm.org](http://www.astm.org).
- ASTM A706 / A706M, 2000 (2013), "Standard Specification for Deformed and Plain Low-Alloy Steel Bars for Concrete Reinforcement," ASTM International, West Conshohocken, PA, 2014, DOI: 10.1520/A0706\_A0706M, [www.astm.org](http://www.astm.org).
- ASTM Standard E1049-85, 1997 (2011), "Standard Practices for Cycle Counting in Fatigue Analysis," ASTM International, West Conshohocken, PA, 2014, DOI: 10.1520/E1049-85R11E01, [www.astm.org](http://www.astm.org).
- Bae, S., Miseses, A.M., and Bayrak, O. (2005). "Inelastic Buckling of Reinforcing Bars." *Journal of Structural Engineering* 131(2), 314-321.
- Balan, T.A., Filippou, F.C., and Popov, E.P. (1998). "Hysteretic Model of Ordinary and High Strength Reinforcing Steel." *Journal of Structural Engineering* 124(3), 288-297.
- Bayrak, O., Sheikh, S.A. (2001). "Plastic Hinge Analysis." *Journal of Structural Engineering* 127(9), 1092-1100.

- Chang, G.A. and Mander, J.B. (1994). "Seismic Energy Based Fatigue Damage Analysis of Bridge Columns: Part I – Evaluation of Seismic Capacity." *Rep. NCEER-94-0006*, National Center for Earthquake Engineering Research, State University of New York at Buffalo, Buffalo, NY.
- Chen, W.E. and Lui, E.M. (1936), *Structural Stability: Theory and Implementation*, Elsevier Science Publishing Co., Inc, New York, 100pp.
- Cooper, J.D., Fiedland, I.M., Buckle, I.G., Nimis, R.B., and Bobb, N.M. (1994). "The NorthRidge Earthquake." From U.S. Department of Transportation: Federal Highway Administration.  
<https://www.fhwa.dot.gov/publications/publicroads/94summer/p94su26.cfm>
- Cosenza, E., Cicco, F., Prota, A. (2009). "Discussion of "Nonlinear Nonlinear Uniaxial Model For Reinforcing Steel Bars" by Sashi K. Kunnath, YeongAe Heo, and Jon F. Mohle." *Journal of Structural Engineering* 135(4), 917-920.
- Dhakal, R.P., and Maekawa, K. (2002a). "Path-Dependent Cyclic Stress-Strain Relationship of Reinforcing Bars Including Buckling." *Engineering Structures* 24(11), 1383-1396.
- Dhakal, R.P., and Maekawa, K. (2002b). "Model For Postyield Buckling of Reinforcement." *Journal of Structural Engineering* 128(9), 1139-1147.
- Dodd, L.L., and Restrepo-Posada, J.I. (1995). "Model For Predicting Cyclic Behavior of Reinforcing Steel." *Journal of Structural Engineering* 121(3), 433-445.
- Downing, S.D. and Socie, D.F. (1982). "Simple Rainflow Counting Algorithms." *International Journal of Fatigue* 4(1), 31-40.

- Filippou, F.C., Popov, E.P., and Bertero, V.V. (1983). "Effects of Bond Deterioration on Hysteretic Behavior of Reinforced Concrete Joints." *EERC Rep. 83-19*, Earthquake Engrg. Res. Ctr., University of California, Berkeley, Calif.
- Gomes, A. and Appleton, J. (1997). "Nonlinear Cyclic Stress-Strain Relationship of Reinforcement Bars Including Buckling." *Engineering Structures* 19(10), 822-826.
- Hoehler, M.S., and Stanton, J.F., (2006). "Simple Phenomenological Model for Reinforcing Steel under Arbitrary Load." *Journal of Structural Engineering* 132(7), 1061-1069.
- Huang, Y., and Mahin, S.A. (2010). "Simulating the Inelastic Seismic Behavior of Steel Braced Frames Including the Effects of Low-Cycle Fatigue." *PEER Rep. 2010/104* Pacific Earthquake Engineering Center, University of California, Berkeley, Calif.
- Kent, D.C., and Park, R. (1973). "Cyclic Load Behaviour of Reinforcing Steel." *Strain* 9(3), 98-103.
- Kunnath, S.K., Heo, Y., and Mohle, J.F. (2009a). "Nonlinear Uniaxial Model For Reinforcing Steel Bars." *Journal of Structural Engineering* 135(4), 335-343.
- Kunnath, S.K., Kanvinde, A., Xiao, Y., Guowei, Zhang. (2009b). "Effects of Buckling and Low-Cycle Fatigue on Seismic Performance of Reinforcing Bars and Mechanical Couplers for Critical Structural Members." *Report No. CA/UCD-SESM-08-01*, Davis, CA.
- Ma, S. –Y. M., Betero, V. V., and Popov, E. P. (1976). "Experimental and Analytical Studies on The Hysteretic Behavior of Reinforced Concrete Rectangular and T-Beams." *EERC Rep. 76-02*, Earthquake Engrg. Res. Ctr., University of California, Berkeley, Calif.
- Massone, L.M., and Moroder, D. (2008). "Buckling Modeling Of Reinforcing Bars With Imperfections." *Engineering Structures* 31, 758-767.



- Mendes, L.A.M., and Castro, L.M.S.S. (2014) “A Simplified Reinforcing Steel Model Suitable for Cyclic Loading Including Ultra-Low-Cycle Fatigue Effects.” *Engineering Structures* 68, 155-164.
- Monti, G., and Nuti, C. (1992). “Nonlinear Cyclic Behavior of Reinforcing Bars Including Buckling.” *Journal of Structural Engineering* 118(12), 3268-3284.
- Piegl, L and Tiller, W. (1997). *The NURBS Book*, 2<sup>nd</sup> Ed., Springer-Verlag, New York.
- N.A. (2012). “China Earthquake Reconnaissance Report: Performance of Transportation Structures During the May 12, 2008, M7.9 Wenchuan Earthquake.”  
From U.S. Department of Transportation: Federal Highway Administration –  
Office of Research, Development, and Technology, Office of Infrastructure.  
<http://www.fhwa.dot.gov/publications/research/infrastructure/structures/11029/003.cfm>
- Restrepo-Posada, J.I., Dodd, L.L., Park, R., and Cooke, N. (1994). “Variables Affecting Cyclic Behavior of Reinforcing Steel.” *Journal of Structural Engineering* 120(11), 3178-3196.
- Rodriguez, M.E., Botero, J.C., and Villa, J. (1999). “Cyclic Stress-Strain Behavior of Reinforcing Steel Including Effect of Buckling.” *Journal of Structural Engineering* 125(6), 605-612.
- Urmson, C.R., and Mander, J.B. (2012). “Local Buckling Analysis of Longitudinal Reinforcing Bars.” *Journal of Structural Engineering* 138(1), 62-71.
- Weisstein, Eric W. "Cylindrical Wedge." From [MathWorld](http://mathworld.wolfram.com/CylindricalWedge.html)--A Wolfram Web Resource.  
<http://mathworld.wolfram.com/CylindricalWedge.html>
- Wilson, D.V. and Bate, P.S. (1986). “Reversibility in the Work Hardening of Spheroidised Steels.” *Acta Metallurgica*, 34(6), 1107-1120.

## **Appendix A: Derivation of Basis Functions in NURBS-Based Interpolations**

### **A.1 Introduction**

The Non-Uniform Rational B-Spline approximation (NURBS) is the basis for many of the equations used in the proposed model. The algorithm for the approximation is used in many computer drawing programs such as AutoCAD. The algorithm is a direct calculation involving parametric equations to define coordinates on the curve. Since it doesn't need iterations, it was chosen for the proposed model to increase efficiency. A second degree NURBS curve consists of three basis functions and a control polygon with three vertices (control points). The basis functions combined with the control points form the parametric equations with  $u$  as their independent variable. The derivation of the basis functions is detailed below (Piegl and Tiller, 1997).

### **A.2 B-Spline Basis Functions**

The derivation starts with a knot vector, which defines the value of  $u$  where the B-Spline curve runs tangent to the control polygon. In every case the approximation is used, the curve only runs tangent at the beginning ( $u = 0$ ) and end ( $u = 1$ ) of the control polygon. Therefore the knot vector is  $\{0,0,0,1,1,1\}$ . The values are zero and one because those are the only values of  $u$  when the curve runs tangent. These values are also repeated to derive second degree basis functions. The computation for the basis functions depend on equations.

$$N_{i,0}(u) = \begin{cases} 1 & \text{if } u_i \leq u \leq u_{i+1} \\ 0 & \text{otherwise} \end{cases} \quad (\text{A.1})$$

$$N_{i,p}(u) = \frac{u - u_i}{u_{i+p} - u_i} N_{i,p-1}(u) + \frac{u_{i+p+1} - u}{u_{i+p+1} - u_{i+1}} N_{i+1,p-1}(u) \quad (\text{A.2})$$

where  $i$  identifies the unique basis function,  $u_i$  refers to a knot element and  $p$  denotes the degree of the basis function. It should be noted that  $i$  starts at 0 instead of 1, meaning that  $u_0$  refers to the first element of the knot vector (Piegl and Tiller, 1997).

Because the calculation of the basis functions of any degree,  $p$ , are based off of the basis functions calculated for a degree,  $p-1$ , a truncated triangular table is formed showing the order of which each basis function is calculated.

$$\begin{array}{cccc}
 0 & & & \\
 0 & N_{0,0} & & \\
 0 & N_{1,0} & N_{0,1} & N_{0,2} \\
 0 & N_{2,0} & N_{1,1} & N_{1,2} \\
 1 & N_{3,0} & N_{2,1} & N_{2,2} \\
 1 & N_{4,0} & N_{3,1} & \\
 1 & & & 
 \end{array}$$

The first column is the transposed knot vector. Using (A.1), it is determined that the basis functions  $N_{0,0}$ ,  $N_{1,0}$ ,  $N_{3,0}$  and  $N_{4,0}$  are equal to 0. Because the basis function,  $N_{2,0}$ , is the only one bound by different knot values, (A.1) is used to define the basis function (Piegl and Tiller, 1997).

$$N_{2,0}(u) = \begin{cases} 1 & \text{if } 0 \leq u \leq 1 \\ 0 & \text{otherwise} \end{cases}$$

The knot vector elements only range from zero to one, meaning that the value of  $u$  never falls out of the range  $[0,1]$  for the length of the curve. Therefore,  $N_{2,0}(u) = 1$ .

The basis functions of higher orders are calculated using equation (A.2) as shown below.

$$N_{0,1}(u) = \frac{u - u_0}{u_1 - u_0} N_{0,0}(u) + \frac{u_2 - u}{u_2 - u_1} N_{1,0}(u) = 0$$

$$N_{1,1}(u) = \frac{u - u_1}{u_2 - u_1} N_{1,0}(u) + \frac{u_3 - u}{u_3 - u_2} N_{2,0}(u) = 1 - u$$

$$N_{2,1}(u) = \frac{u - u_2}{u_3 - u_2} N_{2,0}(u) + \frac{u_4 - u}{u_4 - u_3} N_{3,0}(u) = u$$

$$N_{3,1}(u) = \frac{u - u_3}{u_4 - u_3} N_{3,0}(u) + \frac{u_5 - u}{u_5 - u_4} N_{4,0}(u) = 0$$

These basis functions are then used to calculate the second order basis functions.

$$N_{0,2}(u) = \frac{u - u_0}{u_2 - u_0} N_{0,1}(u) + \frac{u_3 - u}{u_3 - u_2} N_{1,1}(u) = (1 - u)^2$$

$$N_{1,2}(u) = \frac{u - u_1}{u_3 - u_1} N_{1,1}(u) + \frac{u_4 - u}{u_4 - u_2} N_{2,1}(u) = 2u(1 - u)$$

$$N_{2,2}(u) = \frac{u - u_2}{u_4 - u_2} N_{2,1}(u) + \frac{u_5 - u}{u_5 - u_3} N_{3,1}(u) = u^2$$

These are the basis functions used for every NURBS approximation in the proposed model. Two variations are shown below.

$$C(u) = (1 - u)^2 P_0 + 2u(1 - u)P_1 + u^2 P_2 \tag{A.3}$$

$$C(u) = \frac{(1 - u)^2 w_0 P_0 + 2u(1 - u)w_1 P_1 + u^2 w_2 P_2}{(1 - u)^2 w_0 + 2u(1 - u)w_1 + u^2 w_2} \tag{A.4}$$

where  $P_0$ ,  $P_1$  and  $P_2$  are the three control points and  $w_0$ ,  $w_1$  and  $w_2$  are the weights applied to the control points.  $C$  also refers to any coordinate, meaning that the basis functions and weights apply to both coordinates while the control points do not. For example, when calculating the stress, the stress coordinates of the control polygon are used (Piegl and Tiller, 1997).

## **Appendix B: Calibration and Calculation of Linear Portion of Major Reversals**

### **B.1 Introduction**

Major reversals differ from minor reversals in that the first control point of the NURBS approximation is delayed to another point along the initial asymptote. Until the first control point in the NURBS curve, the normalized stress and strain relationship is linear. The placement of this first control point is dependent on a variable  $b$ , which will vary with a term,  $\Omega$ . The term  $\Omega$  is designed to uniquely identify any major reversal curve of any material by Dodd and Restrepo in their original material model (B.1) (Dodd and Restrepo, 1995).

$$\Omega = \left[ 0.001 + \frac{0.00108}{1.043 - (\varepsilon'_p / \varepsilon'_{su})} \right] \left( \frac{f'_p}{f'_t} - 0.69 \right) \frac{1}{0.18} + 0.85 \quad (\text{B.1})$$

where

$$\frac{f'_p}{f'_t} = \frac{f'_{su} [s - \varepsilon'_{su,shift}(k) + \varepsilon'_a(m)] - f'_a(m)}{f'_{su} [2 - \varepsilon'_{su,shift}(1) + \varepsilon'_{su,shift}(2)]} \quad (\text{B.2})$$

$$\varepsilon'_p = \left| \varepsilon'_{su,shift}(k) - \varepsilon'_a(m) \right| \quad (\text{B.3})$$

However, this term was formulated specifically for their own normalized coordinate space, which involves a coordinate transformation calculation very different from that in the proposed method. Still, this term is valuable and was used to calculate  $b$ . The relationship between  $b$  and  $\Omega$  were changed based on material properties to account to be suitable for the new coordinate transformation in the proposed model.

## B.2 Calibration of $b$

The parameter  $b$  is calibrated by examining a curve at a reversal from various points along the strain hardening curve until ultimate strain. For each of these reversals, all numbers with 4 decimal places from 0 and 1 are inputted as  $b$  until the stress at a varying strain is equal for both the original Dodd and Restrepo model and the proposed model. The strain at which the stresses from both models are compared varies in an attempt to have equal stresses after the point of highest curvature in the reversal curve. This was found using (B.4):

$$\varepsilon_{sc} = \left( e^{\varepsilon_r^a} - 1 \right) - \left( 0.005 + 10(\varepsilon_{su} - \varepsilon_{sh}) \right) - 10(\varepsilon_r - \varepsilon_{su}) \quad (\text{B.4})$$

where  $\varepsilon_r$  is the strain at reversal and  $\varepsilon_{sc}$  is the strain at which the proposed model is calibrated to the original model.

This process is used to find the relationship between the optimum value of  $b$  and  $\Omega$ . As expected, this relationship varies depending on the material properties as shown in Figure B1 with the material properties listed in Table B1.

**Table B1.** Material Properties of Initial  $b$  Optimization Analysis

Material	$f_v$ (ksi)	$E_s$ (ksi)	$\varepsilon_{sh}$	$\varepsilon_{sh,1}$	$f_{sh,1}$ (ksi)	$\varepsilon_{su}$	$f_{su}$ (ksi)
MAT1	69.91	28863	0.0178	0.05100	85.80	0.146	92.97
MAT2	64.83	28427	0.0170	0.05100	80.10	0.158	87.75
MAT3	46.27	28572	0.0220	0.03930	55.11	0.225	69.04
MAT4	70.00	29000	0.0110	0.01715	78.96	0.290	100.00
MAT5	66.00	29000	0.0140	0.02004	77.51	0.123	95.00
MAT6	45.00	29000	0.0155	0.01965	48.45	0.140	50.00

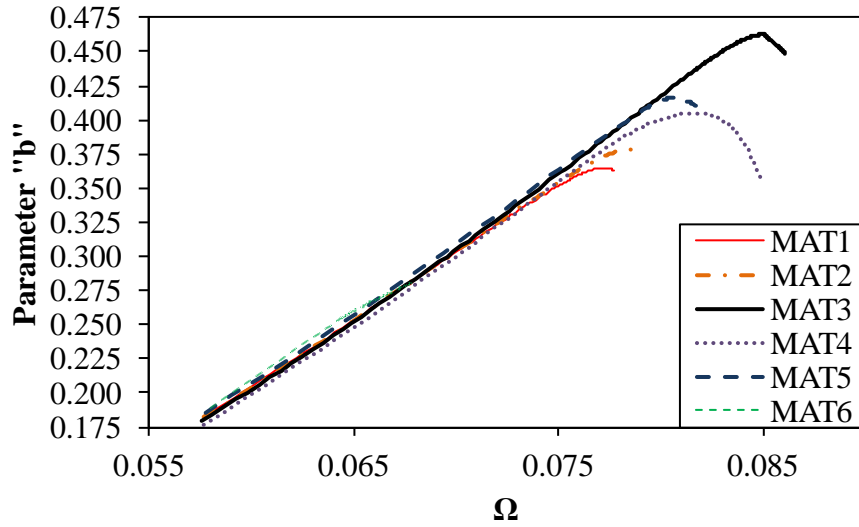


**Figure B1.** Initial  $b$  Optimization Analysis.

Two conclusions are drawn from this initial analysis: The initial slope is constant among all material types and the initial value of  $\Omega$  when  $b$  is zero is constant. These values were found by averaging the values which were obtained by finding a linear fit as shown in Figure B2. The constants are listed in the next section.

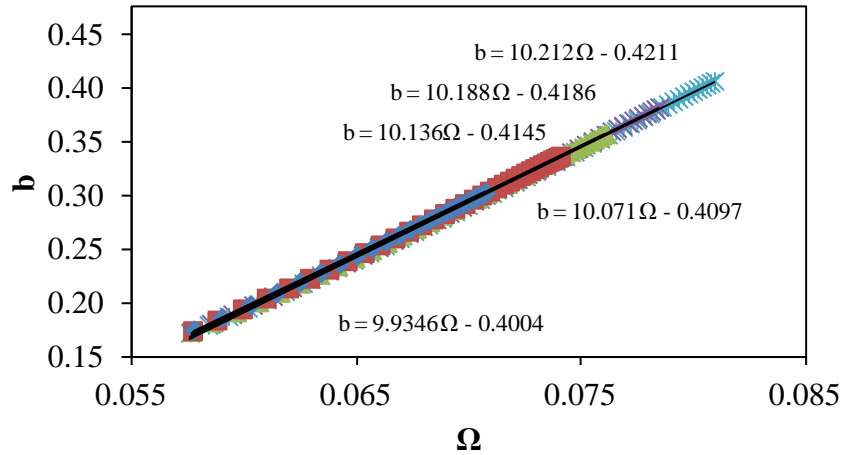


**Figure B2.** First linear portions of  $b$  vs.  $\Omega$ .

It is assumed that the curve ends with a linear relationship with a varying slope and varying value of  $\Omega$  when  $b$  is zero again. Figure B3 shows the assumed relationship between  $b$  and  $\Omega$  which consists of two linear portions and a NURBS curve in the middle.

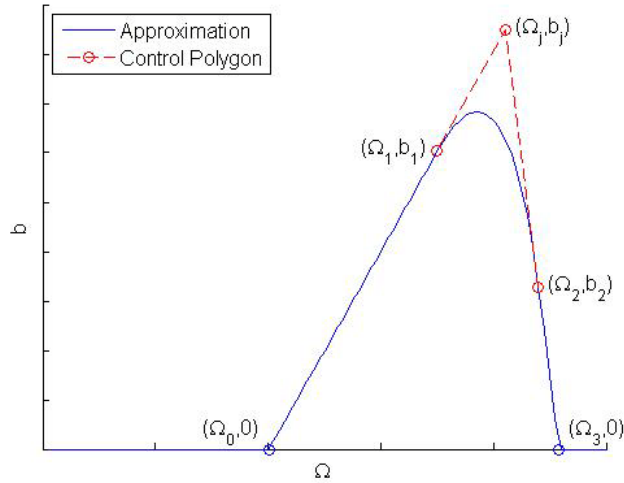
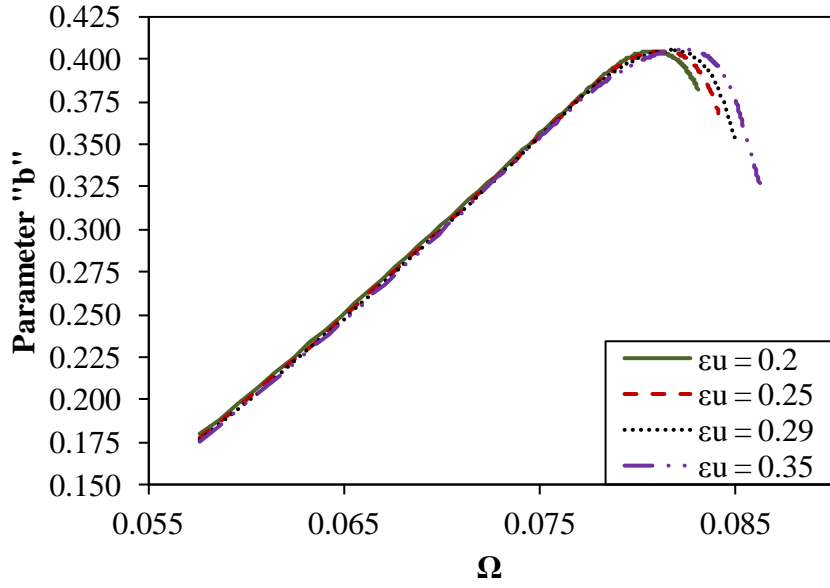


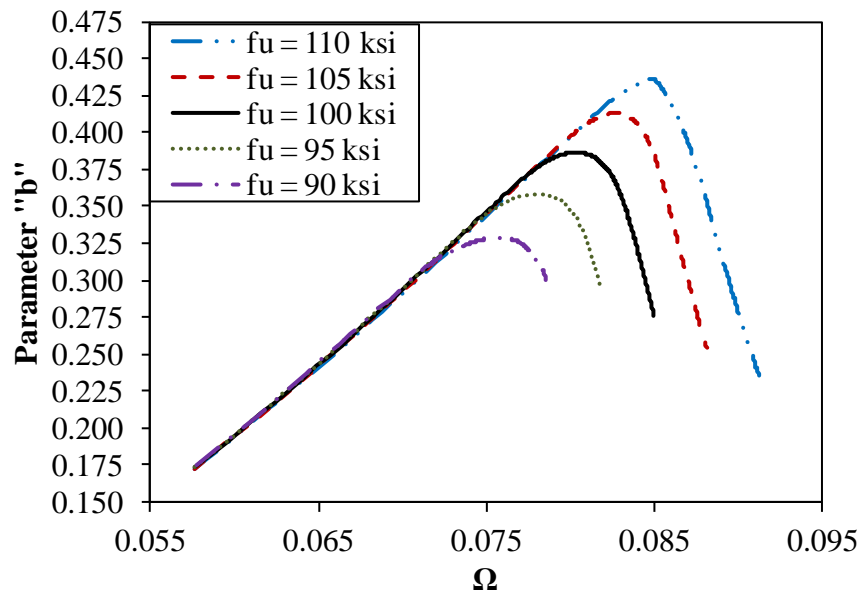
**Figure B3.** General Form of the Variation of  $b$  with  $\Omega$ .

MAT3 is used as a basis point as the different material properties were changed to see how the curve changes. The results from varying several material properties are shown in Figures B4a-d.

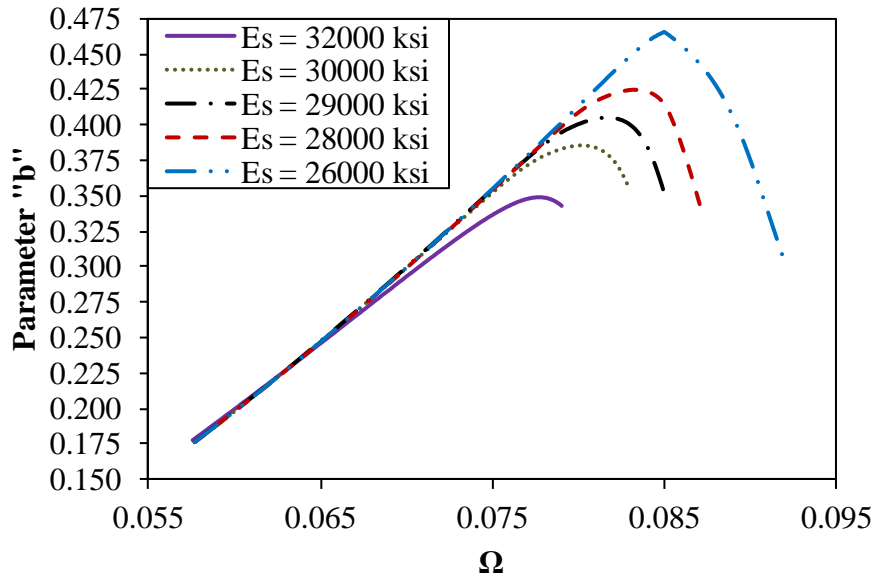




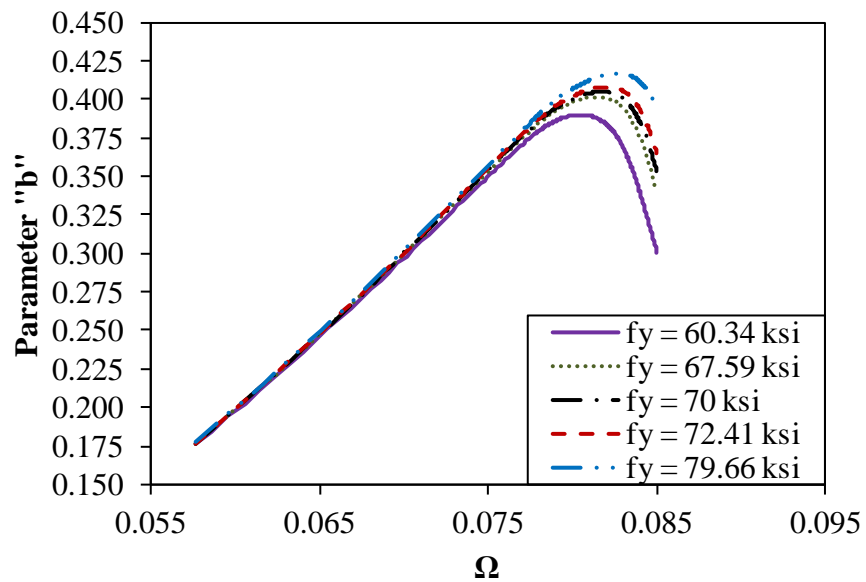
(a) Varying the Ultimate Strain.



(b) Varying the Ultimate Strength.



(c) Varying the Modulus of Elasticity with Constant Yield Strength.



(d) Varying the Yield Strength with Constant Yield Strain.

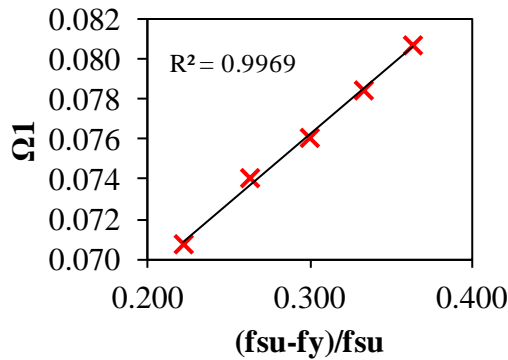
**Figure B4.** Effects of Varying Material Properties on the  $b$  vs.  $\Omega$  Relationship.

The following conclusions are made:

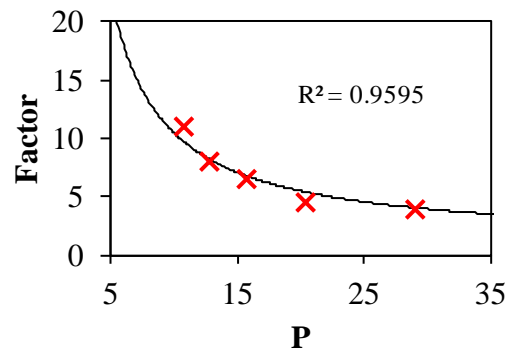
- The ultimate strain doesn't affect the relationship significantly.
- The ultimate strength affects the value of  $\Omega_1$  and  $\Omega_3$ .

- The yield strength affects the relationship less than the yield strain, which seems to be the only thing affecting the slope of the final line,  $m_d$ .

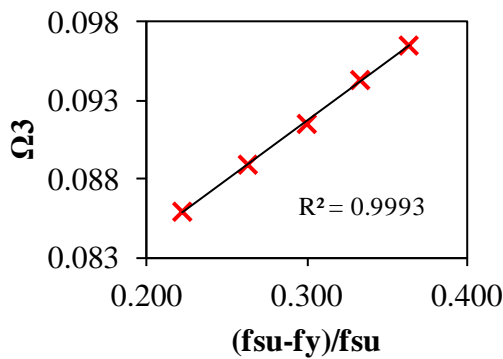
The conclusions from these analyses helped to create relationships between the properties of the  $b$  vs.  $\Omega$  relationship. In order to create relationships between unitless variables, the material properties were represented with the following variables:  $\frac{f_{su} - f_y}{f_{su}}$ ,  $\varepsilon_y$  and  $P$  (the power of the strain hardening curve). After many attempts to find a relationship between the ultimate strain and the variables of the  $b$  vs.  $\Omega$  relationship, it was concluded that the power was the only left variable unaccounted for. These relationships are illustrated in Figures B5a-e. Included in these figures are the constant values of the first slope and  $\Omega_0$ .



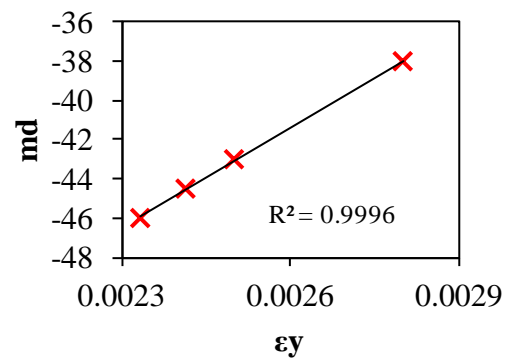
(a) Linear Fit for  $\Omega_1$



(b) Logarithmic fit for Factor in  $\Omega_2$



(c) Linear Fit for  $\Omega_3$



(d) Linear Fit for  $\varepsilon_y$

**Figure B5.** Determination of  $b$  vs.  $\Omega$  relationship constants.

The equations for these constants are listed in the next section. The factor that Figure B5d is referring to is regarding the denominator portion of equation (B.17) in the next section.

### B.3 Calculation of b

The equation for b is a piecewise equation described in equations (B.5) to (B.9).

$$b = 0 \quad \text{if } \Omega \leq \Omega_0 = 0.040137 \text{ or } \Omega \geq \Omega_3 \quad (\text{B.5})$$

$$b = 10.1(\Omega - \Omega_0) \quad \text{if } \Omega_0 < \Omega \leq \Omega_1 \quad (\text{B.6})$$

$$b = (1-u)^2 b_1 + 2u(1-u)b_j + u^2 b_2 \quad \text{if } \Omega_1 < \Omega \leq \Omega_2 \quad (\text{B.7})$$

where

$$u(\Omega) = \frac{-\left(2(\Omega_j - \Omega_1)\right) + \sqrt{\left(2(\Omega_j - \Omega_1)\right)^2 - 4(\Omega_2 - 2\Omega_j + \Omega_1)(\Omega_1 - \Omega)}}{2(\Omega_2 - 2\Omega_j + \Omega_1)} \quad (\text{B.8})$$

$$b = m_d (\Omega - \Omega_3) \quad \text{if } \Omega_2 < \Omega < \Omega_3 \quad (\text{B.9})$$

The variables used in (B.5) to (B.9) are calculated using (B.10) to (B.16).

$$\Omega_1 = 0.069 \frac{f_{su} - f_y}{f_{su}} + 0.0555 \quad (\text{B.10})$$

$$\Omega_3 = 0.0753 \frac{f_{su} - f_y}{f_{su}} + 0.0691 \quad (\text{B.11})$$

$$m_d = 17034 \varepsilon_y - 85.66 \quad (\text{B.12})$$

$$b_j = 10.1(\Omega_j - \Omega_0) \quad (\text{B.13})$$

$$\Omega_j = \frac{10.1\Omega_0 - \Omega_3 m_d}{10.1 - m_d} \quad (\text{B.14})$$

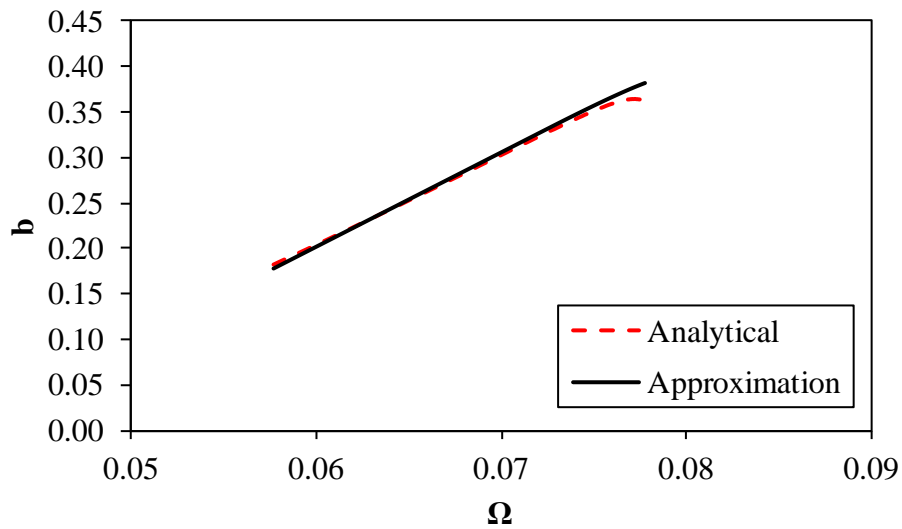
$$b_2 = m_d (\Omega_2 - \Omega_3) \quad (\text{B.15})$$

$$\Omega_2 = \frac{(\Omega_3 - \Omega_j)}{\left(\frac{85}{P-1} + 1\right)} \left(\frac{\Omega_1}{\Omega_j}\right) + \Omega_j \quad (\text{B.16})$$

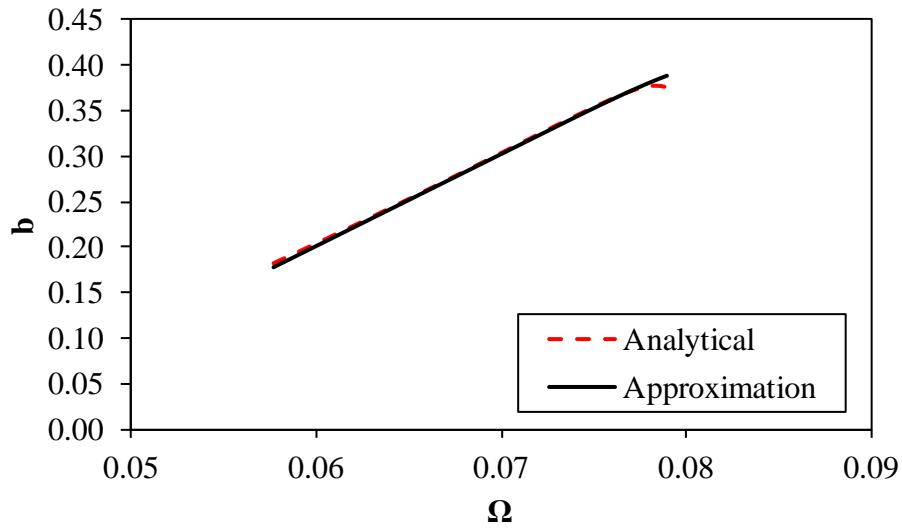
These were determined through various calibrations with varying values of yield stress and strain, ultimate stress, and power of the strain hardening curve.

#### B.4 Verification

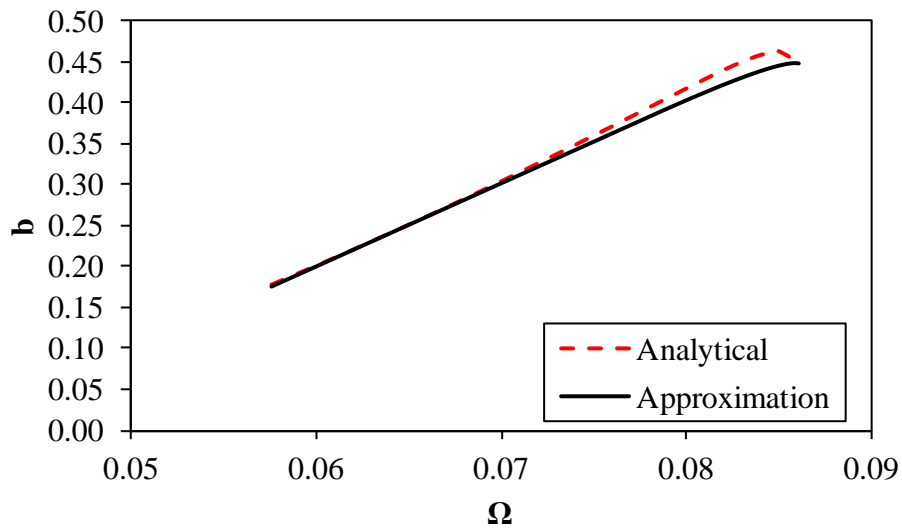
This approximation was verified with all of the material property inputs as specified in Table B1 to verify the accuracy of this approximation. As shown in Figures B6a-f, there is fairly good agreement between the approximations and the initial analytical values shown in Figure B1.



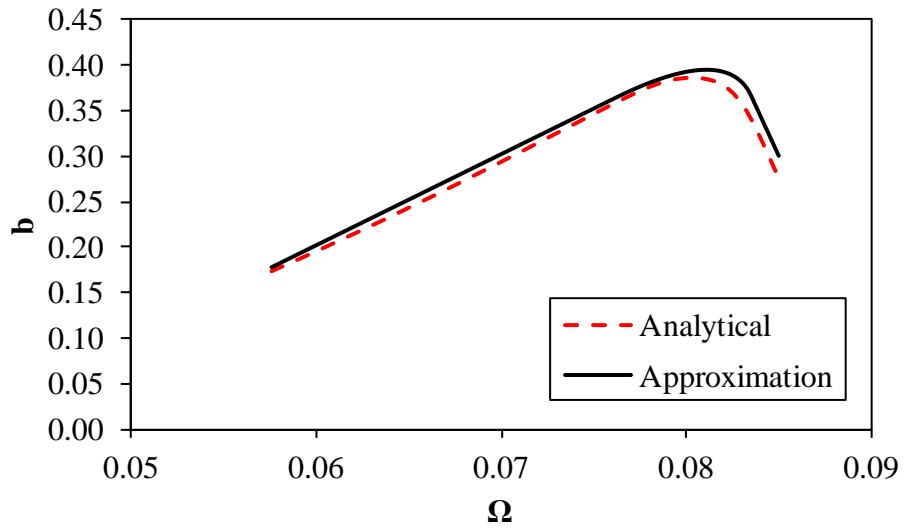
(a) MAT1



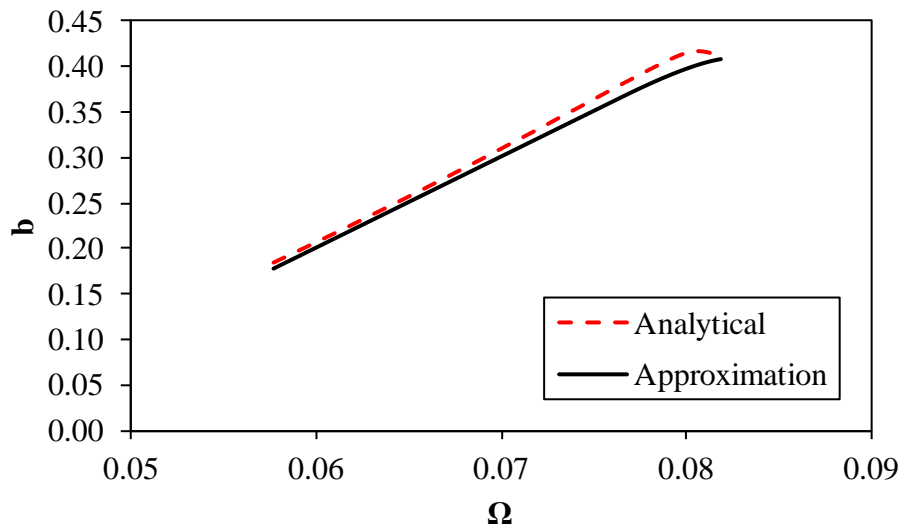
(b) MAT2



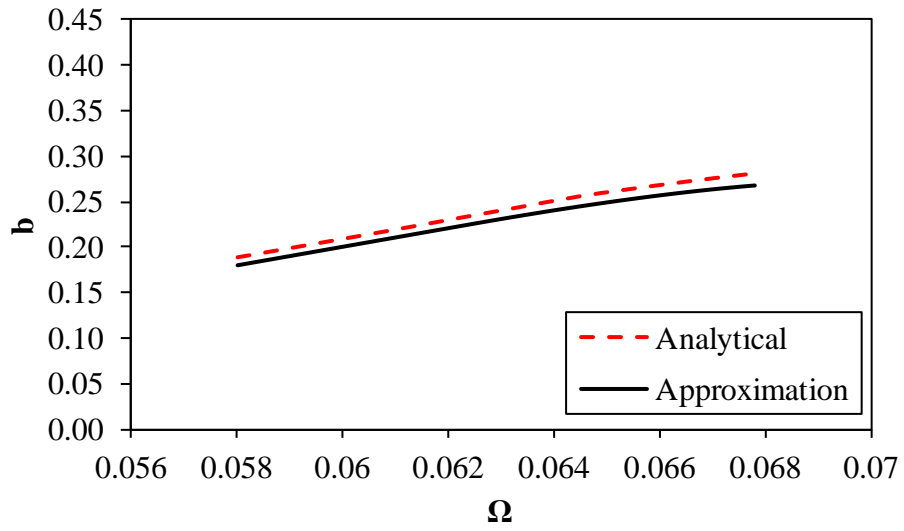
(c) MAT3



(d) MAT4



(e) MAT5



(f) MAT6

**Figure B6.** Comparison Between b vs.  $\Omega$  Approximated and Analytical Relationships.



## **Appendix C: Proof of Sign Retainment of Radical in Equation for u**

### **C.1 Introduction**

Because the NURBS curve is determined with parametric equations, and one of the coordinates is already known, the common variable,  $u$ , needs to be calculated to solve for the other coordinate. The Bezier curve for all situations is approximated with 2<sup>nd</sup> degree Bernstein polynomials which means that the variable  $u$  is calculated using the quadratic formula. Usually, when using the quadratic formula, the radical is either added or subtracted from the rest of the equation. This is to account for both of the solutions to any quadratic equation. This appendix provides a proof that the radical in the equation for  $u$  is always added.

### **C.2 Un-weighted NURBS Curves**

Recall that both coordinates of the NURBS curves used in this report are defined by equations (A.3) and (A.4) which include 3 control points. Rearranging equation (A.3) so that  $u$  is in terms of the control and coordinate points leads to equation (C.1).

$$u(C) = \frac{-(2(P_1 - P_0)) \pm \sqrt{(2(P_1 - P_0))^2 - 4(P_2 - 2P_1 + P_0)(P_0 - C)}}{2(P_2 - 2P_1 + P_0)} \quad (C.1)$$

As previously stated, the values of  $u$  only range from 0 to 1. Applying these limits to equation (C.1) results in the following inequality:

$$0 \leq \frac{-(2(P_1 - P_0)) \pm \sqrt{(2(P_1 - P_0))^2 - 4(P_2 - 2P_1 + P_0)(P_0 - C)}}{2(P_2 - 2P_1 + P_0)} \leq 1$$
$$2(P_1 - P_0) \leq \pm \sqrt{(2(P_1 - P_0))^2 - 4(P_2 - 2P_1 + P_0)(P_0 - C)} \leq 2(P_2 - 2P_1 + P_0) + 2(P_1 - P_0)$$

$$2(P_1 - P_0) \leq \pm \sqrt{(2(P_1 - P_0))^2 - 4(P_2 - 2P_1 + P_0)(P_0 - C)} \leq 2(P_2 - P_1)$$

Recall the control points for all cases where the un-weighted NURBS curve is used. For the relationship between  $\Omega$  and the factor  $b$ , the three control points are  $(\Omega_1, b_1)$ ,  $(\Omega_j, b_j)$  and  $(\Omega_2, b_2)$  in sequential order. For major reversals, the three control points used are  $(\varepsilon''_k, f''_k)$ ,  $(\varepsilon''_j, f''_j)$  and  $(1,1)$  in sequential order. For minor reversals, the three control points used are  $(0,0)$ ,  $(\varepsilon''_j, f''_j)$  and  $(1,1)$  in sequential order.

For all cases where the Bezier curve is used, both coordinates of the control points follow the same inequality:  $P_2 > P_1 > P_0$ . This means that the boundaries of the inequality are positive terms, meaning that the radical can only be added. Thus for equation (C.1), there is only need to calculate one solution to the quadratic equation.

### C.3 In Calculations For The Onset of Buckling

The calculations for  $\gamma_{T,11}$  and  $\gamma_{T,22}$  also involve Bezier curves and not NURBS curves. However, the calculations for  $\gamma_{T,12/21}$  and the location of the neutral axis,  $\bar{y}$ , involve weighted NURBS curves. Furthermore, the radicals in the calculation of the parameter,  $u_T$ , are subtracted for all of these variables as shown in equations (3.45) and (3.47).

The proof in the previous section still applies to the calculations for  $\gamma_{T,11}$  and  $\gamma_{T,22}$ , except the terms all switch sign. This leads to the switching of the inequality and a radical bounded by negative terms. This proof doesn't apply to the calculation of  $\gamma_{T,12/21}$  because of the weights. To prove that the radical is always subtracted in this calculation, equation (3.45) is rearranged when introduced into the inequality shown below.

$$0 \leq \frac{0.44\eta + 0.3432 \pm \sqrt{(-0.44\eta - 0.3432)^2 - 4\eta(0.44\eta - 0.6568)}}{2(0.44\eta - 0.6568)} \leq 1$$

$$-0.44\eta - 0.3432 \leq \pm \sqrt{(-0.44\eta - 0.3432)^2 - 4\eta(0.44\eta - 0.6568)} \leq 0.44\eta - 1.6568$$

Because  $\eta$  is always positive and less than or equal to 1, the radical is bounded by two negative terms and the inequality switches as shown below.

$$-0.44\eta - 0.3432 \geq \pm \sqrt{(-0.44\eta - 0.3432)^2 - 4\eta(0.44\eta - 0.6568)} \geq 0.44\eta - 1.6568$$

Therefore, the radical is always subtracted in this case.

The calculation of  $u$  for the NURBS approximation of the location of the neutral axis is more complex. It is difficult to prove analytically that the radical is always subtracted. Instead, the relationship between  $u$  with  $\eta$  was split into two cases: one where the radical is added and another where the radical is subtracted. These relationships are plotted in Figure C1 and show that only a subtracted radical will lead to a value of  $u$  between 0 and 1. Therefore, the radical must always be subtracted.

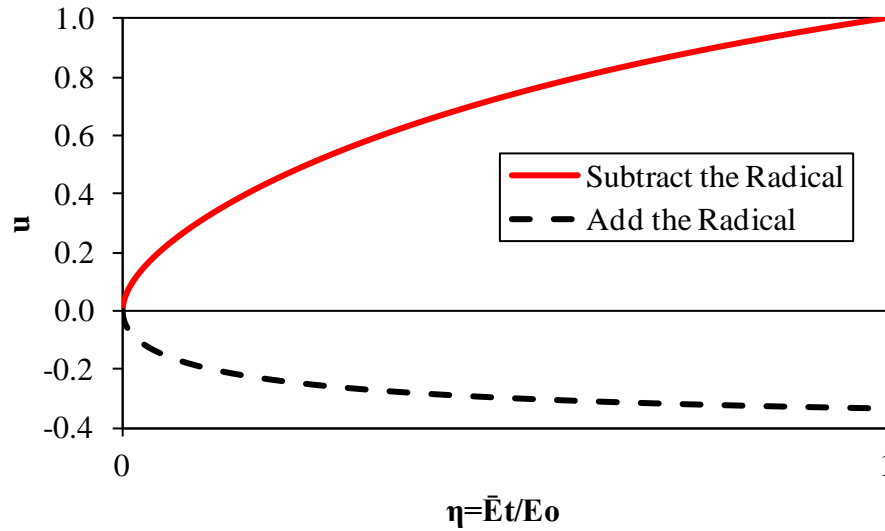


**Figure C1.** Variation of  $u$  with  $\eta$  in the Equations for Buckling Considerations.

## **Appendix D: Single Curvature Check in Reversal curves**

### **D.1 Introduction**

The sign of the 2<sup>nd</sup> derivative of the hysteretic equations used to simulate the reversal curve must be retained for the entire range of strain. This will ensure that the hysteretic loop will be convex in shape. Furthermore, when the curve is in tension, the second derivative must be negative, and when the curve is in compression, the sign must be positive. Therefore, the sign of the second derivative in the natural coordinate space is the opposite of that of the term “s” (which is negative when in a compressive reversal and vice versa) as was observed through various experimental tests with cyclic loading. This appendix provides a proof for sign retainment in curvature throughout a reversal curve.

### **D.2 Sign Retainment in the Natural Coordinate Space**

The following equations are used to describe the 1<sup>st</sup> and 2<sup>nd</sup> derivatives in the double prime coordinate space.

$$\frac{df''}{d\varepsilon''} = \frac{df''/du}{d\varepsilon''/du} \quad (\text{D.1})$$

$$\frac{d^2 f''}{d\varepsilon''^2} = \frac{\left(d\varepsilon''/du\right)\left(d^2 f''/du^2\right) - \left(d^2 \varepsilon''/du^2\right)\left(df''/du\right)}{\left(d\varepsilon''/du\right)^3} \quad (\text{D.2})$$

Because the transformation from the natural coordinates to double prime coordinates is linear, only equation (D.3) shows the application of the chain rule to equation (D.2) to calculate the 2<sup>nd</sup> derivative in the natural coordinate space. While the sign of  $\frac{d\varepsilon''}{d\varepsilon'_s}$  doesn't affect the sign

of expression (D.3), the sign of  $\frac{df'_s}{df''}$  is that of the term  $s$ . If the sign of (D.2) is proven to be always negative, then the sign of expression (D.3) will always be the opposite of that of the term  $s$ .

$$\frac{d^2 f'_s}{d\varepsilon'_s{}^2} = \frac{d^2 f''}{d\varepsilon''^2} \frac{df'_s}{df''} \left( \frac{d\varepsilon''}{d\varepsilon'_s} \right)^2 \quad (\text{D.3})$$

### D.3 Major Reversals

Because the reversal curve before the continuity point is linear, the second derivative of the equation is always zero. Although that doesn't fulfill the requirements of the sign being negative in the double prime space, this requirement is irrelevant before the continuity point since the approximation is merely an extension of the already defined unloading branch.

The 1<sup>st</sup> and 2<sup>nd</sup> derivatives of the Bezier curve approximation are shown in equations (D.4) and (D.5).

$$C'(u) = -2(1-u)P_0 + 2(1-2u)P_1 + 2uP_2 \quad (\text{D.4})$$

$$C''(u) = 2(P_0 - 2P_1 + P_2) \quad (\text{D.5})$$

After adding the control points previously defined, equations (D.4) and (D.5) are substituted into equation (D.4) and simplified, which results in equation (D.6).

$$\frac{d^2 f''}{d\varepsilon''^2} = \frac{4(\varepsilon''_k f''_j - \varepsilon''_j f''_k + \varepsilon''_j - f''_j - \varepsilon''_k + f''_k)}{(-2(1-u)\varepsilon''_k + 2(1-2u)\varepsilon''_j + 2u)^3} \quad (\text{D.6})$$

Equation (D.6) is further simplified after  $\varepsilon''_k$  and  $f''_k$  are substituted using equations (3.27) and (3.28).

$$\frac{d^2 f''}{d\varepsilon''^2} = \frac{(1-b)^2 (\varepsilon''_j - f''_j)}{8(-(1-u)\varepsilon''_k + (1-2u)\varepsilon''_j + u)^3} \quad (\text{D.7})$$

As previously stated, the Bernstein polynomials that make up (A.3) and (A.4) are calculated with a knot vector  $\{0,0,0,1,1,1\}$ . This means that the value of  $u$  is always between 0 and 1 (Piegl, 1997). If these limits are applied to (A.3), a new inequality emerges.

$$2(P_1 - P_0) \leq -2(1-u)P_0 + 2(1-2u)P_1 + 2uP_2 \leq 2(P_2 - P_1)$$

For both of the double prime strain and stress coordinates of the control points,  $P_2 > P_1 > P_0$ . This means that the inequality is bounded by two positive terms, proving that the first derivative and, consequently, the denominator of equation (D.7) is always positive.

The sign of the numerator of equation (D.7) depends on the expression  $(\varepsilon''_j - f''_j)$ . It is known that  $E'_u$  is greater than  $\frac{f'_{rejoin} - f'_a}{\varepsilon'_{rejoin} - \varepsilon'_a}$ . This means that the initial slope of the curve in the double prime coordinate space is always greater than 1. Therefore,  $f''_j > \varepsilon''_j$  and the numerator and, consequently, the 2<sup>nd</sup> derivative in the double prime coordinate space is always negative.

#### D.4 Minor and Simple Reversals

The 1<sup>st</sup> and 2<sup>nd</sup> derivatives of the NURBS parametric equation (3.19) with a zero first control point are shown below.

$$C'(u) = 2(1-2u)P_1 + 2uP_2 \quad (\text{D.8})$$

$$C''(u) = -4P_1 + 2P_2 \quad (\text{D.9})$$

The appropriate control points are added to equations (D.8) and (D.9), substituted into equation (D.2) and then simplified.

$$\frac{d^2 f''}{d\varepsilon''^2} = \frac{(2\varepsilon''_j + u(2 - 4\varepsilon''_j))(-4f''_j + 2) - (2f''_j + u(2 - 4f''_j))(-4\varepsilon''_j + 2)}{2(1 - 2u)\varepsilon''_j - 2u} \quad (\text{D.10})$$

$$\frac{d^2 f''}{d\varepsilon''^2} = \frac{2(\varepsilon''_j - f''_j)}{(1 - 2u)\varepsilon''_j - u} \quad (\text{D.11})$$

The numerator of equation (D.11) is put in terms of  $f''_j$  to determine the sign of the numerator.

$$\frac{d^2 f''}{d\varepsilon''^2} = \frac{2f''_j \left( \frac{1}{\frac{df''_{start}}{d\varepsilon''}} - 1 \right)}{(1 - 2u)\varepsilon''_j - u}$$

where  $\frac{df''_{start}}{d\varepsilon''}$  is the initial slope of the curve in the double prime coordinate space. Recall that

$\frac{df''_{start}}{d\varepsilon''}$  is always greater than 1. Since the term  $f''_j$  is always positive, the numerator must

always be negative.

If the 2<sup>nd</sup> derivative of the curve in the double prime coordinate space must be negative, the denominator must be positive for all values of  $u$ . The inequality shown below is split into two situations because of the term  $(1 - 2u)$  is positive for  $\{0 \leq u \leq 0.5\}$  and negative for  $\{0.5 \leq u \leq 1\}$

$$(1 - 2u)\varepsilon''_j - u > 0$$

$$\left\{ \begin{array}{l} \frac{-u}{1 - 2u} \leq 0 \\ \varepsilon''_j > \frac{-u}{1 - 2u} \end{array} \right. \text{ for } 0 \leq u < 0.5$$

$$\left\{ \begin{array}{l} \frac{-u}{1 - 2u} \geq 1 \\ \varepsilon''_j < \frac{-u}{1 - 2u} \end{array} \right. \text{ for } 0.5 < u \leq 1$$

Thus the restriction for the term  $\varepsilon''_j$  in these equations is  $0 \leq \varepsilon''_j \leq 1$  for any value of  $u$ .

At  $u = 0.5$ , the term  $\frac{-u}{1-2u}$  is either negative or positive infinity. The term  $\varepsilon''_j$  is always positive and never greater than 1. This means that for all possible values of  $\varepsilon''_j$ , the denominator of the 2<sup>nd</sup> derivative in the double prime space is always positive. Therefore the 2<sup>nd</sup> derivative in the double prime coordinate space must always be negative.

### D.5 Sign Retainment in the Engineering Coordinate Space

The sign of curvature is proven to be retained in the natural coordinate space. However, the conversion between engineering coordinates and natural coordinates are logarithmic. The sign of conversion must be proven to be retained after the coordinates are transformed back to engineering coordinates. The second derivative of the engineering stress strain curve was derived in terms of the second derivative of the true stress-strain curve using the chain rule as shown in equation (D.12).

$$\frac{d^2 f'_s}{d\varepsilon_s^2} = \frac{1}{1+\varepsilon_s} \frac{d^2 f'_s}{d\varepsilon_s'^2} \left( \frac{d\varepsilon_s'}{d\varepsilon_s} \right)^2 - \frac{2}{(1+\varepsilon_s)^2} \frac{df'_s}{d\varepsilon_s'} \frac{d\varepsilon_s'}{d\varepsilon_s} + \frac{2}{(1+\varepsilon_s)^3} f'_s \quad (\text{D.12})$$

Recall equation (3.60).

$$\frac{d\varepsilon_s'}{d\varepsilon_s} = \frac{1}{1+\varepsilon_s} \quad (\text{3.60})$$

Equation (3.60) is substituted into equations (D.12) to get (D.13).

$$\frac{d^2 f'_s}{d\varepsilon_s^2} = \frac{1}{(1+\varepsilon_s)^3} \left( \frac{d^2 f'_s}{d\varepsilon_s'^2} - 2 \frac{df'_s}{d\varepsilon_s'} + 2f'_s \right) \quad (\text{D.13})$$

As equation (D.13) shows, the sign of the second derivative might not always be retained. However, determining when the sign changes along the curve cannot be done analytically. So for



several curves used to compare the original and modified nonlinear reversal curves, the slope was recorded along randomly determined curves. The relationship between slope along the reversal curve and strain follows a similar behavior for all tensile reversals and compressive reversals as shown in Figures D1 and D2.

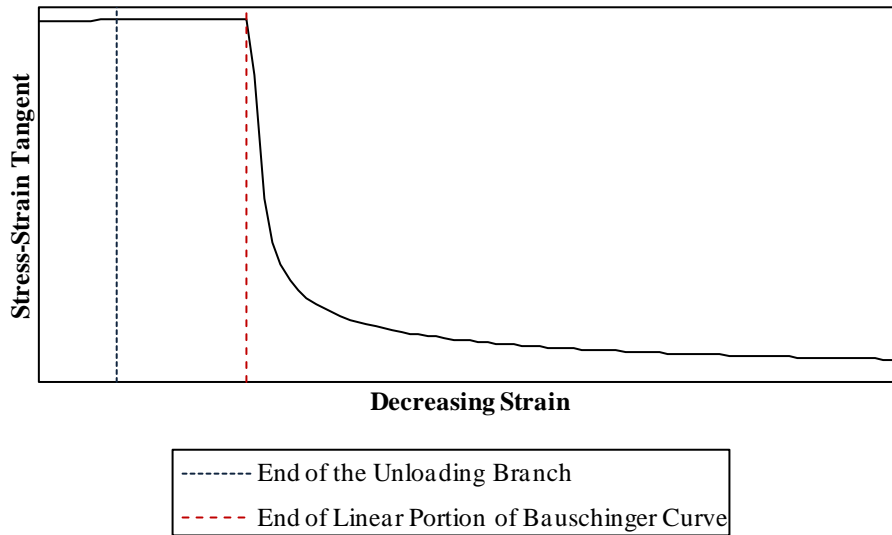


**Figure D1.** Stress-Strain Tangent vs. Strain Along a Compressive Reversal.

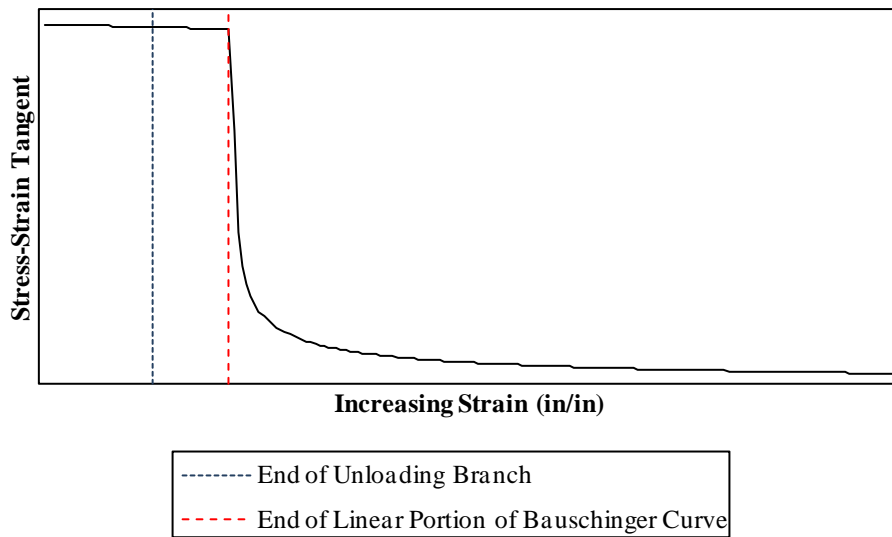


**Figure D2.** Stress-Strain Tangent vs. Strain Along a Tensile Reversal.

For tensile reversals, the tangent decreases throughout the entire range of strain, showing that the sign of curvature is retained for every tensile reversal curve. For compressive reversals, the tangent decreases as the curve progresses to the end for the non-linear portions of the reversal curve. The tangent increases in the linear regions of the natural coordinate space, showing a change in sign of curvature. This is due to the Poisson's effect, increasing the cross-sectional area, which would explain why only compressive curves experience this and tensile curves don't. However, the change in slope throughout the linear region isn't significant ( $<3\%$ ) for any of the strain histories observed, leading to the assumption that the curvature in the linear region of any curve is negligible. With this assumption, the sign of curvature for every curve is retained in the engineering coordinate space.

## **Appendix E: Comparison Between the Analytical Values and Approximated Values of the Sectional Tangent Stiffness Matrix for a Reinforcing bar**

### **E.1 Introduction**

When determining the onset of buckling, it is important to determine the stiffness matrix. Once the neutral axis is determined, the stiffness matrix can be directly calculated. However, calculating the matrix involve a set of complicated equations. Thus, these values are approximated using the NURBS algorithm.

Recall that the stress acting on a portion of the cross-section will be governed by a different tangent modulus than the stress acting on the other portion. So it is important to determine the geometry of a circular segment, specifically the area, the 1<sup>st</sup> moment of area and the moment of inertia about the neutral axis. The geometry of the circular segment with a height less than the radius of the bar will be found first, and all of the equations will be put in terms of that geometry.

### **E.2 Determining the Onset of Buckling**

Because the stiffness matrix involves several double integrals over the area of the section, it is important to determine the location of the neutral axis. An expression is found using the force equilibrium equation. The stress distribution throughout the area of the bar is shaped like a cylindrical wedge on both sides of the neutral axis. The force acting on either side of the shape is the volume of the stress distribution.

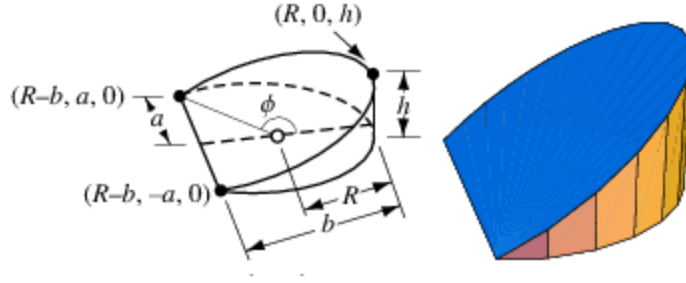


**Figure E1.** Geometry of a Cylindrical Wedge (Retrieved from: Weisstein, n.d.).

The equation for the volume of a cylindrical wedge based on the parameters shown in Figure E1 was already derived in the Wolfram Web Resource (Weisstein, n.a.).

$$V = \frac{h}{3b} \left( a(3R^2 - a^2) + 3R^2(b - R)\phi \right) \quad (\text{E.1})$$

Where

$$a = \sqrt{b(2R - b)} \quad (\text{E.2})$$

$$\phi = \cos^{-1} \left( 1 - \frac{b}{R} \right) \quad (\text{E.3})$$

In this case,  $h = df_{\max/\min} = E_t d\phi_o b = E_t d\omega''_o b$  and  $b = \bar{y}$  or  $(D - \bar{y})$  where  $D$  is the diameter of the reinforcing bar,  $\bar{y}$  is the location of the neutral axis from the bottom of the reinforcing bar cross section and  $E_t$  is the sectional tangent modulus of the stress-strain curve and the term,  $d\phi_o$ , refers to the change in curvature at midspan.

The definitions of  $h$  and  $b$ , as well as diameter in terms of radius, are substituted into (E.1) These expressions are then used to calculate the tensile and compressive forces and they are substituted into the equilibrium equation.

$$\sum F = 0 = T + C$$

$$0 = \frac{d\phi_o}{3} \left[ \begin{aligned} &\sqrt{\bar{y}(D-\bar{y})} \left( \frac{3}{4} D^2 - D\bar{y} + \bar{y}^2 \right) (\bar{E}_t - E_o) + \dots \\ &\dots \frac{3D^2}{4} \left( \bar{y} - \frac{D}{2} \right) \left( \bar{E}_t \cos^{-1} \left( 1 - \frac{2\bar{y}}{D} \right) + E_o \cos^{-1} \left( \frac{2\bar{y}}{D} - 1 \right) \right) \end{aligned} \right] \quad (\text{E.4})$$

where  $E_o$  is equal to the unloading modulus,  $E'_u$ , and  $\bar{E}_t$  is the tangent modulus of the stress-strain curve.

Because the change in curvature will never be zero, the entire term in the brackets must equal zero. As stated before, this equation is too complex to analytically solve for the only unknown,  $\bar{y}$ . Instead, the iterative process is done only once to show the relationship between the tangents and the location of the neutral axis. To make calculations simpler, the term,  $E_o$ , was factored out to leave a ratio,  $\eta$ , of  $\bar{E}_t$  to  $E_o$ . The location of the neutral axis is also divided by the diameter of the bar, because the ratios of the areas on either side of the neutral axis are the same regardless of the diameter of the bar. Thus a more general relationship was between  $\eta$  and  $\bar{y}/D$  was found. A NURBS approximation is shown (3.29) in section 3.4.1 and is compared to the analytical method in Figure E2. As shown, the approximation is suitable to calculate the ratio of the location of the neutral axis to the diameter of the reinforcing bar.

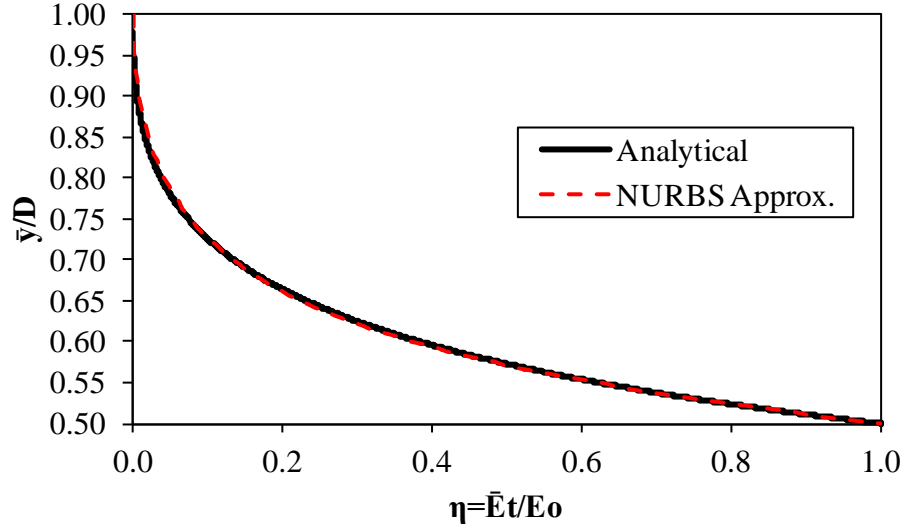


**Figure E2.** Comparison of Analysis from (E.4) and NURBS Approximation of the Ratio of the Location of the Neutral Axis to the Diameter of the Reinforcing bar.

### E.3 Deriving the Sectional Tangent Matrix

As stated before, the shape matrix has four elements as shown below.

$$\hat{D}_{T,11} = \iint_A \bar{E}_t dS = A_t E_o + A_c \bar{E}_t \quad (\text{E.5})$$

$$\hat{D}_{T,12} = \hat{D}_{T,21} = \iint_A -y E_t dS = -(A_t \bar{y}_t E_o + A_c \bar{y}_c \bar{E}_t) \quad (\text{E.6})$$

$$\hat{D}_{T,22} = \iint y^2 E_t dS = I_t E_o + I_c \bar{E}_t \quad (\text{E.7})$$

where  $A_t$  is the area unloading,  $A_c$  is the area in continued compression,  $\bar{y}_t$  is the distance to the centroid of the unloading area from the neutral axis,  $\bar{y}_c$  is the distance to the centroid of the area under continued compression from the neutral axis,  $I_t$  is the moment of inertia of the unloading area and  $I_c$  is the moment of inertia of the area under continued compression.

To simplify the equations,  $A_c$ ,  $A_c \bar{y}_c$  and  $I_c$  were put into terms of  $A_t$ ,  $A_t \bar{y}_t$  and  $I_t$  respectively. Also,  $E_o$  was factored out to introduce the term,  $\eta$ .

$$\hat{D}_{T,11} = E_o \left( A_t + \left( \pi \left( \frac{D}{2} \right)^2 - A_t \right) \eta \right) = E_o \left( A_t (1-\eta) + \pi \left( \frac{D}{2} \right)^2 \eta \right)$$

$$\hat{D}_{T,12} = \hat{D}_{T,21} = -E_o \left( A_t \bar{y}_t (1-\eta) + \pi \left( \frac{D}{2} \right)^2 \left( \bar{y} - \frac{D}{2} \right) \eta \right)$$

$$\hat{D}_{T,22} = E_o \left( I_t (1-\eta) + \left( \frac{1}{4} \pi \left( \frac{D}{2} \right)^4 + \pi \left( \frac{D}{2} \right)^2 \left( \bar{y} - \frac{D}{2} \right)^2 \right) \eta \right)$$

where  $\bar{y}$  is the location of the neutral axis from the extreme compression fiber.

Using the geometry of a circular segment and the parallel axis theorem, the following expressions were found for  $A_t$ ,  $\bar{y}_t$  and  $I_c$ .

$$A_t = \frac{\left( \frac{D}{2} \right)^2}{2} (\theta - \sin \theta) \quad (\text{E.9})$$

$$\bar{y}_t = \frac{2D \sin^3 \frac{\theta}{2}}{3(\theta - \sin \theta)} - \left( \bar{y} - \frac{D}{2} \right) \quad (\text{E.10})$$

$$I_t = \frac{\left( \frac{D}{2} \right)^4}{8} \left( \theta - \sin \theta + 2 \sin \theta \sin^2 \frac{\theta}{2} \right) \quad (\text{E.11})$$

where  $\theta$  is the angle in radians of the circular arc on the perimeter of the circular segment which can be calculated using (E.12).

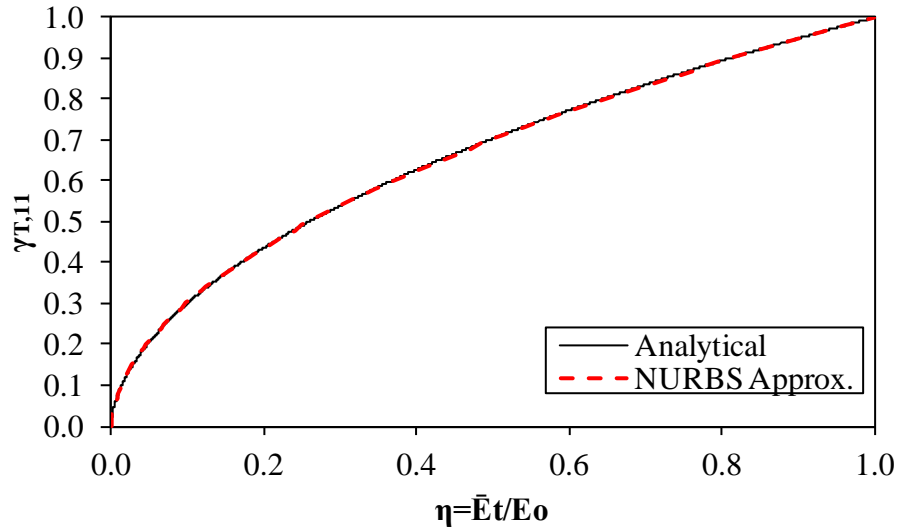
$$\theta = 2 \cos^{-1} \left( \frac{2\bar{y}}{D} - 1 \right) \quad (\text{E.12})$$

As apparent in (E.5) to (E.12), the stiffness matrix can be calculated analytically without any iterative processes. A NURBS approximation can be fitted to the (E.5), (E.6) and (E.7) to simplify calculations even further. In order to normalize the stiffness matrix calculations for any

material, the NURBS approximations are calibrated to the terms  $\frac{\hat{D}_{T,11}}{E_o\pi\left(\frac{D}{2}\right)^2}$ ,  $\frac{\hat{D}_{T,12,21}}{E_o\pi\left(\frac{D}{2}\right)^3}$  and

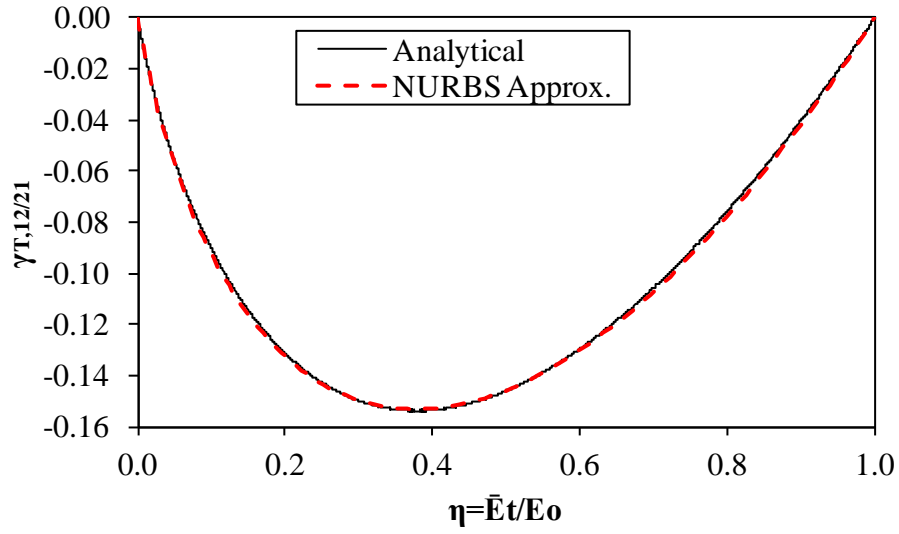
$\frac{\hat{D}_{T,22}}{E_o\pi\left(\frac{D}{2}\right)^4}$ . As stated before, these terms are denoted as  $\gamma_{T,11}$ ,  $\gamma_{T,12/21}$  and  $\gamma_{T,22}$ , and the resulting

NURBS approximations are described in section 3.4.1. The accuracy of the NURBS approximation was checked with the analytical equations and there is good agreement between the two relationships as shown in Figures E3a-c.

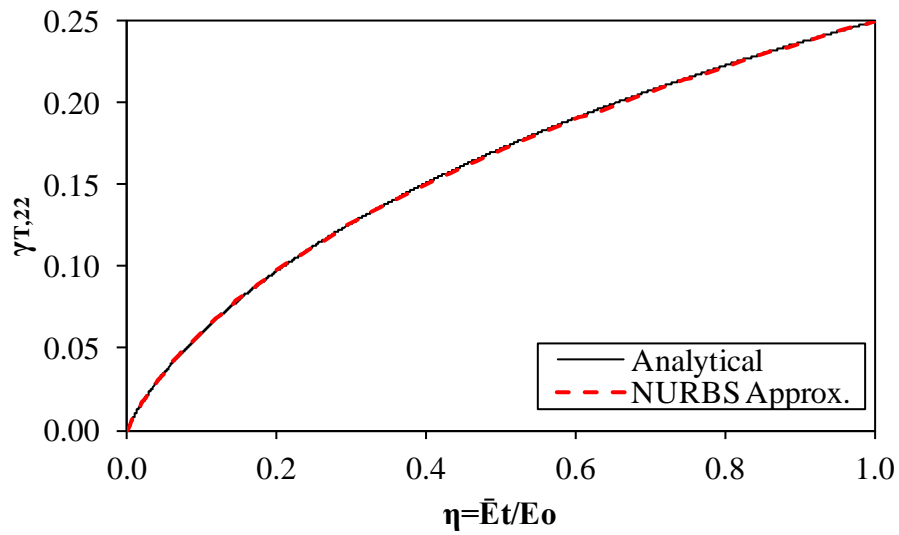


(a)  $\gamma_{T,11}$  vs.  $\eta$





(b)  $\gamma_{T,12/21}$  vs.  $\eta$



(c)  $\gamma_{T,22}$  vs.  $\eta$

**Figure E3.** Comparison between Analytical Results and NURBS Approximations in Predicting the Stiffness Matrix Parameters.

## **Appendix F: Calibration of Strength Degradation Factor with Monotonic Experimental Data**

### **F.1 Introduction**

After the onset of buckling is calculated, a factor is applied to the strength to simulate the inelastic post-buckling behavior. The factor varies from 1 until the factored stress reaches the residual strength determined to be at 20% of the yield stress. NURBS is yet again employed to approximate this variation.

### **F.2 Method**

As a starting point, the monotonic experimental results compiled by Bayrak and Sheikh were used. They have performed compressive monotonic tests on several specimens of the same material properties while varying the slenderness ratio and the initial eccentricity. For the purposes of this research, only the results from specimens with no initial eccentricities were observed (Bayrak and Sheikh, 2001). A compressive monotonic analysis with the proposed model was done to obtain the stress in the reinforcement without buckling. The experimental stresses and the analytical stresses were then divided to get the variation of the experimental strength degradation factor. The results are shown in Figure F1.

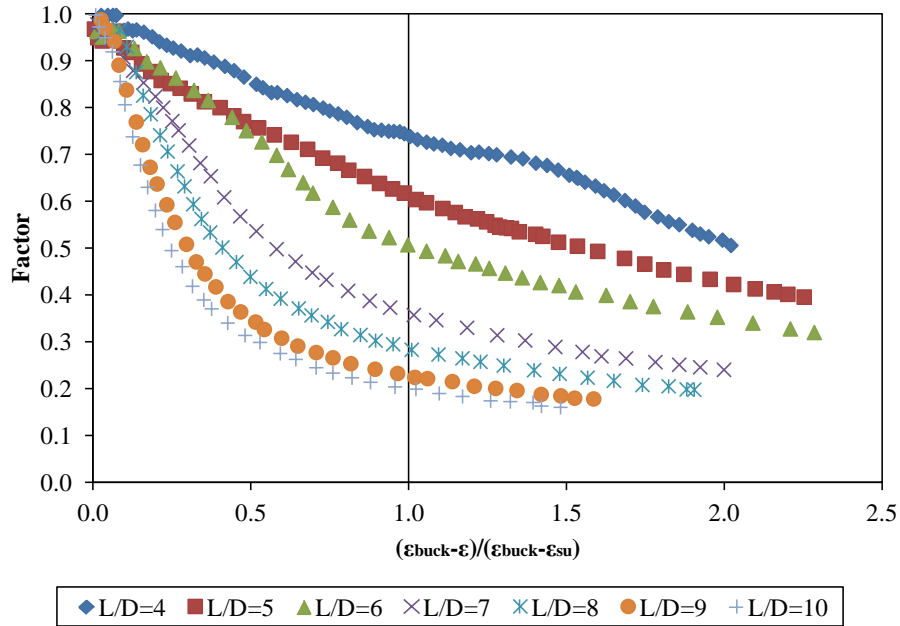


**Figure F1.** Variation of the Strength Degradation Factor with Strain Normalized to the Buckled Strain and Slenderness Ratio.

The factor varied with the compressive strain normalized to the difference between the strain at the onset of buckling and the negative of the ultimate strain. Although there is a clear pattern showing between the sharpness of the curve and the slenderness ratio, this relationship is difficult to approximate numerically. As shown in Figure F2, the relationship with the logarithm of the factor with base 10 and the normalized strain is easier to capture numerically for the sole reason that the curves all seem to reach the same slope after the negative of the ultimate strain. So the average of the slopes after the ultimate strain is shown to be -0.17034. However, there it is clear that the factor at negative ultimate strain and the initial slope varies.

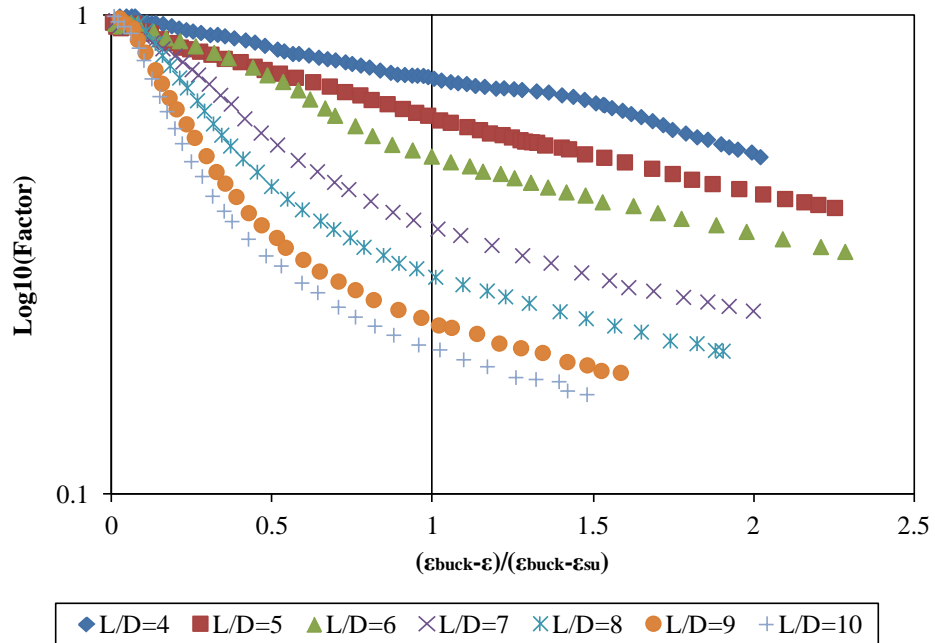


**Figure F2.** Variation of Logarithm of the Strength Degradation Factor with Normalized Strain.

With linear interpolation, the factor at ultimate for each slenderness ratio was recorded. Figure F3 shows that a suitable linear relationship can be found between the slenderness ratio,  $L/D$ , and the factor at ultimate,  $f_2$ .

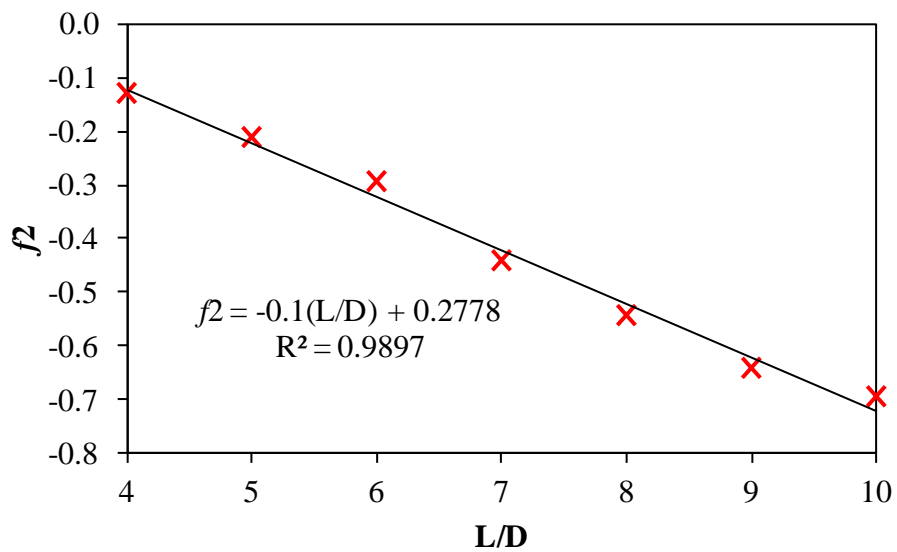


**Figure F3.** Strength Degradation Factor at Negative Ultimate vs. Slenderness Ratio.

The next step was to find the initial slope. However, as Dhakal and Maekawa have shown in their analyses, the material properties of the material also play a role in the buckling behavior of a material (2002). Additional analyses were done with results from experiments performed by Mander, Priestley, and Park, which were reported by Dhakal and Maekawa (2002).

To find the initial slope, a bilinear approximation was overlaid on the experimental data and then a suitable initial slope for the approximation was recorded. It was also determined that the slope would vary with the slenderness ratio and the square root of the power of the strain hardening curve. This power was used to represent the material properties because it was unitless and it led to the best linear fit shown in Figure F4.

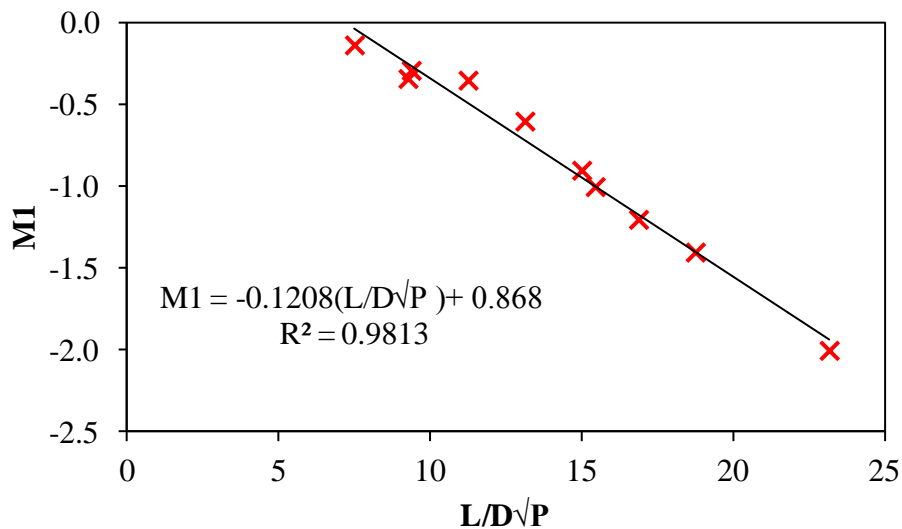


**Figure F4.** Relationship Between The Initial Slope, M1, and The Slenderness Ratio and Material Properties.

Once these properties could be accounted for, a NURBS algorithm was developed with weight values of 1 and the control points at the beginning (0,1), ultimate (1,f2) and the

intersection of slopes M1 and M2. This algorithm was compared with the experimental data gathered by Bae, Miseses, and Bayrak (2005) as shown in Figure F5.

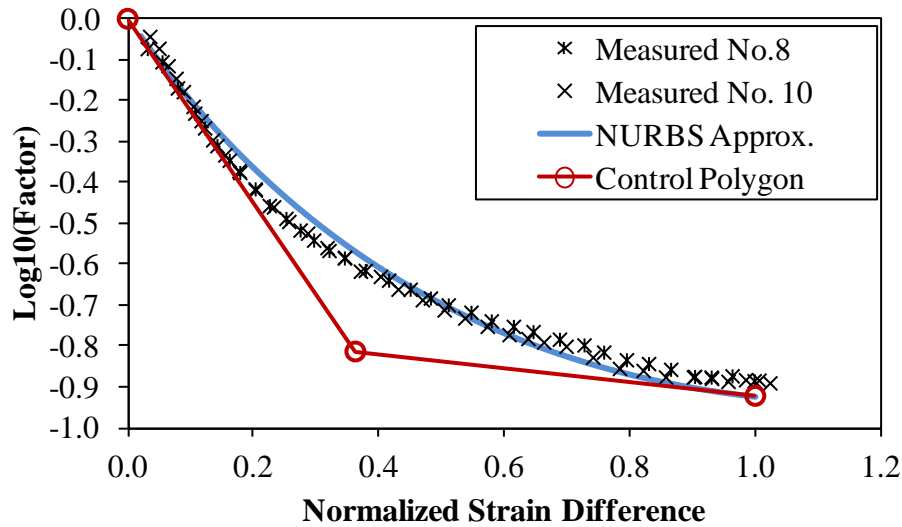
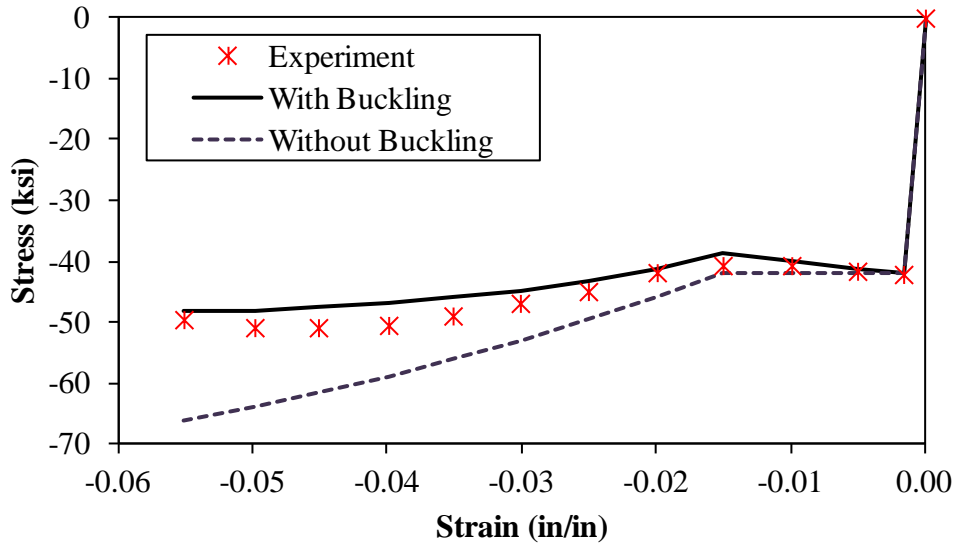


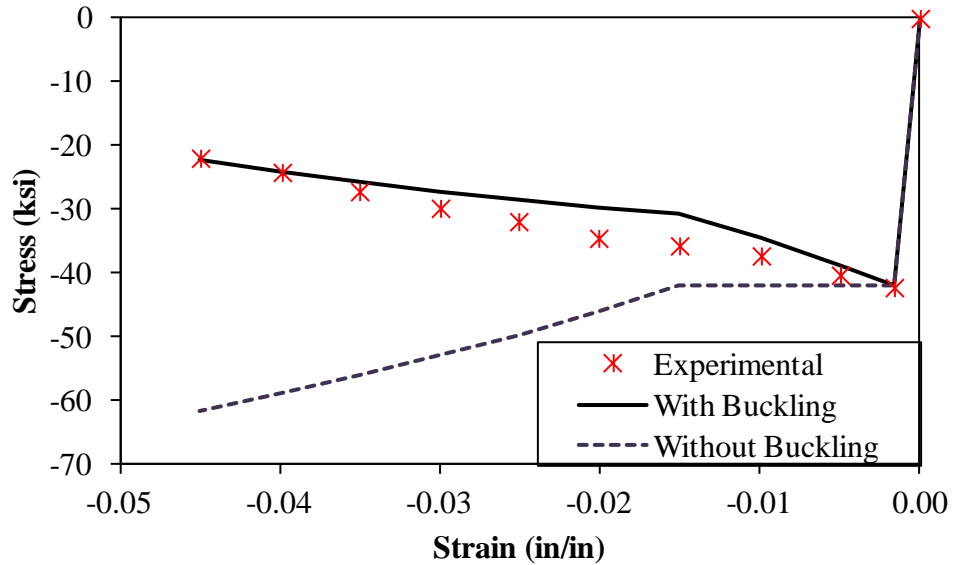
**Figure F5.** Comparisons Between The Proposed Approximation and The Experimental Results of the Logarithm of the Strength Degradation Factor (Bae et al., 2005).

There are instances where the initial slope and the final slope do not intersect between the normalized strain values of 0 and 1. When this does happen, the initial and final slopes are somewhat similar and overlapping. Therefore, for these cases, the variation of the logarithm of the factor is approximated with a line at the initial slope.

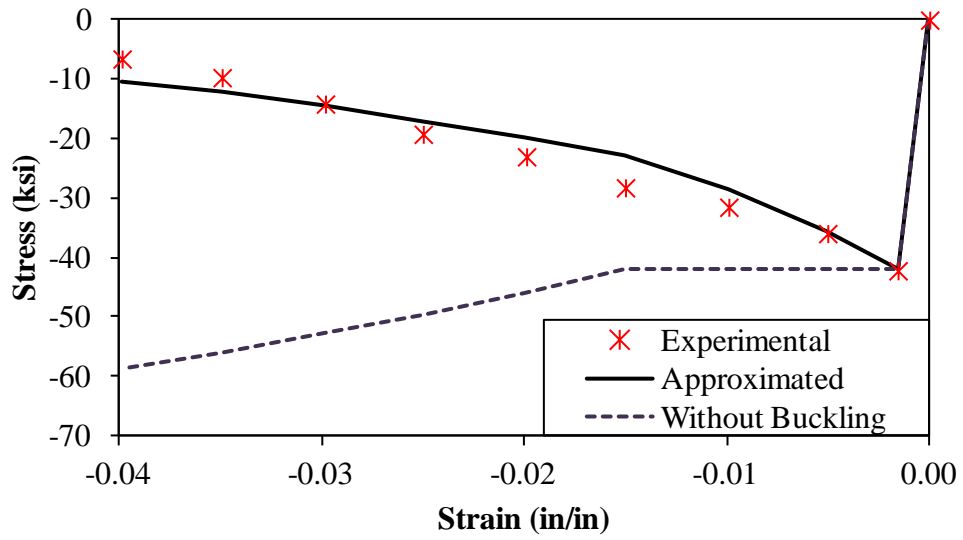
The comparisons between the monotonic experimental data gathered by Mander (Dhakal and Maekawa, 2002ab) and the analysis with the buckling considerations implemented are shown in Figures F6 a-c.



(a) Comparisons Between Bare-Bar Monotonic Test Results and Approximations (L/D=5) (Dhakar and Maekawa, 2002a)



(b) Comparisons Between the Bare-Bar Monotonic Test Results and Approximations (L/D=8) (Dhakar and Maekawa, 2002a)



(c) Comparisons Between the Bare-Bar Monotonic Test Results and Approximations ( $L/D=11$ ) (Dhakai and Maekawa, 2002a)

**Figure F6.** Comparisons Between the Bare-Bar Monotonic Test Results and Approximations of the Buckled Response (Dhakai and Maekawa, 2002ab).